

**NITROGEN AND SULPHUR CO-DOPED CARBON QUANTUM DOTS /  
TITANIUM DIOXIDE PHOTOCATALYTIC MEMBRANE FOR  
PHOTODEGRADATION OF DICLOFENAC IN WATER**

**KOE WENG SHIN**

**A project report submitted in partial fulfilment of the  
requirements for the award of Bachelor of Engineering  
(Honours) Chemical Engineering**

**Lee Kong Chian Faculty of Engineering and Science  
Universiti Tunku Abdul Rahman**

**January 2019**

## DECLARATION

I hereby declare that this project report is based on my original work except for citations and quotations which have been duly acknowledged. I also declare that it has not been previously and concurrently submitted for any other degree or award at UTAR or other institutions.

Signature : \_\_\_\_\_

Name : KOE WENG SHIN

ID No. : 1403373

Date : \_\_\_\_\_

**APPROVAL FOR SUBMISSION**

I certify that this project report entitled **NITROGEN AND SULPHUR CO-DOPED CARBON QUANTUM DOTS / TITANIUM DIOXIDE PHOTOCATALYTIC MEMBRANE FOR PHOTODEGRADATION OF DICLOFENAC IN WATER** was prepared by **KOE WENG SHIN** has met the required standard for submission in partial fulfilment of the requirements for the award of Bachelor of Engineering (Honours) Chemical Engineering at Universiti Tunku Abdul Rahman.

Approved by,

Signature : \_\_\_\_\_

Supervisor : Dr. Chong Woon Chan

Date : \_\_\_\_\_

Signature : \_\_\_\_\_

Co-Supervisor : Dr. Pang Yean Ling

Date : \_\_\_\_\_

The copyright of this report belongs to the author under the terms of the copyright Act 1987 as qualified by Intellectual Property Policy of Universiti Tunku Abdul Rahman. Due acknowledgement shall always be made of the use of any material contained in, or derived from, this report.

© 2019, Koe Weng Shin. All right reserved.

## ACKNOWLEDGEMENTS

I would like to thank everyone who had contributed to the successful completion of this project especially, Dr. Mah Shee Keat's master student Mr. Lim Su Wei for providing more than enough assistance in carrying out this research. I would like to express my gratitude to my research supervisor, Dr. Chong Woon Chan and my co-supervisor, Dr. Pang Yean Ling for her invaluable advice, guidance and his enormous patience throughout the development of the research.

In addition, I would also like to express my gratitude to my loving parents and friends who had helped and given me encouragement throughout this period.

## ABSTRACT

Anti-inflammatory drug diclofenac (DCF) was one of the most frequently detected pharmaceuticals waste in water samples. DCF are extremely non-biodegradable and pseudo persistent in environment which cannot be removed by solely membrane filtration or advanced oxidation processes (AOPs) technology. In order to alleviate this problem, mixed matrix membrane (MMM) which was the hybridization of membrane filtration and photocatalysis can overcome both drawbacks by adsorbed DCF onto membrane and further oxidized by photocatalyst immobilized in membrane to form smaller and non-toxic product. In this study, polysulfone (PSF) membrane was deposited with pure  $\text{TiO}_2$  and different loading of NCQDs on N, S-CQDs/ $\text{TiO}_2$  photocatalyst through in-situ phase inversion method and the membrane were evaluated for the photodegradation of diclofenac (DCF) under UV light, visible light and environment light irradiation. Different techniques including FTIR, XRD, SEM-EDX and contact angle meter were employed to characterize and investigate the performance of synthesized MMM. It was found that 1.5g N, S-CQDs/ $\text{TiO}_2$  MMM exhibited the highest photodegradation and pure water permeation flux performance after the overall evaluation. Up to 76.73% of DCF photodegradation was observed after 150 minutes of environment light irradiation. There were improvement of 64.52% of photodegradation efficiency compare to pure  $\text{TiO}_2$  membrane. For permeation flux performance, the composite membrane showed highly hydrophilicity which gave the highest permeability of 277.798  $\text{L}/\text{m}^2 \text{ hr bar}$  among all type of MMM.

## TABLE OF CONTENTS

<b>DECLARATION</b>	<b>ii</b>
<b>APPROVAL FOR SUBMISSION</b>	<b>iii</b>
<b>ACKNOWLEDGEMENTS</b>	<b>v</b>
<b>ABSTRACT</b>	<b>vi</b>
<b>TABLE OF CONTENTS</b>	<b>vii</b>
<b>LIST OF TABLES</b>	<b>xi</b>
<b>LIST OF FIGURES</b>	<b>xiii</b>
<b>LIST OF SYMBOLS / ABBREVIATIONS</b>	<b>xvii</b>

### CHAPTER

<b>1</b>	<b>INTRODUCTION</b>	<b>1</b>
	1.1 Global Water Pollution from Pharmaceutical Waste	1
	1.2 Water Pollution in Malaysia	2
	1.3 Types and Environmental Impacts of Pharmaceutical Compounds	5
	1.4 Advanced Oxidation Processes (AOPs)	8
	1.5 Problem Statement	10
	1.6 Objectives	11
	1.7 Scope and Limitation of the Study	12
<b>2</b>	<b>LITERATURE REVIEW</b>	<b>13</b>
	2.1 Photocatalysis Reaction	13
	2.2 Membrane Filtration	14
	2.2.1 Microfiltration (MF)	18
	2.2.2 Ultrafiltration (UF)	18
	2.2.3 Nanofiltration (NF)	19
	2.3 Photocatalytic Membrane Reactor (PMR)	20

2.4	Photocatalytic Membrane	23
2.5	Fabrication of Photocatalytic Membrane	26
2.6	Classification of Photocatalysts	32
2.6.1	Platinum-Based Photocatalysts	34
2.6.2	Ruthenium-Based Photocatalysts	36
2.6.3	Rhodium-Based Photocatalysts	38
2.6.4	Titanium-Based Photocatalysts	39
2.6.5	Zinc-Based Photocatalysts	41
2.6.6	Copper-Based Photocatalysts	43
2.6.7	Nitrogen-Based Photocatalysts	45
2.6.8	Graphene-Based Photocatalysts	46
2.6.9	CQDs-Based Photocatalysts	48
2.7	N, S Co-Doped CQDs/TiO <sub>2</sub> Deposited on PSF UF Membrane	51
<b>3</b>	<b>METHODOLOGY</b>	<b>53</b>
3.1	General Preview	53
3.2	Materials and Chemicals	53
3.3	Instruments and Equipments	54
3.4	Overall Research Flowchart	56
3.5	Experiment Procedures for Preparation N, S-CQDs/TiO <sub>2</sub> Photocatalysts Solution	57
3.6	Experiment Procedures for Preparation of PSF UF Membrane	58
3.7	Experiment Procedures for Fabrication of N, S-CQDs/TiO <sub>2</sub> Photocatalysts Entrapped on PSF UF Membrane	58
3.8	Characterization of Photocatalyst Solution and Photocatalytic Membrane	60
3.8.1	Characterization of Photocatalyst Solution	60
3.8.2	Characterization of Photocatalytic Membrane	61
3.8.3	Membrane Permeation Flux	64
3.9	Experimental Set-up for Photodegradation Process	65

3.10	Experimental Set-up for Permeation Flux Test	66
3.11	Parameter Studies	67
3.11.1	Effect of NCQDs Loading on N, S-CQDs/TiO <sub>2</sub>	67
3.11.2	Effect of Light Sources	67
3.11.3	Effect of Photocatalytic Membrane Area	67
3.11.4	Effect of Transmembrane Pressure (TMP)	68
3.12	Kinetic Study	68
3.13	UV-Vis Spectrophotometer	69
3.14	Gantt Chart	70
<b>4</b>	<b>RESULTS AND DISCUSSION</b>	<b>71</b>
4.1	Introduction	71
4.1.1	UV-Vis Absorption Spectra of TiO <sub>2</sub> and N, S-CQDs/TiO <sub>2</sub>	71
4.1.2	Fourier Transform Infrared (FTIR)	72
4.1.3	XRD Analysis of TiO <sub>2</sub> and N, S-CQDs/TiO <sub>2</sub>	75
4.1.4	Morphology and Composition Analysis of TiO <sub>2</sub> and N, S-CQDs/TiO <sub>2</sub> Photocatalytic Membrane	76
4.2	Photocatalytic Performance of Prepared Photocatalytic Membrane	81
4.3	Effect of Photocatalytic Membrane Area on Photocatalytic Performance	87
4.4	Photodegradation Kinetics under Environment Light	88
4.5	Hydrophilicity and UF Photocatalytic Membrane Performance	89
4.5.1	Hydrophilicity of Photocatalytic Membrane	89
4.5.2	UF Photocatalytic Membrane Performance	89
4.6	Possible Mechanism of Photodegradation Process	92

<b>5</b>	<b>CONCLUSION AND RECOMMENDATIONS</b>	<b>94</b>
	5.1 Conclusions	94
	5.2 Recommendations	95
	<b>REFERENCES</b>	<b>96</b>

## LIST OF TABLES

Table 1.1:	Impacts of Pharmaceutical Compounds on Environment	6
Table 1.1:	Continued	7
Table 2.1:	Characteristics and Physical Properties for Polymeric and Ceramic Membrane	17
Table 2.2:	Applications of Photocatalytic Membrane in the Photodegradation of Pollutants	24
Table 2.2:	Continued	25
Table 2.3:	Fabrication Methods for Photocatalytic Membrane	30
Table 2.3:	Continued	31
Table 2.4:	Various Type of Photocatalysts for Different Elements	34
Table 2.5:	Photodegradation Rate Between Pure TiO <sub>2</sub> Nanoparticles and TiO <sub>2</sub> /PANI Nanocomposite Photocatalyst	41
Table 3.1:	Material and Chemical Used in Experiment and Their Specifications	53
Table 3.1:	Continued	54
Table 3.2:	Model and Function of Instruments and Equipment	54
Table 3.2:	Continued	55
Table 3.3:	Formulation of Photocatalytic Membrane	67
Table 4.1:	Bandgap Energy for TiO <sub>2</sub> and N, S-CQDs/TiO <sub>2</sub> with Different Loading	72
Table 4.2:	Crystallite Size of TiO <sub>2</sub> and Different Loading of N, S-CQDs/TiO <sub>2</sub> Photocatalytic Membrane	75
Table 4.3:	Changes of Photodegradation Efficiency under UV Light Irradiation	84
Table 4.4:	Changes of Photodegradation Efficiency under Visible Light Irradiation	85

Table 4.5:	Changes of Photodegradation Efficiency under Environment Light Irradiation	85
Table 4.6:	Contact Angle of Different Type of MMM	89
Table 4.7:	Porosity and Mean Pore Radius of Different Mixed Matrix Membrane Based on Load Pressure of 1 bar	91

## LIST OF FIGURES

Figure 1.1:	Major Sources and Pathways of Pharmaceutical Waste in Global Environment (Rehman, <i>et al.</i> ,2015)	1
Figure 1.2:	River Water Quality Trend from Year 2012 to 2016 in Malaysia (DOE, 2016)	3
Figure 1.3:	Mean Concentration of Four Types of Pharmaceutical Waste in Three Different River (Praveena, <i>et al.</i> ,2018)	4
Figure 1.4:	Statistics on Number of Publications from Year 2000 to Year 2018 on Applications of AOPs for Pharmaceutical Degradation (Kanakaraju, Glass and Oelgemöller, 2018)	8
Figure 2.1:	Mechanism of Photocatalysis Reaction (Byrne, Subramanian and Pillai, 2017)	14
Figure 2.2:	Basic Principle of Porous Membrane Processes (Z FCui, Jiang and Field, 2010)	15
Figure 2.3:	Slurry PMR with External Membrane Filtration (Iglesias, <i>et al.</i> ,2016).	22
Figure 2.4:	Slurry PMR with Submerged Membrane Filtration (Iglesias, <i>et al.</i> ,2016)	22
Figure 2.5:	Configuration of Photocatalytic Membrane (Xu, <i>et al.</i> ,2018)	23
Figure 2.6:	Three Types of Semiconductor Heterojunctions Structure (Pirhashemi, Habibi-Yangjeh and Rahim Pouran, 2018)	33
Figure 2.7:	Photocatalysis Water Splitting Reaction of Modified Photocatalyst with Halogen in Water (M.Wang, <i>et al.</i> ,2018)	35
Figure 2.8:	Schematic diagram for the Photoexcited Charge Carrier Separation and Transport Process in Ru/g-C <sub>3</sub> N <sub>4</sub> /TiO <sub>2</sub> nanocomposite (Jiang, <i>et al.</i> ,2018)	37
Figure 2.9:	Crystal Structure of TiO <sub>2</sub> for Rutile (a), Brookite (b) and Anatase (c) (Bagheri, <i>et al.</i> ,2015)	39

Figure 2.10:	Schematic Diagram for Photocatalytic Mechanism of Ag doped TiO <sub>2</sub> Photocatalysts (Chang and Cho, 2016)	40
Figure 2.11:	Schematic Diagram Illustration of Photocatalytic Reaction Mechanism of g-C <sub>3</sub> N <sub>4</sub> /V <sub>o</sub> -ZnO Hybrid Photocatalyst Under Visible Light Irradiation (Y.Liu, <i>et al.</i> ,2015)	42
Figure 2.12:	Photodegradation Mechanism of CuO/SmFeO <sub>3</sub> nanocomposite for RhB Dye Under Visible Light Irradiation (Behzadifard, Shariatinia and Jourshabani, 2018)	44
Figure 2.13:	Schematic Diagram of Photodegradation Mechanism For N/TiO <sub>2</sub> /RGO Nanocomposite (Zhang, Yang and Park, 2018)	46
Figure 2.14:	Schematic Diagram of Photodegradation Mechanism of N-TiO <sub>2</sub> /NG for MB Under Visible Light Irradiation (Liu, <i>et al.</i> ,2016)	48
Figure 2.15:	Chemical Structure of CQDs (Lim, Shen and Gao, 2015)	49
Figure 2.16:	Schematic Chemical Structure of CQDs Formed From Two Different Approaches (Namdari, Negahdari and Eatemadi, 2017)	50
Figure 3.1:	Overall Flow Diagram of the Research	56
Figure 3.2:	Reflux Process to Produce Yellowish brown N, S-CQDs Photocatalyst Solution	57
Figure 3.3	Fabrication Process of Photocatalytic Membrane; (a) Preparation of Membrane Casting Solution (b) Membrane Casting Using the Casting Blade (c) In-situ Phase Inversion Process in Water Bath	59
Figure 3.4:	FTIR Peak Assignment for PSF Membrane (Kuvarega, <i>et al.</i> ,2018)	62
Figure 3.5:	Measurement of Membrane Thickness Using Dial Gauge Thickness	64
Figure 3.6:	Schematic Illustration of Photocatalysis Experiment; (a) Visible Light Irradiation (b) UV Light Irradiation (c) Environment Light Irradiation	65
Figure 3.7:	Experimental Set Up of Permeation Flux Test	66

Figure 3.8:	Calibration Curve for DCF Model Pollutant	70
Figure 3.9:	FYP II Schedule	70
Figure 4.1:	UV-Vis Absorption (ABS) Spectra of TiO <sub>2</sub> and Different Loading of NCQDs on N, S-CQDs/TiO <sub>2</sub> Composite	72
Figure 4.2:	FTIR Spectra of Pure and Photocatalytic PSF Membrane in the Wavelength Range Between 500–3900 cm <sup>-1</sup> .	73
Figure 4.3:	FTIR Spectra of Pure and Photocatalytic PSF Membrane in the Wavelength Range Between 500–2500 cm <sup>-1</sup> .	74
Figure 4.4:	FTIR Spectra of Pure and Photocatalytic PSF Membrane in the Wavelength Range Between 2500–3900cm <sup>-1</sup> .	74
Figure 4.5:	XRD Patterns of TiO <sub>2</sub> and N, S-CQDs/TiO <sub>2</sub> Composites with Different Amount of NCQDs	76
Figure 4.6:	SEM Images of Photocatalytic Membrane; (a) TiO <sub>2</sub> (b) 1.0g N, S-CQDs/TiO <sub>2</sub> (c) 1.5g N, S-CQDs/TiO <sub>2</sub> (d) 2.0g N, S-CQDs/TiO <sub>2</sub>	77
Figure 4.7:	SEM Image of Cross Sectional View of TiO <sub>2</sub> Membrane at Four Magnification; (a) ×500 (b) ×1000 (c) ×1500 (d) ×5000	78
Figure 4.8:	SEM Image of Cross Sectional View of 1.0g N, S-CQDs/TiO <sub>2</sub> Membrane at Four Magnification; (a) ×500 (b) ×1000 (c) ×1500 (d) ×5000	78
Figure 4.9:	SEM Image of Cross Sectional View of 1.5g N, S-CQDs/TiO <sub>2</sub> Membrane at Four Magnification; (a) ×500 (b) ×1000 (c) ×1500 (d) ×5000	79
Figure 4.10:	SEM Image of Cross Sectional View of 2.0g N, S-CQDs/TiO <sub>2</sub> Membrane at Four Magnification; (a) ×500 (b) ×1000 (c) ×1500 (d) ×5000	79
Figure 4.11:	EDX Analysis; (a) TiO <sub>2</sub> Membrane (b) 1.0g N, S-CQDs/TiO <sub>2</sub> Membrane (c) 1.5g N, S-CQDs/TiO <sub>2</sub> Membrane (d) 2.0g N, S-CQDs/TiO <sub>2</sub> Membrane	80

- Figure 4.12: Photocatalytic Degradation of DCF Pharmaceutical Waste in the Presence of  $\text{TiO}_2$  and N, S-CQDs/ $\text{TiO}_2$  Membrane with Different Amount of NCQDs under UV Light Irradiation. 85
- Figure 4.13: Photocatalytic Degradation of DCF Pharmaceutical Waste in the Presence of  $\text{TiO}_2$  and N, S-CQDs/ $\text{TiO}_2$  Membrane with Different Amount of NCQDs under Visible Light Irradiation. 86
- Figure 4.14: Photocatalytic Degradation of DCF Pharmaceutical Waste in the Presence of  $\text{TiO}_2$  and N, S-CQDs/ $\text{TiO}_2$  Membrane with Different Amount of NCQDs under Environment Light Irradiation. 86
- Figure 4.15: Photocatalytic Degradation of DCF Pharmaceutical Waste in the Presence of 1.5g N, S-CQDs/ $\text{TiO}_2$  Membrane with Different Membrane Area under Environment Light Irradiation. 87
- Figure 4.16: Plots of  $\ln(C_0/C)$  Versus Irradiation Time of  $\text{TiO}_2$  and N, S-CQDs/ $\text{TiO}_2$  with Different NCQDs Loading under Environment Light Irradiation. 88
- Figure 4.17: Pure Water Flux of  $\text{TiO}_2$  and N, S-CQDs / $\text{TiO}_2$  UF Membrane with Different Amount of NCQDs. 91
- Figure 4.18: Schematic Illustration of the Proposed Photocatalytic Mechanism of N, S-CQDs/ $\text{TiO}_2$  MMM under Environment Light Irradiation. 93

## LIST OF SYMBOLS / ABBREVIATIONS

$A$	effective filtration area, 0.001256 m <sup>2</sup>
$\beta$	full width at half maximum, FWHM
$c$	light velocity, $3 \times 10^8$ m/s
$C$	DCF concentration, mg/L
$C_o$	initial DCF solution concentration after adsorption equilibrium in dark, mg/L
$C_t$	DCF concentration at time t, mg/L
$d$	crystallite size, nm
$\mathcal{E}$	membrane porosity
$E^o$	reduction potential
$E_f$	fermi energy
$E_g$	bandgap energy, eV
$H^+$	hydrogen ions
$h$	planck's constant, $4.1359 \times 10^{-15}$ Js
$J_v$	membrane permeation flux at time t, L/m <sup>2</sup> hr
$k$	CuK $\alpha$ constant, 0.94
$k$	reaction rate constant of surface active site, mg/L min
$k_{app}$	apparent rate constant of first order
$K$	langmuir adsorption equilibrium constant of DCF, L/mg
$l$	membrane thickness, m
$\lambda$	absorption threshold wavelength, m
$\cdot O_2^-$	superoxide radicals
$\cdot OH$	hydroxyl radicals
$\Delta P$	load pressure, Pa
$q$	volume of permeate water per unit time, m <sup>3</sup> s <sup>-1</sup>
$r_m$	mean pore radius, m
$\rho_c$	density of PSF, 1.24 g/cm <sup>3</sup>
$\rho_H$	density of water, 0.998 g/cm <sup>3</sup>
$r$	reaction rate, mg/L min
$\theta$	angle between incoming X-ray and reflected lattice plane
$t$	filtration time, hr
$t$	treatment time, minutes

$\mu$	water viscosity, $8.9 \times 10^{-4}$ Pa s
$V$	volume of permeate, L
$W_d$	weight of dry membrane, g
$W_w$	weight of wet membrane, g
AgNCs	silver nanocrystals
AgNO <sub>3</sub>	silver nitrate
Al <sub>2</sub> O <sub>3</sub>	alumina
AMW	antibiotic manufacturing waste
AOPs	advanced oxidation processes
APIs	active pharmaceutical ingredients
ARB	antibiotic resistant bacteria
ARGs	antibiotic resistance genes
BZF	bezafibrate
C	copper
CA	citric acid
CB	conduction band
CBZ	carbamazepine
CDs	carbon dots
CdNO <sub>3</sub>	cadmium nitrate
CdS	cadmium sulphite
CH	co-hydrolysis
CNT	carbon nanotube
CQDs	carbon quantum dots
Cu	copper
Cu <sub>2</sub> O	copper oxide
DCF	diclofenac
EPMCs	emerging pharmaceutical manufacturing countries
Fe <sub>2</sub> O <sub>3</sub>	iron oxide
FTIR	fourier transform infrared spectroscopy
G	glucose
GO	graphene oxide
H <sub>3</sub> BO <sub>4</sub>	boric acid
HNO <sub>3</sub>	nitric acid

H <sub>2</sub> O <sub>2</sub>	hydrogen peroxide
HOMO	highest energy occupied molecular orbital
HPC	hydroxypropyl cellulose
H <sub>3</sub> PO <sub>4</sub>	phosphoric acid
H <sub>2</sub> SO <sub>4</sub>	sulphuric acid
HTC	hydrothermal carbonization
LPD	liquid phase deposition
LPM	low pressure membrane
LSPR	localized surface plasmon resonance
LUMO	lowest energy unoccupied molecular orbital
MAH	microwave assisted heating
MB	methylene blue
MF	microfiltration
MIP	molecular imprinted polymer
MMM	mixed matrix membrane
MO	methyl orange
MPG-C <sub>3</sub> N <sub>4</sub>	mesoporous graphite carbon nitride
MSW	municipal solid waste
N	nitrogen
NaOCl	sodium hypochlorite
Na <sub>2</sub> S	sodium sulfide
NCQDs	nitrogen doped carbon quantum dots
NF	nanofiltration
NGR	nitrogen doped graphene
(NH <sub>4</sub> ) <sub>2</sub> TiF <sub>6</sub>	ammonium hexafluorotitanate
NMP	N-methyl-2-pyrrolidone
NSAIDs	non-steroidal anti-inflammatory drugs
N, S-CQDs	nitrogen, sulphur doped carbon quantum dots
O	oxygen
PAA	porous anodic alumina
PANI	polyaniline
PES	polyethersulfone
PMR	photocatalytic membrane reactor
PRO	propanolol

PSF	polysulfone
Pt	platinum
PtSe <sub>2</sub>	platinum doped selenide
PVC	polyvinyl alcohol
PVDF	polyvinylidene fluoride
QY	quantum yield
RGO	reduced graphene oxide
Rh	rhodium
RhB	rhodamine B
Ru	ruthenium
S	sulphur
SEE	simultaneous electrospinning and electrospaying
SEM-EDX	scanning electron microscope equipped with energy dispersive X-ray
SHFM	submerged hollow fiber membrane
Si	silicon
SmFeO <sub>3</sub>	samarium orthoferrite
SMX	sulfamethoxazole
SO <sub>2</sub>	sulfone
SS	sewage sludge
SWCA	static water contact angle
Ti	titanium
TiF <sub>4</sub>	titanium tetrafluoride
TiO <sub>2</sub>	titanium dioxide
TMP	transmembrane pressure
UCPL	up-converted photoluminescence
UF	ultrafiltration
UTI	urinary tract infection
UV	ultraviolet
UV-VIS	ultraviolet visible
UWTPs	urban wastewater treatment plants
VB	valence band
WO <sub>3</sub>	tungsten trioxide
WWTP	wastewater treatment plant

XRD	X-ray diffraction
Zn	zinc
ZnO	zinc oxide

## CHAPTER 1

### INTRODUCTION

#### 1.1 Global Water Pollution from Pharmaceutical Waste

Water pollution is one of the most concern environmental problem which is caused by human activities or natural sources. With the rapid development of biomedical science and pharmaceutical industry, worldwide production and consumption of pharmaceuticals increased tremendously. The sources of water pollution with pharmaceuticals may include municipal sewage, animal wastes in live-stocks farming, patient waste by hospitals and pharmaceutical manufacturing industry as shown in Figure 1.1. The most often detected classes of pharmaceuticals found are non-steroidal anti-inflammatory drugs (NSAIDs), beta-blockers, antibiotics, neuroleptics, hormones and lipid regulators (Feier, *et al.*,2018). The discharge of pharmaceutical waste from various sources will flow into urban wastewater treatment plants (UWTPs). From the treated wastewater effluent, high concentration antibiotics and drugs which ranged from few ng/L to tens of  $\mu\text{g/L}$  can be found due to their overdose and inefficiency removal by conventional processes applied in UWTPs (Gao, *et al.*,2018; Karaolia, *et al.*,2018). The present of antibiotics will result in antibiotic resistant bacteria (ARB) and selection of antibiotic resistance genes (ARGs) which can harm humans and animals especially in outbreak of diarrhea and communicable diseases (Rizzo, *et al.*,2013; Friedman, Temkin and Carmeli, 2016).

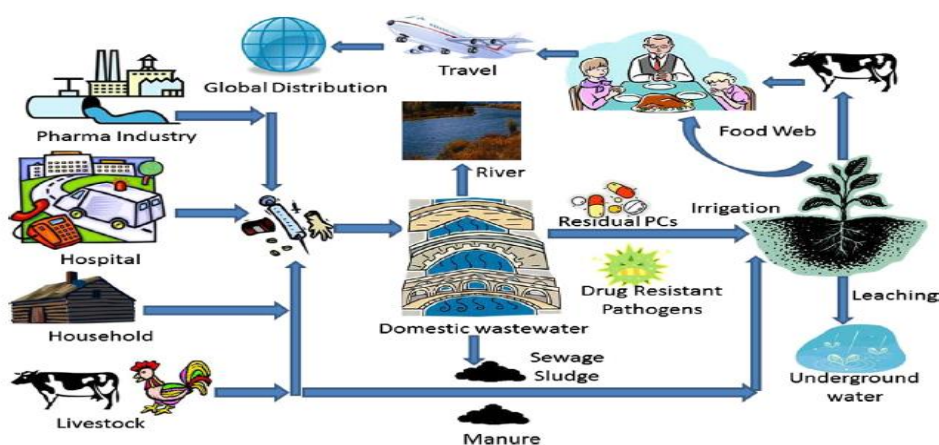


Figure 1.1: Major Sources and Pathways of Pharmaceutical Waste in Global Environment (Rehman, *et al.*,2015)

Lien, *et al.* (2016) found that high concentration of antibiotics resistant bacteria and genes found in UWTPs mostly come from hospital effluent. Referring to the study by He, *et al.* (2016), annual antibiotics consumption reaches 10 – 20 million kg worldwide. Rehman, *et al.* (2015) found that China, India, Pakistan and Bangladesh are identified as emerging pharmaceutical manufacturing countries (EPMCs) in the world. Among these four countries, China is the world largest producer and consumer of antibiotics. This is due to lower pharmaceutical production cost, easy clinical trials and growing market. This implied that China has become largest world's production of antibiotic manufacturing wastes (AMW). Zhang, *et al.* (2015) found that 92700 tonnes of antibiotics were consumed in 2013 with almost 46% of antibiotics were released into rivers through sewage effluent. This value is expected to be higher in 2018 due to 12.9 % of pharmaceutical industry annual growth in China (Rehman, *et al.*,2015). In developing country such as Malaysia, misuse, overuse and damping of antibiotics frequently occur (Okon, *et al.*,2014). Thus, antibiotic resistance has become the most important challenge as the existing antimicrobial drugs could not effectively treat against disease agent (Dires, *et al.*,2018).

## **1.2 Water Pollution in Malaysia**

Rapid industrial development in Malaysia brought overall economic development of the country by providing plenty of job opportunities, improve infrastructural development and socioeconomic. However, it brings adverse effects to the environment such as water pollution. Water pollution mostly caused by the discharge of the industrial effluent such as heavy metals, suspended solids, pharmaceutical waste and other compounds into river stream without proper treatment. Figure 1.2 shows water quality based on 140 rivers in Malaysia. According to Figure 1.2, the number of clean rivers started to decrease from 74 to 62 at year 2013 while number of slightly polluted river continuously increased since 2012. On the other hand, the polluted rivers significantly decreased from 12 to 5 since 2014 and increased back to 10 at year 2016. The large decrement of polluted rivers was due to stringent environmental regulations imposed by government on manufacturing industry (Malaysia, 2015).

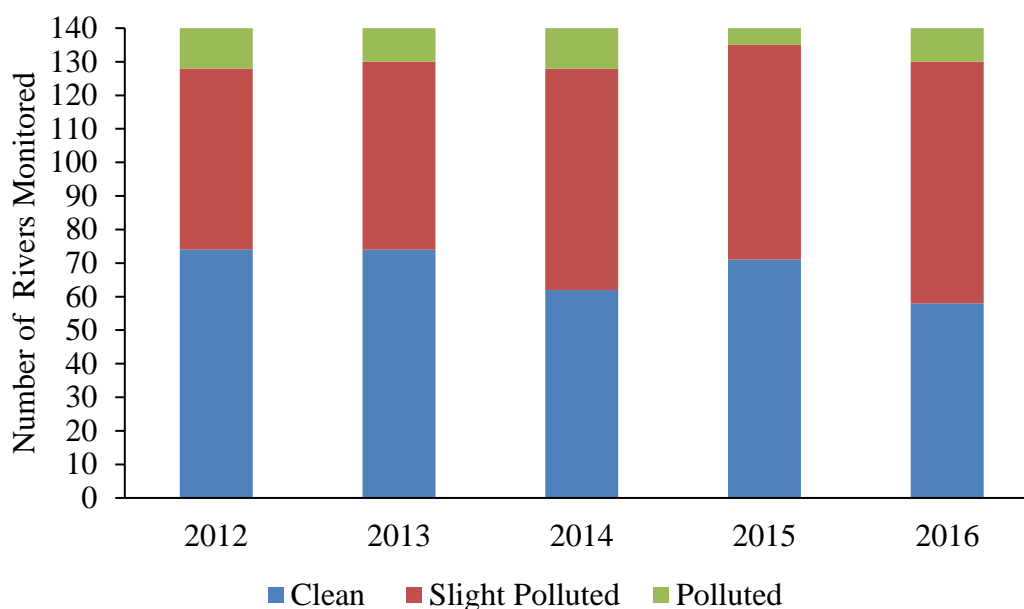


Figure 1.2: River Water Quality Trend from Year 2012 to 2016 in Malaysia (DOE, 2016)

Chan, *et al.* (2017) found that the prevalence of public health problem such as overweight or obesity has reached epidemic levels in Malaysia and others developing countries. Therefore, various communicable disease such as type II diabetes and heart disease related to overweigh increase and the demand for human pharmaceuticals to control these disease become high in Malaysia. As a result, more often for the continuous exposure of pharmaceutical waste in aquatic environment and groundwater system. The raw water which is polluted by pharmaceutical waste will then be treated and supply as drinking water to residential area. The drinking water will consists of ARB and ARGs if conventional drinking water treatment system not able to completely remove all the antibiotics. Referring to the study by Praveena, *et al.* (2018), surface water samples that collected from rivers at three different locations in Malaysia were analysed. Lui River which was exposed to anthropogenic activities such as agricultural, urbanization and residential areas (Riad, *et al.*,2004). Selangor River which exposed to domestic sewage, runoff from agriculture land, untreated pharmaceutical industrial effluent, oil palm and rubber plantations. Gombak River which exposed to several private clinics, hospitals, medical analysis laboratory, domestic effluent discharges and industrial effluent. Figure 1.3 presents pharmaceutical mean concentration for the three rivers. Ciprofloxacin is an antibacterial agent which is widely used to treat urinary tract infection (UTI),

nitrofurazone is an antimicrobial agent, sulfamethoxazole (SMX) is an antibiotic and diclofenac (DCF) is non-steroidal anti-inflammatory drugs. Based on Figure 1.3, Gombak River has higher pharmaceutical waste concentrations compared to Lui River and Selangor River. These pharmaceutical wastes mostly can be found in medical centre along Gombak River. Based on three different rivers, the mean DCF concentrations is the less among four types of pharmaceutical substances due to strictly prohibition of DCF imposed by government since 2010. DCF is ranked as top three drugs that are frequently used in Malaysia since 2010 and more likely can be misused and abused (Ministry of Health Malaysia, 2014). This is because DCF is the most inexpensive drug and available in retail pharmacies which allow to be used as self-medication.

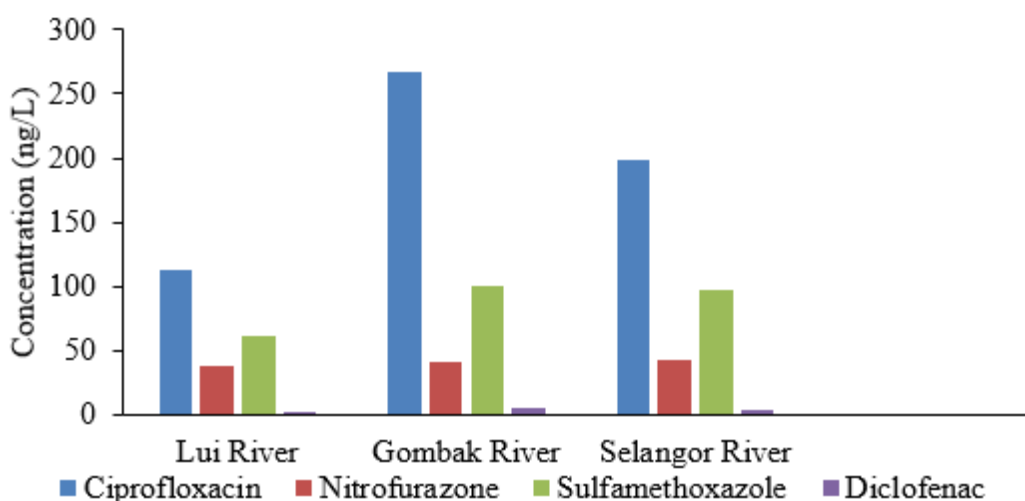


Figure 1.3: Mean Concentration of Four Types of Pharmaceutical Waste in Three Different River (Praveena, *et al.*,2018)

### **1.3 Types and Environmental Impacts of Pharmaceutical Compounds**

Pharmaceutical compounds consists of active pharmaceutical ingredients (APIs) which give a negative impact to the environment due to their continuous presence in groundwater, surface water and drinking water (Kanakaraju, Glass and Oelgemöller, 2018). They can enter the aquatic environment by various routes such as domestic wastewater, pharmaceutical industry, hospitals, clinics and animal breeding farms (Nikolaou, Meric and Fatta, 2007). Environmentally concerning groups of pharmaceutical compounds consists antibiotics, NSAIDs and analgesics,  $\beta$ -blockers, anticonvulsants and lipid regulators. Table 1.1 shows various type of pharmaceutical compounds with their impact to the environment. Therefore, it shall be removed from water.

Table 1.1: Impacts of Pharmaceutical Compounds on Environment

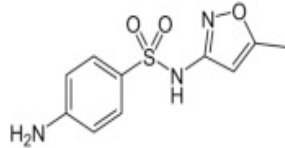
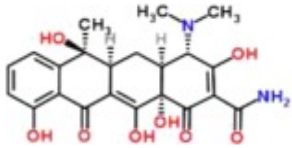
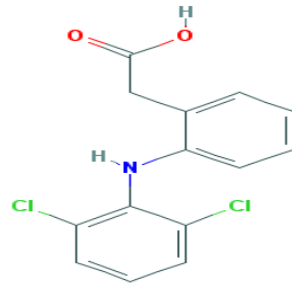
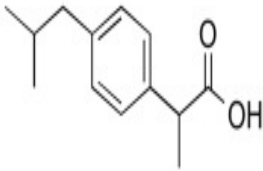
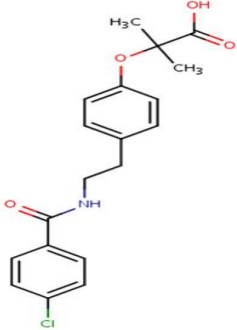
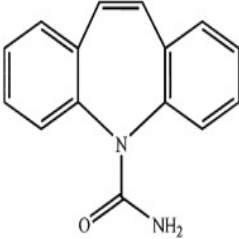
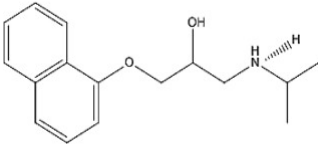
Therapeutic Class	APIs	Chemical Structure	Impacts	References
Antibiotics	SMX		Resistance among bacterial pathogens which altered microbial community structure that affect higher food chain.	(Witte, 1998)
	Tetracycline			
NSAIDs	DCF		DCF absorbed into soil and may leach out to groundwater causing accumulated toxic effects and ultimately to drinking water.	(Lonappan, <i>et al.</i> ,2016)
	Ibuprofen		Toxicity of ibuprofen cause oxidative stress, DNA damage and haematological changes in aquatic organisms	(Mathias, <i>et al.</i> ,2018; Vulava, <i>et al.</i> ,2016)

Table 1.1: Continued

Therapeutic Class	APIs	Chemical Structure	Impacts	References
<b>Lipid Regulators</b>	Bezafibrate (BZF)		Bioaccumulation and biomagnification of BZF could damage the DNA of aquatic organism due to additive effects and possible mixture toxicity. This will affect quality of drinking water and cause harmful to human.	(Gałęcki, et al.,2016; Isidori, et al.,2007)
<b>Anticonvulsants</b>	Carbamazepine (CBZ)		CBZ can cause acute and chronic toxicological effect on aquatic organism and several side effects on human such as headaches and vomiting	(Rajendran and Sen, 2018; Wang and Wang, 2017)
<b>β-blockers</b>	Propranolol (PRO)		PRO has the highest acute and chronic toxicity which will harm aquatic organisms and then affect human health such as growth and reproduction rate	(Huggett, et al.,2002; Fent, Weston and Caminada, 2006; El-Abasawi, et al.,2018)

#### 1.4 Advanced Oxidation Processes (AOPs)

Owing to the non-biodegradable nature, high stability and pseudo persistence of APIs, the conventional wastewater treatment plant (WWTP) fails to completely remove these APIs. Therefore, APIs are suspected to cause toxic effects on living organisms through raw water source even the concentration is as low as ng/L (Feier, *et al.*,2018). Therefore, there is an increase of emerging technologies like advanced oxidation processes (AOPs) to overcome the inefficiency of conventional WWTP for eliminating pharmaceuticals from water. AOPs involve the use of hydroxyl radicals that generated from oxidation-reduction techniques to treat or degrade pharmaceuticals (Bansal, Verma and Talwar, 2018). Figure 1.4 presents the number of researchers studied on the applications of AOPs in eliminating pharmaceuticals. Based on the statistics, it can be observed that the number of publications at year 2017 was the highest. It can be expected that pharmaceuticals pollution become an arising concern since year 2013 until year 2017.

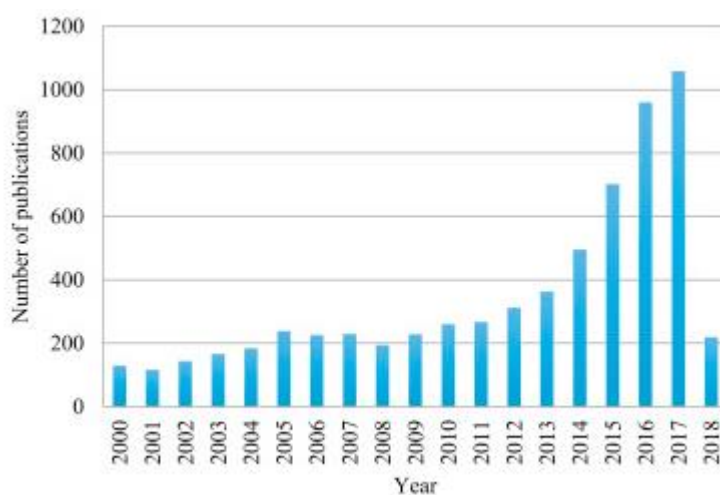


Figure 1.4: Statistics on Number of Publications from Year 2000 to Year 2018 on Applications of AOPs for Pharmaceutical Degradation (Kanakaraju, Glass and Oelgemöller, 2018)

AOPs can be divided into two groups depending on mode of activation, photochemical and non-photochemical methods. AOPs technologies include Fenton, photo-Fenton, ozonation, UV radiation, photocatalysis, sonolysis and electrochemical oxidation. Fenton process can remove pharmaceuticals in water to trace level but the efficiency is greatly affected by  $H_2O_2$ , Fe (II) dosage and solution pH where greater

degradation efficiency only can occur at optimal solution pH between 2 and 4 (Trapido, *et al.*,2009). The enhancement of Fenton process is photo-Fenton where UV-Vis light is employed to generate radicals. Although photo-Fenton can be effective at neutral pH compare to Fenton, it also need hydrogen peroxide which is extremely toxic to produce hydroxyl radicals. Both ozonation and UV radiation can effectively remove treat pharmaceutical compounds in water but the maintenance, construction and energy cost to operate is high (Matamoros, García and Bayona, 2008). Ma (2012) found that water sonolysis often generate insufficient hydroxyl radical to degrade pharmaceuticals. Besides, sonolysis process is difficult to control as it required stable sonication frequency (12-868 kHz) and ultrasound power density (25-100 W/L) (Adityosulindro, *et al.*,2017). In electrochemical oxidation, electrode material require large amount of electricity for oxidization of water to generate sufficient amount of hydroxyl radical (Liu, *et al.*,2018). Among all the AOPs, photocatalysis is more suitable to be used to treat pharmaceuticals in water because it only need UV or visible light source and water as precursors to produce hydroxyl radical. Referring to the study by Szabó, *et al.* (2011), most of the semiconductor use UV light irradiation to generate hydroxyl radical due to high energy radiation. However, long term exposure to UV radiation can cause adverse effect to human. Thus, modification of semiconductor has been done to extend the light absorption wavelength to visible light range.

## 1.5 Problem Statement

Water scarcity remains a huge challenge which can affect accessibility to safe drinking water. According to the sustainable development goal 6 which was established by United Nation at 2015, approximately 884 million people have no access to safe and affordable drinking water even though several efforts have been carried out to supply clean drinking water to rural area (United Nations, 2018). Active pharmaceutical ingredients were extremely non-biodegradable and pseudo persistent in the environment. According to Rosman et al. (2018), conventional treatment technologies ineffectively remove pharmaceutical waste exist in drinking water and surface water. Incomplete removal of pharmaceuticals in aquatic environment will lead to the formation of ARB and ARGs which will cause harmful to human. Therefore, it was essential to eliminate pharmaceuticals in water to trace amount.

Referring to the study by Rosman, *et al.* (2018), membrane filtration technology have been developed to remove pharmaceuticals due to significantly low energy consumption, flexible and simple process. However, membrane technology are susceptible to membrane fouling which lead to decrease in permeate flux and higher cleaning cost are required to regenerate the membrane. Therefore, integration of membrane technology with AOPs technology into one system called photocatalytic membrane could overcome the drawback from both technology. The drawback from membrane technology is membrane fouling that will decrease the permeate flux. Drawback from AOPs technology is agglomeration of photocatalyst which can cause formation of intermediate product due to incomplete photodegradation process. The formation of intermediate products can lead to toxic accumulation in water which may affect photocatalyst activity. AOPs rely on formation of hydroxyl radicals to oxidize the pharmaceuticals into small size and less harmful product. By coupling with membrane technology, photocatalysts will be evenly dispersed in the membrane. Therefore, intermediate product from water will be adsorbed onto the membrane and further oxidized by photocatalysts immobilized in the membrane to form non-toxic products which ensure complete photodegradation process occur. The integration system are able to concentrate the pollutants near the photocatalysts surface and reduce membrane fouling. Based on the above statement, semiconductor need to be modified by incorporation of membrane system to improve the photocatalytic performance. The mostly used semiconductor is titanium dioxide ( $\text{TiO}_2$ ) due to good stability, inexpensive and photocatalytic performance. On the other hand, polymeric membrane

such as PSF is used to support TiO<sub>2</sub> photocatalysts. The idea of combining both technology is due to agglomeration of photocatalyst in suspension and membrane fouling problem.

Referring to the study by J.Zhang, *et al.* (2016), sunlight irradiation usually comprises of 45 % of visible light and 5 % of UV light. However, wider band gap energy of TiO<sub>2</sub> greatly limit the light absorption efficiency. This is because most of the semiconductor only activated solely by UV light with a wavelength less than 400 nm. Therefore, we try to improve the electrical properties of TiO<sub>2</sub> semiconductor in this study by coupled with nitrogen and sulphur doped carbon quantum dots (N, S-CQDs) from concentrated acid and raw egg yolk sources.

The effect of various operating parameters such as NCQDs loading on N, S-CQDs/TiO<sub>2</sub>, photo sources, transmembrane pressure (TMP) on permeation flux and and photocatalytic membrane area were unknown. The efficiency of photocatalytic membrane could be determined by finding its apparent reaction rate constants. Besides, further study was required for the kinetic of N, S-CQDs/TiO<sub>2</sub> hybrid photocatalyst on the photodegradation of DCF using pseudo first order kinetic equation.

## 1.6 Objectives

The objectives for this research were:

- To synthesize and characterize N, S-CQDs/TiO<sub>2</sub> photocatalysts in terms of band gap energy.
- To incorporate N, S-CQDs/TiO<sub>2</sub> into PSF membrane by in-situ phase inversion method and characterize the photocatalytic membrane in terms of hydrophilicity, chemical functional group, morphology and crystalline structure.
- To investigate the photodegradation efficiency of N, S-CQDs/TiO<sub>2</sub>/PSF membrane under various conditions such as loading of NCQDs on N, S-CQDs/TiO<sub>2</sub> on PSF membrane, types of photo sources and photocatalytic membrane area.
- To study the reaction kinetic on photocatalytic degradation reaction of DCF.

### 1.7 Scope and Limitation of the Study

This work was to fabricate N, S-CQDs/TiO<sub>2</sub> PSF MMMs and study its photocatalytic degradation and permeation flux performance under various operating condition such as NCQDs loading, type of photo sources, effect of TMP and surface area of MMM. N, S-CQDs/TiO<sub>2</sub> PSF MMMs were fabricated by dip coating the synthesized PSF membrane into N, S-CQDs/TiO<sub>2</sub> sol which also called as in-situ phase inversion. In order to achieve the objectives stated previously, the scope of this study were listed as follows:

- i. Determine the optimum dosage of NCQDs and maximum light absorption wavelength of N, S-CQDs/TiO<sub>2</sub> sol.
- ii. Identify the performance of fabricated MMMs in terms of membrane porosity and pure water permeation flux using dead end filtration system.
- iii. Perform photodegradation test of N, S-CQDs/TiO<sub>2</sub> MMMs under different NCQDs loading, photo sources and surface area of MMMs and determine the optimum conditions.
- iv. Determine the apparent reaction rate constant using pseudo first order kinetic equation.

There were few limitations existed in this study which listed as follows:

- i. The polluted water from pharmaceutical manufacturing industry usually contains a high concentration of various contaminants which are not easily to be degraded and filtered. Hence, in this work, only one type of pharmaceutical waste with insignificant concentration of 10 ppm was used as model pollutant.
- ii. The by-products produced from photodegradation process was difficult to be detected. Thus, this research only focused on photodegradation rate instead of type of by-products obtained.
- iii. The pure water permeation flux performance were affected by few operating parameters, including TMP, membrane casting velocity, composition and temperature of membrane dope solution. Due to limited duration to complete this study, this research was only focused on TMP.

## CHAPTER 2

### LITERATURE REVIEW

#### 2.1 Photocatalysis Reaction

Heterogeneous photocatalysis is an AOP based on the use of ultraviolet (UV) radiation (sunlight) and a semiconductor (photocatalyst) to generate oxidizing and reducing species (Molinari, Lavorato and Argurio, 2017). The most widely used semiconductors include zinc oxide (ZnO), cadmium sulfite (CdS), and TiO<sub>2</sub>. Among them, TiO<sub>2</sub> is the most commonly used photocatalyst due to its high reusability, low cost metal oxide, suitable band gap, chemical stability and has excellent effectiveness in degradation of organic pollutants (Iglesias, *et al.*, 2016). Band gap energy ( $E_g$ ) is the difference in energy between top of the valence band (VB) filled with electron and bottom of the conduction band (CB) devoid of electron (Evingür and Pekcan, 2016).  $E_g$  is the important parameter in fabricate photocatalyst because it can affect the efficiency of electron hole pairs separation (Zhong, *et al.*, 2017).

The basic principle of photocatalytic degradation is same as the photocatalytic water splitting reaction but the final product is different. Photocatalytic water splitting is the release of hydrogen and oxygen from water under redox reaction and lead to the formation of active species include hydroxyl radicals ( $\cdot\text{OH}$ ), hydrogen peroxide (H<sub>2</sub>O<sub>2</sub>) and superoxide radicals ( $\cdot\text{O}_2^-$ ) (Wang, Tadó and Shao, 2018). On the other hand, photocatalysis reaction takes place at the surface of the semiconductor. The process is illustrated in Figure 2.1. The electronic structure of photocatalyst can be classified by CB and VB which are separated by  $E_g$  (Byrne, Subramanian and Pillai, 2017). Photocatalysis reaction is triggered when photocatalyst is being bombarded by photons produced from UV radiation. If the absorption energy of photon is greater than the  $E_g$ , the electron on the surface of photocatalyst is excited from VB to CB leading to the formation of free electron hole pair. As a result, a positive hole is formed in the VB (Janssens, *et al.*, 2017). Oxidation of water take place at the positive hole in VB and producing  $\cdot\text{OH}$  and hydrogen ion (H<sup>+</sup>) (Salim, *et al.*, 2018). At conduction band, reduction take place and photo excited electron will react with oxygen (O<sub>2</sub>) to produce  $\cdot\text{O}_2^-$  which is the reactive oxygen species. Both  $\cdot\text{O}_2^-$  and  $\cdot\text{OH}$  are effective to degrade pollutant into harmless carbon dioxide and water.

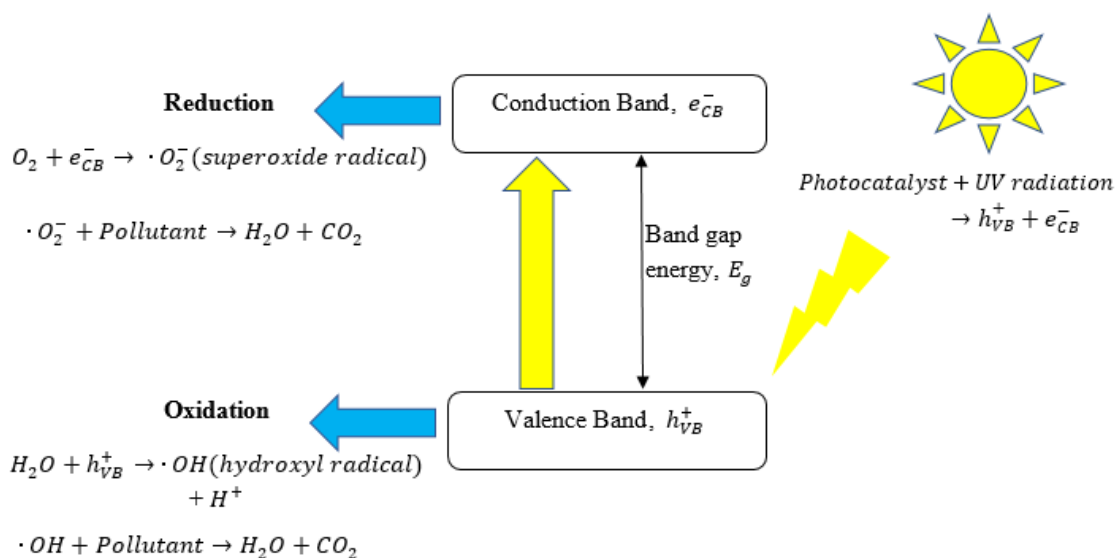


Figure 2.1: Mechanism of Photocatalysis Reaction (Byrne, Subramanian and Pillai, 2017)

Organic dye such as Rhodamine B (RhB) can be degraded by  $TiO_2$ . Firstly, absorption of photons with energies larger than  $E_g$  of  $TiO_2$  which is 3.2eV lead to the generation of electron and hole (Dong, *et al.*,2018). Photo excited electron will undergo reduction to produce  $\cdot O_2^-$  while hole will undergo oxidation to produce  $\cdot OH$ . Both  $\cdot O_2^-$  and  $\cdot OH$  have powerful capability for oxidizing and destroying organic dye at the surface of  $TiO_2$ . RhB will then undergo mineralization and non-selective degradation by this pool of reactive transients (Pang and Abdullah, 2013). Besides, hole can directly oxidize RhB adsorbed on the surface of photocatalyst or degrade them indirectly through  $\cdot OH$  generated by reaction of hole because free RhB is more accessible to  $\cdot OH$  radical oxidation (Shabat-Hadas, Mamane and Gitis, 2017).

## 2.2 Membrane Filtration

Membrane is a layer of thin semi-permeable material with much smaller pores that can be described as conventional filter to separate tiny particles when a driving force is applied cross the membrane. Membrane processes able to transfer specific compounds selectively and can easily to be scaled up due to their compact and modular design (Onsekizoglu, *et al.*,2015). There are two types of membrane separation techniques which are dead end filtration and cross flow filtration (Djennad, Benachour and Schomäcker, 2012). Dead end filtration is a batch process which feed flow accumulate on the membrane surface and lead to formation of thick filter cake. Cross flow refers

to permeate flow and retentate flow direction have a  $90^\circ$  angle. Cross flow filtration is the flow of feed by pressure as driving force and will not lead to accumulation of filter cake. In general, membrane can be classified as porous and nonporous. Porous membrane operate on pore size exclusion while nonporous membrane do not operate on a size exclusion mechanism (Z. F.Cui, Jiang and Field, 2010). The most commonly used membrane are microfiltration (MF) ultrafiltration (UF) and nanofiltration (NF) which are based on pressure driven techniques such as (Mozia, *et al.*,2015). The working mechanism of membrane is illustrated in Figure 2.2. Pressure difference between both sides of membrane allow suspension (Mixture A and B) to pass through the membrane. Solute (Component B) will be retained and solvent (Component A) will pass through the membrane depending on the porous size.

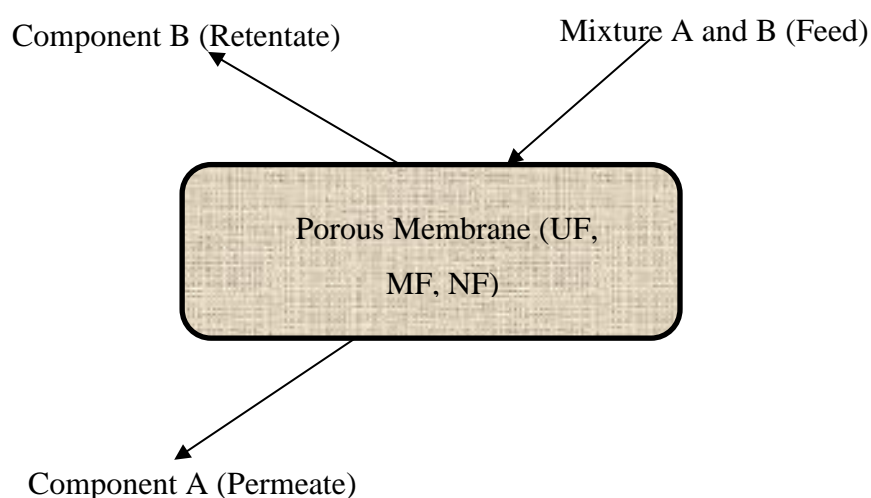


Figure 2.2: Basic Principle of Porous Membrane Processes (Z FCui, Jiang and Field, 2010)

Some important criteria to be considered for membrane selection are the capacity to completely reject catalyst, controlling membrane fouling and low concentration polarization which will result in reduced permeation flux. Membrane fouling is the accumulation of microorganisms, organic and inorganic compounds and colloidal matter on membrane surfaces and pores (Shamsuddin, Das and Starov, 2015). There are two types of membrane which are polymeric membrane and ceramic membrane. Polymeric membrane are more preferred due to their lower cost compare to ceramic membrane (Iglesias, *et al.*, 2016). However, polymeric membrane has low resistance to strong acid solvents, shorter lifetime, high water flux, low mechanical strength and not able to persist in high temperature condition (Ko, *et al.*, 2018). Ceramic membrane is made from one or more layer of chemically and thermally stable metal oxide materials such as alumina ( $\text{Al}_2\text{O}_3$ ) and  $\text{TiO}_2$  that have macroporous support to provide mechanical support (Hubadillah, *et al.*, 2018). Both types of membrane have excellent mechanical strength and durability. Table 2.1 shows the characteristic for different type of membrane.

Table 2.1: Characteristics and Physical Properties for Polymeric and Ceramic Membrane

Membrane Material	Most Common Use	Advantages	Disadvantages	References
<b>Polymeric Polyvinylidene Fluoride (PVDF)</b>	MF / UF	<ul style="list-style-type: none"> <li>• Superior thermal, chemical stability</li> <li>• Solvent and oxidant resistance</li> </ul>	<ul style="list-style-type: none"> <li>• High fouling ability</li> <li>• Low permeability</li> <li>• Wider pore size distribution</li> </ul>	(Lv, et al.,2018; Warsinger, et al.,2018)
<b>Polymeric Polysulfone (PSF)</b>	MF / UF	<ul style="list-style-type: none"> <li>• High pH and harsh chemicals resistance</li> <li>• Good mechanical and thermal properties</li> </ul>	<ul style="list-style-type: none"> <li>• Low resistance to fouling due to hydrophobic nature</li> </ul>	(Ravishankar, et al.,2018; Warsinger, et al.,2018)
<b>Polymeric Polyethersulfone (PES)</b>	MF / UF	<ul style="list-style-type: none"> <li>• High oxidative</li> <li>• Excellent chemical and thermal resistance</li> <li>• pH: 1 – 13</li> </ul>	<ul style="list-style-type: none"> <li>• High fouling ability which shorten lifespan of membrane</li> </ul>	(Zhang, et al.,2018; Kourde-Hanafi, et al.,2017; Warsinger, et al.,2018)
<b>Ceramic Al<sub>2</sub>O<sub>3</sub> / TiO<sub>2</sub></b>	MF / UF / NF	<ul style="list-style-type: none"> <li>• Better fouling and higher temperature resistance than polymeric membrane</li> </ul>	<ul style="list-style-type: none"> <li>• Higher cost</li> </ul>	(Wadekar and Vidic, 2018; Warsinger, et al.,2018)

### 2.2.1 Microfiltration (MF)

Low pressure membrane (LPM) process such as microfiltration can be applied in water and wastewater treatment for removal of suspended solid, microorganisms and particulates to produce high quality permeate. It is useful in suspensions separation which porous membrane is used to separate suspended particle within the size range between  $0.1 - 10\mu\text{m}$  (Dijkshoorn, *et al.*,2017). Hollow fiber membrane is most commonly used membrane for water purification compare to flat sheet and tubular type membrane because it can provide large membrane area in a limited space (Iio, *et al.*,2016). Technology for drinking water and wastewater treatment using submerged hollow fiber membrane (SHFM) system provide higher permeate quality, low energy consumption and greater packing density (Li, *et al.*,2016). However, membrane fouling problem remains an issue where membrane performance is reduced and operating cost is increased (Wu, *et al.*,2016). To overcome this, backwash or chemical wash are often used to mitigate membrane fouling. Permeate or filtrate is used during regular backwash while chemical such as sodium hypochlorite ( $\text{NaOCl}$ ) is added to filtrate to make backwash process more efficient for removing organic accumulation (Jung, *et al.*,2018). Periodic chemical cleaning is required to eliminate foulants that adsorbed on the membrane surface and form filter cake during filtration.

### 2.2.2 Ultrafiltration (UF)

UF membrane are often run in crossflow filtration mode which is more suitable for continuous separation. UF membrane with pore size between 1 nm and 100 nm are used in purifying of drinking water (potabilization) for removal proteins, bacteria, virus, silica, dyes, polysaccharides, colloids and considered a good barrier in nanometer scale (Gentile, *et al.*,2018). These organic compounds adhere on the membrane surface easily and cause membrane fouling. For an example, bacteria may adhere and continue to grow, forming a layer of biofilms on membrane surfaces which block the membrane pores and cause biofouling problem (Saeki, Minami and Matsuyama, 2017). PSF is usually used as polymeric matrix for fabrication of UF membrane because it has better thermal, chemical and mechanical properties incorporated with superior film forming capability. However, the hydrophobic nature of PSF may contribute to membrane fouling (Khan, *et al.*,2018). To overcome antifouling problem of UF membrane, zwitterionic membrane materials has been

developed. Chemical structure of zwitterionic polymer are hydrophilic, neutral charges, hydrogen bond acceptors but not hydrogen bond donors. From this characteristics, zwitterionic polymer can form hydration layer at membrane surface to avoid biofouling and adsorption of solutes and nonspecific protein (Huang, *et al.*,2018).

### 2.2.3 Nanofiltration (NF)

NF with a membrane pore size between 0.5 - 2.0 nm can separate mono and multi valent salts, and different size of organic molecules based on the electrostatic repulsive effect and steric hindrance effect (Ji, *et al.*,2017). Materials that often used to make NF membrane is polyethersulfone (PES) which has good thermal stability, ease of fabrication, better mechanical strength, good chemical resistance and high glass transition temperature (Tsehay, *et al.*,2018). However, the hydrophobic nature of PES can lead to membrane fouling which decline permeation flux, reduce membrane lifespan and increase operation cost (Zangeneh, *et al.*,2018). There are a wide range of inorganic nanomaterials have been incorporated in membrane matrix for modification of NF such as  $\text{Al}_2\text{O}_3$ ,  $\text{TiO}_2$ , carbon nanotubes (CNT) and iron oxide ( $\text{Fe}_2\text{O}_3$ ) nanoparticles which can reduce membrane fouling, improve permeability, increase chemical stability and reinforcing the rejection. Among these additives, graphene oxide (GO) is getting higher attention due to its large specific surface area, excellent adsorption of metal ions and greater mechanical strength (Bagheripour, *et al.*,2018). GO nanofiltration membrane can be prepared using electrospaying and traditional method such as vacuum and pressure assisted filtration method. GO nanofiltration membrane prepared from vacuum filtration have higher water flux which is  $21.8 \text{ Lm}^{-2}\text{h}^{-1}\text{bar}^{-1}$  and can reject more than 99% for organic dyes and 20 – 60% for salt ions (Han, Xu and Gao, 2013). GO nanofiltration membrane prepared from electrospaying have lower water flux which is  $11.13 \text{ Lm}^{-2}\text{h}^{-1} \text{bar}^{-1}$  and can remove nearly 100% for negatively charged organic dyes and more than 98% for positively charged organic dyes (Chen, *et al.*,2018). Vacuum filtration has higher water flux compare to electrospaying which means it can produced greater amount of permeate per unit area of membrane surface area per unit time. Vacuum filtration and electrospaying both has nearly complete solute rejection but vacuum filtration need higher pressure and longer process time. This is because higher mass transfer pressure during preparing a

thicker membrane. Therefore, electrospaying is better compare to vacuum filtration because more operation cost can be saved by electrospaying.

### 2.3 Photocatalytic Membrane Reactor (PMR)

Photocatalytic membrane reactor (PMR) is a hybrid system combining photocatalysis and membrane filtration techniques where a photocatalytic reactor links with membrane process to degrade the pollutant while simultaneously separate larger particles (Leong, et al.,2014; Phan, et al.,2017). PMR can be classify into two groups which are immobilized PMR and slurry PMR (Zhang, *et al.*,2016). Immobilized PMR is a photocatalytic reactor with photocatalysts immobilized on membrane while slurry PMR is a photoreactor with photocatalyst in liquid suspension. Photocatalysis system is one of the AOP which use of photocatalytic materials and light illumination to generate strong oxidizing or reducing radicals to degrade toxic organic compounds (Molinari, Lavorato and Argurio, 2017). On the other hand, membrane system is used to separate molecules present in the medium after treated by AOP, and acts as a barrier for photocatalyst particles and creates a possibility for its reuse (Szymański, Morawski and Mozia, 2018). Separation techniques used in PMR is based on pressure driven filtration using MF, UF and NF membranes (Darowna, *et al.*,2017).

Membrane technology has been most widely used to remove organic solutes with different size from one another. However, membrane separation efficiency will be decreased as larger size organic solutes accumulate on the membrane surface. This phenomenon is known as membrane fouling. Membrane fouling will lead to continuous decline of permeate flux over time and decrease the filtration efficiency as well as shorten the membrane lifespan. Besides, the formation of filter cake will lead to higher pressure drop which will increase energy consumption. Therefore, the combination of membrane process with AOPs would eliminate membrane fouling while removing pollutants through oxidation and reduction (Hatat-Fraile, *et al.*,2017). AOPs use generated  $\cdot\text{OH}$  and  $\cdot\text{O}_2^-$  as main oxidant and reductant for degradation of organic pollutant until their total mineralization to carbon dioxide, water and inorganic ions or small biodegradable molecules (Ganiyu, *et al.*,2015). Therefore, less membrane cleaning is required as well as increase permeate yield.

Figure 2.3 and 2.4 illustrate slurry PMR and immobilized PMR. Both slurry PMR and immobilized PMR have the same configuration with porous membrane, submerged lamp, mechanical stirrer, baffle and air sparger. Porous membranes with different pore sizes are to remove non-toxic and small biodegradable molecules. Submerged lamp provides light to excite the electrons of photocatalyst from valence band to conduction band leading to the formation of radicals. Mechanical stirrer is applied to ensure oxygen, photocatalysts and organic pollutants distributed homogeneously inside the photoreactor. Baffle between submerged lamp and stirrer is placed to prevent lamp damage and reduce vortexing problem. Air sparger is often implemented in PMR provide oxygen in air bubbles form to mitigate membrane fouling problem. This is because oxygen supplied can be utilized as electron acceptor to produce  $\cdot\text{O}_2^-$  to breakdown organic pollutants into smaller molecules through reduction (Çelik, Casey and Hasar, 2018).

The different between slurry PMR and immobilized PMR are membrane arrangement and photocatalyst form. For slurry PMR, photocatalysts is suspended in organic matter solution inside photoreactor and membrane module is placed after photoreactor. For immobilized PMR, photocatalysts are incorporated with porous membrane to produce photocatalytic membrane and is submerged into the photoreactor. In term of photocatalysts separation, slurry PMR can separate and recover photocatalyst effectively due to an additional photocatalyst separation channel while separation or recycling of photocatalyst are not required in the immobilized PMR (Zhang, *et al.*,2016). Therefore, slurry PMR has higher degree of membrane fouling which reduce permeate flux due to catalyst penetration while membrane in immobilized PMR can be used as long as catalytic activity remains high. However, photocatalysts in immobilized PMR will loss under long term operation. Iglesias, *et al.* (2016) explained that immobilized PMR is preferable due to lesser space requirement and less membrane fouling problem. As a result, lower maintenance and operation cost is required.

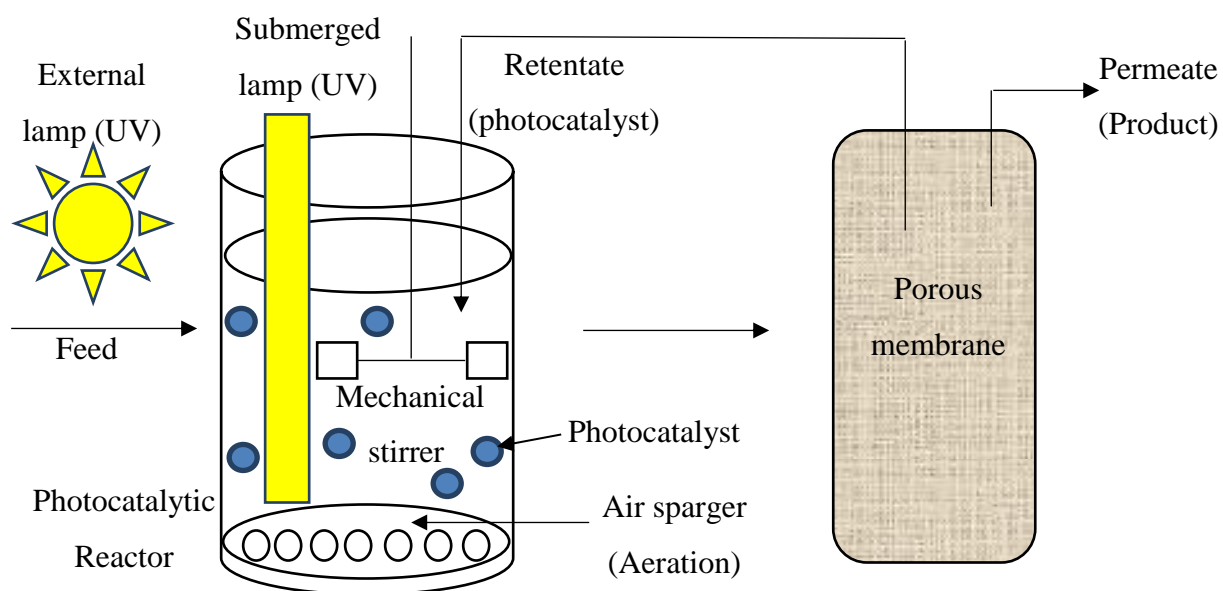


Figure 2.3: Slurry PMR with External Membrane Filtration (Iglesias, *et al.*,2016)

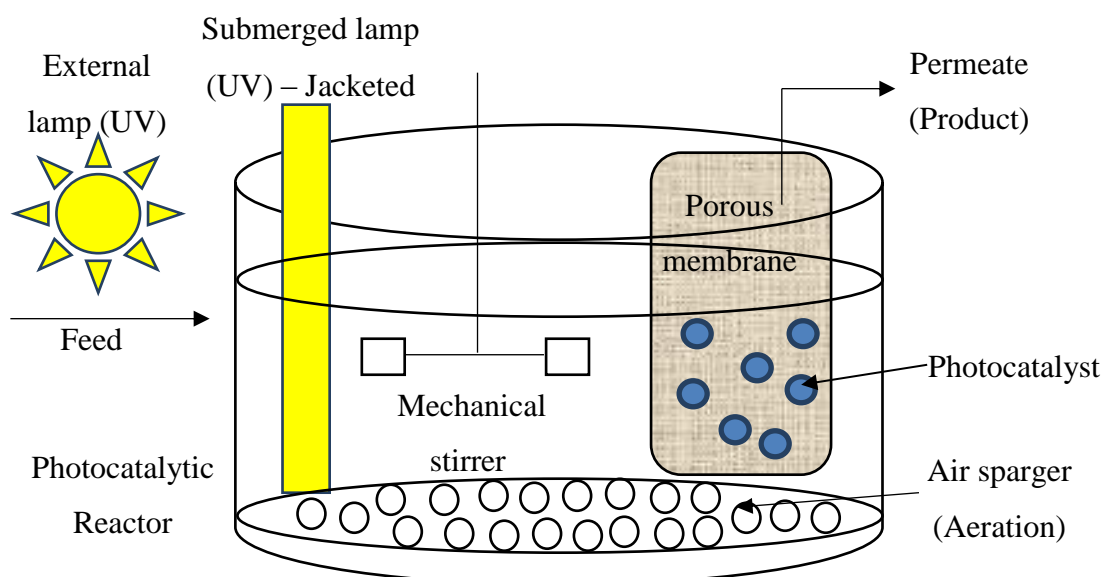


Figure 2.4: Slurry PMR with Submerged Membrane Filtration (Iglesias, *et al.*,2016)

## 2.4 Photocatalytic Membrane

Photocatalytic membrane is the incorporation of photocatalyst in membrane for photocatalysis process. Figure 2.5 present configuration of photocatalytic membrane. Photocatalytic membrane can be defined as a supported photocatalysts layer on porous membrane that undergo photocatalytic activity under visible light or UV irradiation (Zhang, Wang and Diniz Da Costa, 2014). Photocatalysts generate radicals which are the strongest oxidant and reductant to degrade pollutants into simple, smaller and harmless inorganic molecules without generating secondary waste (Leong, *et al.*,2014). The generation of radicals can be initiated by energy source such as UV light, visible light, ultrasonic and heat. Membrane is able to immobilize and protect the photocatalyst as well as act as a separation barrier for reaction products (Molinari, *et al.*,2002). As a result, photocatalysts couple with membrane able to concentrate pollutants near the catalyst surface and reduce membrane fouling (Starr, *et al.*,2016).

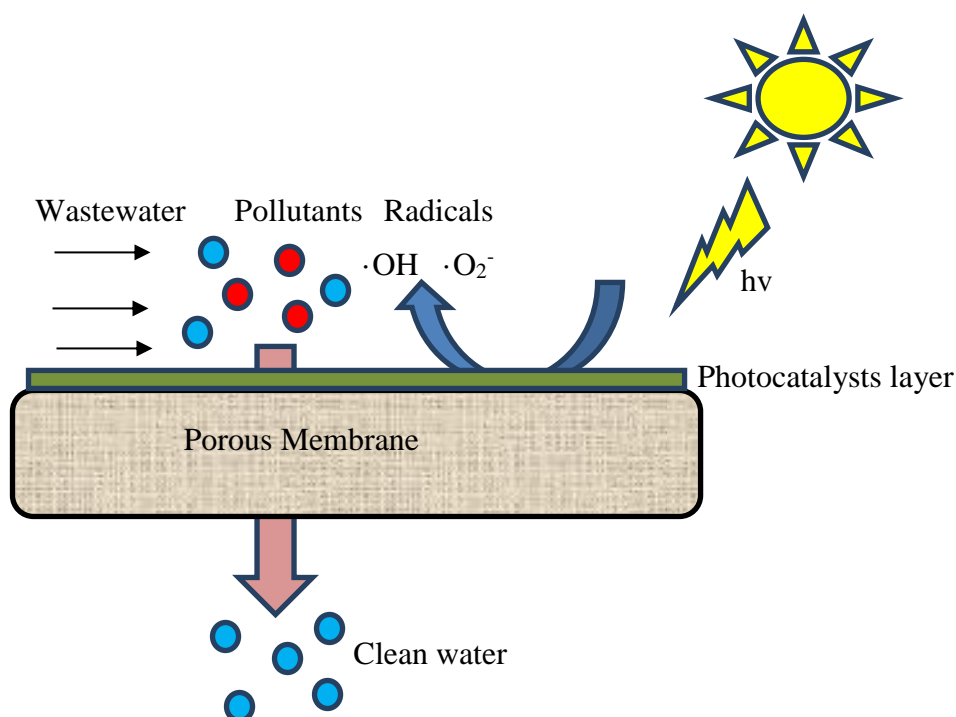


Figure 2.5: Configuration of Photocatalytic Membrane (Xu, *et al.*,2018)

Table 2.2 summarizes the photocatalysis performance of photocatalytic membrane by the immobilization of various photocatalyst.

Table 2.2: Applications of Photocatalytic Membrane in the Photodegradation of Pollutants

Photocatalyst	Membrane	Process Condition	Main Results	References
<b>1% Mesoporous Graphite Carbon Nitride/Titanium Dioxide Nanoparticle (mpg-C<sub>3</sub>N<sub>4</sub>/TiO<sub>2</sub>)</b>	PSF polymeric UF membrane	Pollutants: Antibiotic, sulfamethoxazole (SMX) pH: - Light: UV Light intensity: 300 W Wavelength: 270 nm	<ul style="list-style-type: none"> <li>69% of SMX degraded after 30 hours of consecutive irradiation.</li> <li>Lower contact angle of 58.1° which increase membrane hydrophilicity</li> </ul>	(Yu, <i>et al.</i> ,2018)
<b>2 wt.% Molecular Imprinted Polymer (MIP)-TiO<sub>2</sub> Nanoparticles</b>	PSF polymeric UF membrane	Pollutants: methylene blue (MB) and methyl orange (MO) pH: - Light: UV irradiation Light intensity: 10 W Wavelength: < 390 nm	<p><u>Without UV</u></p> <ul style="list-style-type: none"> <li>MB removal – 82.99 ± 8.61%</li> <li>MO removal – 28.40 ± 2.91%</li> </ul> <p><u>With UV</u></p> <ul style="list-style-type: none"> <li>MB removal – 96.90 ± 3.76%</li> <li>MO removal – 34.18 ± 7.45%</li> </ul>	(Melvin Ng, Leo and Abdullah, 2017)
<b>Zinc Oxide (ZnO) Nanowire Crystal</b>	Polypropylene (PP) polymeric MF membrane	Pollutants: MB and humic acid pH: 3 and 6 (neutral) Light: white light for MB and UV light for humic acid Light intensity: - Wavelength: 663 nm (white light) and 254 nm (UV light)	<p><u>pH 3</u></p> <ul style="list-style-type: none"> <li>MB degradation rate is 0.0214min<sup>-1</sup></li> <li>More than 50% loss of humic acid concentration</li> </ul> <p><u>pH 6</u></p> <ul style="list-style-type: none"> <li>MB degradation rate is 0.0143min<sup>-1</sup></li> <li>Less than 50% loss of humic acid concentration</li> </ul>	(Bojarska, <i>et al.</i> ,2017)

Table 2.2: Continued

Photocatalyst	Membrane	Process Condition	Main Results	References
<b>2 wt.% Silver Nanocrystals (AgNCs) Doped on Polymeric Graphite Carbon Nitride (g-C<sub>3</sub>N<sub>4</sub>)</b>	Nafion polymeric membrane	Pollutants: RhB pH: Light: visible light Light intensity: 500W Wavelength: $\geq 420$ nm	<ul style="list-style-type: none"> <li>AgNCs / g- C<sub>3</sub>N<sub>4</sub> / Nafion hybrid membrane shows better degradation rate than g- C<sub>3</sub>N<sub>4</sub> and g- C<sub>3</sub>N<sub>4</sub> / Nafion membrane</li> <li>Good durability and recycling stability</li> </ul>	(H.Zhang, <i>et al.</i> ,2018)
<b>0.6 at. % Nitrogen (N) Doped TiO<sub>2</sub></b>	Al <sub>2</sub> O <sub>3</sub> ceramic MF membrane	Pollutants: Antiepileptic drug, carbamazepine (CBZ) pH: - Light: UV light and visible light Light intensity: 300W Wavelength: 320 nm – 400 nm (UV light) and 400 nm – 700 nm (visible light)	<ul style="list-style-type: none"> <li>N-doped TiO<sub>2</sub> / Al<sub>2</sub>O<sub>3</sub> shows better photocatalytic activity than TiO<sub>2</sub> / Al<sub>2</sub>O<sub>3</sub> under both UV and visible light irradiation</li> <li>Degradation rate of CBZ increased with temperature while decreased with dissolved oxygen concentration</li> </ul>	(Horovitz, <i>et al.</i> ,2016)

## 2.5 Fabrication of Photocatalytic Membrane

Photocatalytic membrane can be organized into two classes based on the membrane materials which are inorganic membranes and inorganic polymer hybrid membrane (Zhang, Wang and Diniz Da Costa, 2014). Inorganic membrane is the membrane that made of ceramics, nanoporous carbon and metal oxide. Inorganic polymer hybrid membrane is the membrane that made of inorganic material and polymer materials such as PSF, PES, cellulose acetate and polycarbonate. Methods to fabricate photocatalytic membrane include sol – gel method, liquid phase deposition (LPD) method, hydrothermal carbonization (HTC), microwave irradiation, anodization and simultaneous electrospinning and electrospraying (SEE).

Sol – gel method involves two phases: solution and gelation. Sol is a colloidal suspension of photocatalyst particles whereas gel is an interconnected network of photocatalysts particles (Owens, *et al.*,2016). Sol – gel process has several advantages such as chemical homogeneity, low cost and low calcination temperature (Salavati-Niasari, *et al.*,2016). Therefore, less amount of heat required due to low calcination temperature properties. Taking  $\text{TiO}_2$  photocatalytic membrane as an example, sol – gel process begins with hydrolysis of  $\text{TiO}_2$  to form a sol. Then,  $\text{TiO}_2$  coated on porous support by dip coating. Finally, it is calcinated to produce a supported anatase form  $\text{TiO}_2$  membrane. In a study by Habibpanah, et al. (2011),  $\text{TiO}_2 - \text{Al}_2\text{O}_3$  composite sol prepared by co – precipitation sol – gel or co – hydrolysis (CH) process. Then, prepared sol is heating at  $80 - 85\text{ }^\circ\text{C}$  for few hour and electrostatically peptized, stabilized by nitric acid which followed by one day refluxing. In order to create a crack free top layer on  $\text{Al}_2\text{O}_3$  substrates, solution of hydroxypropyl cellulose (HPC) and polyvinyl alcohol (PVC) are added to dipping sol as binders. Photocatalytic membrane formed by dip – coating the  $\text{Al}_2\text{O}_3$  support in the prepared sol.

LPD is a low temperature deposition process that involves hydrolysis and direct deposition reaction of metal – fluoro complex without any heating process (Lin, Wu and Huang, 2018). Taking  $\text{TiO}_2 / \text{Al}_2\text{O}_3$  photocatalytic membrane as an example,  $\text{TiO}_2$  thin film is produced by hydrolysis of ammonia added titanium tetrafluoride ( $\text{TiF}_4$ ). Then, the thin film is grafted through heterogeneous nucleation on the surface of  $\text{Al}_2\text{O}_3$ . Finally, nanotube photocatalytic membrane is obtained after the  $\text{TiO}_2$  thin film is removed from  $\text{Al}_2\text{O}_3$  membrane surface. LPD method has several advantages such as large area, simplicity, high selectivity and ease in changing film composition

(Huang, Lin and Wu, 2017). On the other hand, Park, *et al.* (2017) explained that preparation of TiO<sub>2</sub> thin films by 0.3 M boric acid (H<sub>3</sub>BO<sub>3</sub>) and 0.1 M ammonium hexafluorotitanate (NH<sub>4</sub>)<sub>2</sub>TiF<sub>6</sub> that separately dissolved in deionized water at 50 °C and stirred. Then, silicon (Si) wafer which treated by oxygen plasma and immersed into the prepared solution at 50 °C. As a result, TiO<sub>2</sub> nucleate on Si support for specific time to form TiO<sub>2</sub> / Si photocatalytic membrane.

HTC is a thermochemical conversion technique which use subcritical water to transform wet and dry biomass into energy and chemicals without pre-drying (Wang, *et al.*,2018). Besides, HTC often take place in autoclave with carbonization of precursors under pressure. Carbonization can be modified by integrated with pressuer to improve carbon yield, to obtain specific particle morphology of resultant carbons and to densify resultant carbon (Inagaki, Park and Endo, 2010). Biomass used in HTC process usually include sewage sludge (SS), food waste, lignocellulose and municipal solid waste (MSW) (Zhou, Engler and Nelles, 2018). The solid product from HTC process is hydro char that is attractive because it can reduce the cost of raw materials and properties can be engineered for different applications such as production of carbon quantum dots (CQDs) (Jain, Balasubramanian and Srinivasan, 2016). Referring to the study by Shen, *et al.* (2018), TiO<sub>2</sub> can be coupled with CQDs to enhance the photocatalytic activity. Both citric acid (CA) and glucose (G) can be selected as carbon precursors to synthesize CQDs. In the experiment, CA or G are dissolved in deionized water and transferred into autoclave for heating under pressure. The solution is heated to 170 °C for 12 hours. Then, the obtained solution is filtered and undergo dialysis to obtain purified CQDs. After that, purified CQDs couple with TiO<sub>2</sub> to prepare CQDs doped TiO<sub>2</sub> composites by heating at 150 °C for 6 hours.

Microwave is the electromagnetic wave with a frequency between 300 MHz - 300GHz and the wavelength in the range between 1m – 1mm. Microwave irradiation also known as non-contact treatment technology which is a highly effective heating source in chemical reactions because it can provide better yields, accelerate reaction rate and give uniform and selective heating (Wang and Chen, 2018). Divya, *et al.* (2018) found that reduced graphene oxide (RGO) based composite with Ag nanoparticles can be fabricated through one step microwave irradiation and increased degradation efficiency. Firstly, RGO was synthesized using modified Hummer's method. Then, obtained RGO dissolved in water and mixture was sonicated to obtain

a uniform solution. After that, silver nitrate ( $\text{AgNO}_3$ ) and sodium borohydride was added into the solution. The mixture was sonicated and placed in microwave at  $120\text{ }^\circ\text{C}$  for 10 minutes. The reaction system was cooled to room temperature and washed with deionised water. Finally, RGO / Ag nanocomposites obtained after drying at  $80\text{ }^\circ\text{C}$ . In a study by Fan, *et al.* (2013), time consuming HTC process can be improved by using microwave as heating resource for HTC. Such system is called microwave assisted HTC (MAHTC). MAHTC combines the advantages of microwave heating and HTC which can rapidly achieve the high temperature and high pressure as well as shorten the preparation time in closed reaction system (Meng, *et al.*,2016).

Anodizing is the conversion coating of the surface of base metal such as aluminium, titanium and zinc and its alloys to porous metal oxide. In this process, metal base part to be coated becomes anode in electrolytic cell. According to Kandy and Gaikar (2018), growth of CdS nanorods photocatalyst on porous anodic alumina (PAA) support structure can improve photocatalytic reduction of carbon dioxide. There are several steps involve in fabrication of PAA membrane such as pre-treatment, first step anodization, chemical etching and second step anodization. Firstly, aluminium substrate undergo pre-treatment which include annealing at  $400\text{ }^\circ\text{C}$  for 3 hours under nitrogen and electropolishing using sulphuric acid ( $\text{H}_2\text{SO}_4$ ) and phosphoric acid ( $\text{H}_3\text{PO}_4$ ). Secondly, the pre-treated aluminium substrate undergoes first step anodization using digital power supply and electrolyte. Then, first step anodization followed by chemical etching to strip the oxide layer and second step anodization to form PAA membrane. After that, PAA membrane was sonicated to remove trapped air bubbles in pores structure. Finally, PAA membrane undergoes cationic adsorption cycle using cadmium nitrate ( $\text{CdNO}_3$ ) solution followed by anionic reaction using sodium sulfide ( $\text{Na}_2\text{S}$ ) to form CdS that precipitates within pores of membrane.

Electrospinning and electrospraying are electrohydrodynamic atomization process which polymer solution such as nylon-6 can be spun or sprayed by utilizing a high potential electric field to obtain particles or fibers (Zong, *et al.*,2018). Electrospinning involves evaporation of solvent followed by solidification of droplets to form charged solid fibers when an electrically charged solution is feed through small opening. On the other hands, electrospraying is an atomization method to disperse liquid into extremely fine charged droplets (Patil, *et al.*,2017). In a study by Pahasup-

anan, *et al.* (2017), fabrication of TiO<sub>2</sub> nanoparticles entrap under network of non-woven electrospun fiber membrane can be done in three layers. The base layer consists of nylon-6 electrospun fiber mat which prepared by electrospinning. The middle layer consists of nylon-6 nanofibrous network and anatase form TiO<sub>2</sub> which constructed by simultaneous electrospinning and electro spraying method. Final top layer was build up by nylon-6 electrospinning. This layer by layer method can gives an additional strength due to construction of multilayers thin films with different physical properties sandwiched between the layers.

Table 2.3 presents the performance and characteristics of photocatalytic membrane as prepared by different fabrication methods.

Table 2.3: Fabrication Methods for Photocatalytic Membrane

Fabrication Methods	Nanomaterials	Photocatalytic Membrane Characteristics	Performance	References
<b>Sol – gel (CH process)</b>	Al <sub>2</sub> O <sub>3</sub> / TiO <sub>2</sub> supported on Al <sub>2</sub> O <sub>3</sub> support	Pore size: 1 – 3 μm	95% decomposition of dyestuff (green malachite) after 3 hours exposure of UV irradiation	(Habibpanah, Pourhashem and Sarpoolaky, 2011)
<b>LPD</b>	TiO <sub>2</sub> supported on Ni substrate	Pore size: 1 μm	<u>After 6 hours nucleated TiO<sub>2</sub></u> <ul style="list-style-type: none"> <li>• Hardness and Young’s modulus increased.</li> <li>• Improved antibacterial effect</li> </ul>	(Park, <i>et al.</i> ,2017)
<b>HTC</b>	CQDs-G / TiO <sub>2</sub> and CQDs-CA/TiO <sub>2</sub>	Pore size: 2 – 4 nm for CQDs-CA and 3 -6 nm for CQDs-G	Slight cytotoxicity with less than 80% cell viability CQDs-G / TiO <sub>2</sub> has better photocatalytic activity than CQDs-CA/TiO <sub>2</sub> . It can reach about 99% of degradation ratio after 6 hours UV light exposure	(Shen, <i>et al.</i> ,2018)

Table 2.3: Continued

Fabrication Methods	Nanomaterials	Photocatalytic Membrane Characteristics	Performance	References
<b>Microwave Irradiation</b>	RGO / Ag nanocomposites	Pore size: -	RGO / Ag nanocomposites shows better photocatalytic degradation of RhB at 80 minutes under 550 nm wavelength of visible light.	(Divya, <i>et al.</i> ,2018)
<b>Anodization</b>	CdS supported on PAA	Pore size: 45 – 55 nm	Photocatalytic reduction of CO <sub>2</sub> to methanol (CH <sub>3</sub> OH) having efficiency of 45.4% and 1.97% of CO <sub>2</sub> conversion efficiency in a single pass.	(Kandy and Gaikar, 2018)
<b>SEE</b>	TiO <sub>2</sub> nanoparticles entrapped within nylon-6 electrospun fiber membrane	Pore size: 0.3 – 10 μm	More than 98% MB removal efficiency after 120 minutes of photocatalytic oxidation	(Pahasup-anan et al., 2017)

## 2.6 Classification of Photocatalysts

Photocatalysts are the substances that can carry out photocatalysis process to generate charge carrier in the presence of light. The charge carriers consist of electron and hole which are responsible for degradation of contaminants (Han, *et al.*, 2018). For unsupported catalyst, large number of electrons and holes are recombined with each other by relaxation of photogenerated electron in CB to VB and without participate in photocatalytic reaction. This is because kinetics for electron-hole recombination is much faster than interfacial charge transfer (Jo, *et al.*, 2018). Therefore, overall photocatalytic quantum efficiency is significantly hindered due to less number of photogenerated charge carrier on surface reaction sites to carry out photodegradation. Charge carrier recombination is the process of backward reaction of  $H_2$  and  $O_2$  to form  $H_2O$  (Wang, Tade and Shao, 2018). Referring to the study by Huang, *et al.* (2017), introduction of doping agents as cations or anions can narrow down the  $E_g$  level, improve light absorption for photocatalysis and make the recombination of photoinduced electrons and holes become difficult. In addition, doping can provide larger dipole moments to change the electron transfer kinetics and increase surface area of semiconductor (Ünlü, Çakar and Özacar, 2018). Thus, recombination rate of photogenerated electron and hole become low and more contaminants can be adsorbed. Some photocatalyst may be doped with two or three different semiconductors. The principle for hybrid photocatalyst is that at the interface between two semiconductors, photogenerated electron flow from more negative to less negative Fermi energy ( $E_F$ ) in CB while hole flow from more positive to less positive  $E_F$  in VB (Zhang and Jaroniec, 2018). The arrangement of semiconductor heterojunctions is classified into three categories based on their band gap energies as shown in Figure 2.6. In straddling gap structure (type 1), the CB of semiconductor 2 is more negative than semiconductor 1 and its VB is more positive than semiconductor 2. Based on the principle of charge carrier transfer, electron and hole will be accumulated in smaller  $E_g$  in semiconductor 1. Therefore, charge carrier recombination might occur due to smaller  $E_g$  which does not improve photocatalytic performance. In staggered gap structure (type 2), the CB of semiconductor 2 is more negative than semiconductor 1 and VB of semiconductor 1 is more positive than semiconductor 2. Therefore, electron will transfer from semiconductor 2 to semiconductor 1 while hole transfer from semiconductor 1 to semiconductor 2. In this type of arrangement, electron-hole separation is better

compare to type 1 because charge carriers are separated in two semiconductors respectively. In broken gap structure (type 3), both CB and VB of semiconductor 1 is lower than semiconductor 2. Therefore, both electrons and holes are not able to pass the interface to the respective bands of semiconductor. This is because the transport of charge carriers at interface is interrupted by energy barrier (Zhang and Jaroniec, 2018). Among three heterojunctions structure, type 2 semiconductor heterojunction structure is the most typical heterojunction system because it can promote efficiently separation of photogenerated electrons and prevent the charge carrier recombination in electron transfer process in order to improve the photocatalytic reaction (Chen, *et al.*,2008). For an example, Liu, *et al.* (2015) found that g-C<sub>3</sub>N<sub>4</sub> doped on copper(1) oxide (Cu<sub>2</sub>O) was fabricated by solvothermal and chemisorption process, which was confirmed to be type 2 heterojunction structure. This hybrid photocatalyst have better photocatalytic performance of H<sub>2</sub> generation reached 795 $\mu$ mol/g after 3 hours for degradation of contaminants under visible light irradiation.

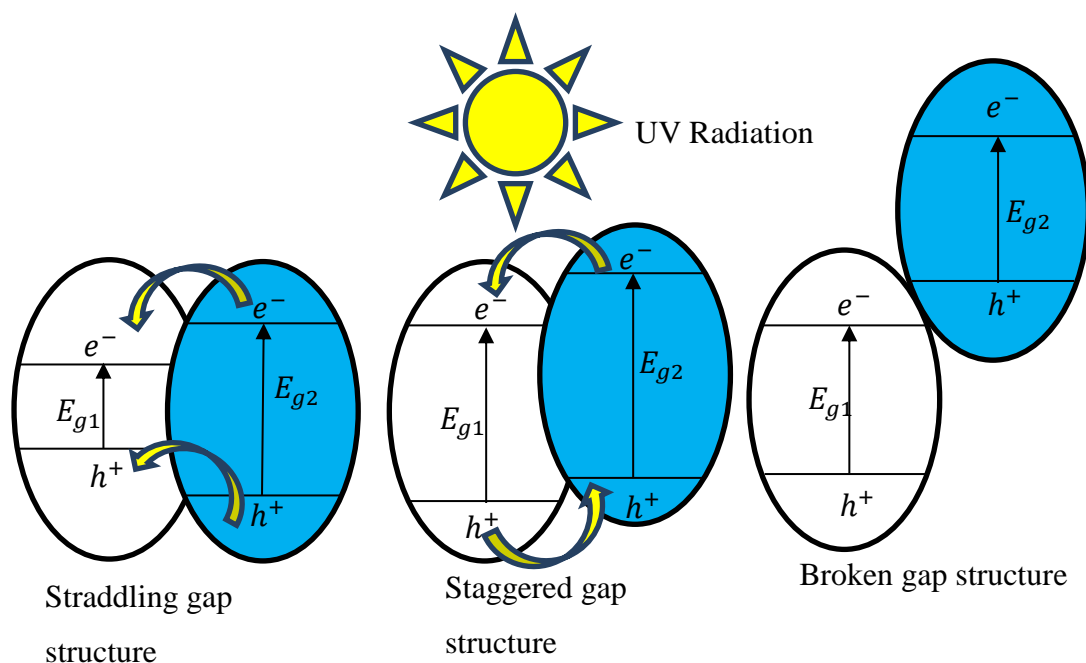


Figure 2.6: Three Types of Semiconductor Heterojunctions Structure (Pirhashemi, Habibi-Yangjeh and Rahim Pouran, 2018)

Table 2.4 presents photocatalyst which synthesis from different elements according to their physical and chemical properties.

Table 2.4: Various Type of Photocatalysts for Different Elements

<b>Elements</b>	<b>Photocatalysts</b>
<b>Noble Metal</b>	Platinum (Pt), Ruthenium (Ru) and Rhodium (Rh)
<b>Transition Metal</b>	Titanium (Ti), Zinc (Zn) and Copper (Cu)
<b>Non-metals &amp; Metalloid</b>	Nitrogen (N), Graphene, Carbon dots (CDs)

### 2.6.1 Platinum-Based Photocatalysts

Pt catalyst is the promising catalyst due to their superior properties in number of applications such as catalyst, biomedicine and electronics. However, Pt is a high cost metal which is not cost effective for industrial application. Among various type of noble metals, Pt is the most effective co-catalyst to extract photogenerated electron for reduction of contaminants due to its fast electron trapping from CB in semiconductor which prevent charge carrier recombination and improve photocatalytic performance (Xie et al.,2014; Atabaev et al.,2016). In this case, co-catalyst is a substance with small loading amount doped on the bulk photocatalyst to improve the photocatalytic performance.

Oh, *et al.* (2014) reported that fabrication of platinum doped metal selenide (PtSe<sub>2</sub>) supported on graphene through microwave assisted method can result in improvement of photocatalytic performance. The hybrid photocatalyst was tested towards organic dyes such as RhB and MB under visible light. They suggested that there were three steps involved in the decomposition of organic dyes. Firstly, adsorption of organic contaminants which lead to the increased concentration on photocatalyst surface. Next, light irradiation on PtSe<sub>2</sub> excite the electron from CB to VB leaving hole in VB. Thirdly, the excited electron from PtSe<sub>2</sub> is transferred to graphene sheet to react and degrade adsorb organic contaminants. Light irradiation on PtSe<sub>2</sub> due to smaller E<sub>g</sub> which can generate more electron in VB and transfer to graphene to be stored. Graphene sheet can prevent the recombination of electron-hole due to its higher E<sub>g</sub>. Electron that accumulated in graphene will undergo reduction to generate  $\cdot\text{O}_2^-$  which responsible for contaminants degradation. On the other hand, the

hole creating in VB of PtSe<sub>2</sub> will remain and undergo oxidation to produce ·OH for decomposition of contaminants.

Wang, *et al.* (2017) found that H<sub>2</sub> and O<sub>2</sub> undesired recombination reaction over Pt co-catalyst was due to their activation property for H<sub>2</sub> and O<sub>2</sub> to form water. This means less radical species being produced to degrade the organic pollutants which reduce the photocatalytic performance. Therefore, in a study by M.Wang, *et al.* (2018), halogen atom doped on Pt before support on photocatalyst can overcome water forming reverse reaction by inhibiting the adsorption and activation of H<sub>2</sub> and O<sub>2</sub> molecules to form water. Figure 2.7 illustrates the process for water hindering on halogen adsorbed Pt doped TiO<sub>2</sub>.

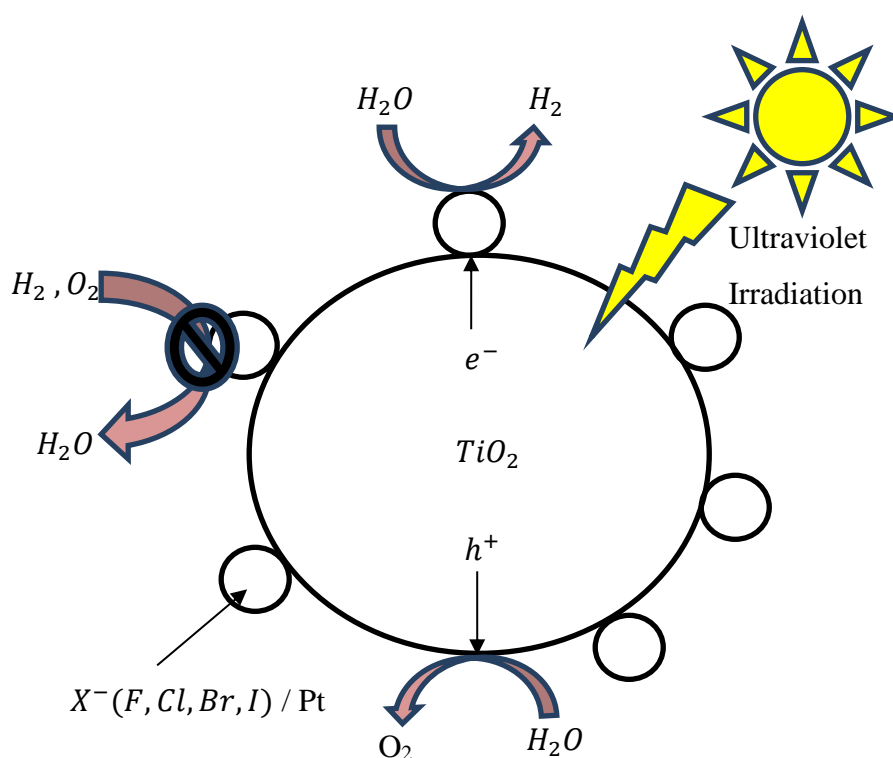
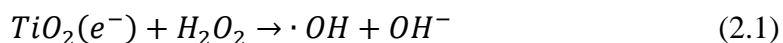


Figure 2.7: Photocatalysis Water Splitting Reaction of Modified Photocatalyst with Halogen in Water (M.Wang, *et al.*2018)

### 2.6.2 Ruthenium-Based Photocatalysts

Ru complex is the most widely used photosensitizer because prolonged lifetime can be obtained at the cost of reduced excited state energy, strong electron transporting ability and has good chemical stability (Wolpher, *et al.*,2004). Therefore, it has strong visible light absorption to generate more radical species for photodegradation of pollutants (Ozawa, *et al.*,2014). Besides, Ru photosensitizer unit have efficient and rapid electron transfer to another photocatalyst unit which can accelerate the photocatalysis and prevent recombination of charge carrier (Kumar, *et al.*,2018). Photosensitizers is a molecule that can absorb photons from visible light and transfer to another molecule to promote their chemical reaction but itself remain inert.

In a study by Jiang, *et al.* (2018), Ru complexes act as a photosensitizer was doped on the g-C<sub>3</sub>N<sub>4</sub> by using the amino groups of g-C<sub>3</sub>N<sub>4</sub> and become immobilized together. The synthetic Ru/g-C<sub>3</sub>N<sub>4</sub> then supported on TiO<sub>2</sub> by solvothermal synthesis to form ternary nanocomposite (Ru/g-C<sub>3</sub>N<sub>4</sub>/TiO<sub>2</sub>). The photocatalytic performance was tested by degradation of MB under visible light irradiation. Figure 2.8 illustrates the separation of electron-hole pairs over Ru/g-C<sub>3</sub>N<sub>4</sub>/TiO<sub>2</sub> nanocomposite. Firstly, irradiation of visible light on Ru complex (RuC<sup>2+</sup>) will produce RuC<sup>2+\*</sup> molecule in excited state. RuC<sup>2+</sup> have higher photocatalytic quantum efficiency due to strong visible light absorption and smaller E<sub>g</sub>. Therefore, more photogenerated electron being produced in CB of excited state of RuC<sup>2+\*</sup> molecule and transferred to CB of g-C<sub>3</sub>N<sub>4</sub> for stored. Next, g-C<sub>3</sub>N<sub>4</sub> will absorb visible light which excite the electron from VB to CB and leaving hole in VB. The photogenerated electron will converged on the surface of g-C<sub>3</sub>N<sub>4</sub> and combine with electron transferred from excited state of RuC<sup>2+\*</sup> molecule. The CB and VB edge potential for g-C<sub>3</sub>N<sub>4</sub> is -1.11eV and 1.56eV while for TiO<sub>2</sub> is -0.23eV and 2.85eV. Electron accumulated on the surface of g-C<sub>3</sub>N<sub>4</sub> will transferred to CB of TiO<sub>2</sub> due to more negative CB of g-C<sub>3</sub>N<sub>4</sub> as compare to TiO<sub>2</sub>. The electron accumulated on CB of TiO<sub>2</sub> will dissolved in oxygen and being reduced to form ·O<sub>2</sub><sup>-</sup> and further react to form H<sub>2</sub>O<sub>2</sub> and finally produce ·OH. On the other hand, the hole in the VB of g-C<sub>3</sub>N<sub>4</sub> cannot oxidize H<sub>2</sub>O to form ·OH for degradation of contaminants due to more negative VB edge potential than reduction potential (E<sup>0</sup>). In this case, E<sup>0</sup> is measure based on tendency of H<sub>2</sub>O<sub>2</sub> to get electron and reduced to produce active ·OH as shown in Equation 2.1.



Based on Equation 2.1, one mole of  $\text{H}_2\text{O}_2$  will acquire one mole of electron to form hydroxyl ion ( $\text{OH}^-$ ). Therefore,  $E^0$  can be calculated through division of  $\cdot\text{OH}$  by  $\text{OH}^-$ . However, holes in VB of  $g\text{-C}_3\text{N}_4$  also participate in pollutants degradation but the amount of  $\text{CO}_2$  and  $\text{H}_2\text{O}$  form is less compare to reduction reaction take place in CB of  $\text{TiO}_2$ .

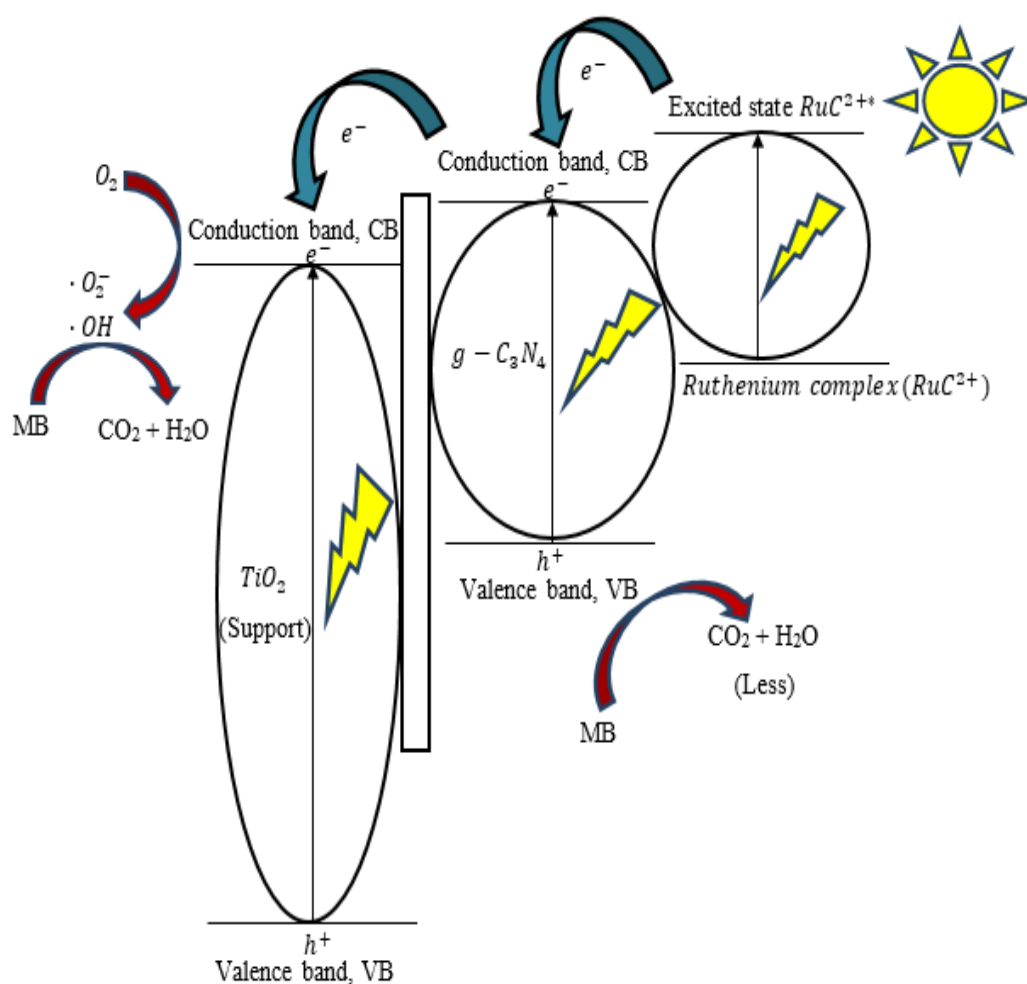


Figure 2.8: Schematic diagram for the Photoexcited Charge Carrier Separation and Transport Process in  $\text{Ru}/g\text{-C}_3\text{N}_4/\text{TiO}_2$  nanocomposite (Jiang, *et al.*, 2018)

### 2.6.3 Rhodium-Based Photocatalysts

Rh complexes based on transition metal of group 9 can be either four, five or six coordinated with oxidation states of  $\text{Rh}^{\text{I}}$ ,  $\text{Rh}^{\text{II}}$  and  $\text{Rh}^{\text{III}}$  in water and  $\text{Rh}^{\text{III}}$  hydride species is used for  $\text{H}_2$  evolution (Bakac, 2006). Rh complexes can be used as co-catalyst for  $\text{H}_2$  evolution due to good stability which are not oxidizable by water (Bion and Duprez, 2016).

Kitano, Hashimoto and Kominami (2011) found that photocatalyst of rhodium ion modifier ( $\text{Rh}^{3+}$ ) doped on  $\text{TiO}_2$  surface can have better photocatalytic performance. This is because  $\text{Rh}^{3+}$  can reduce the  $E_g$  of  $\text{TiO}_2$  which cause more generation of photogenerated electron for degradation of contaminants (Kitano, *et al.*,2016). This hybrid photocatalyst can be prepared by calcine  $\text{TiO}_2$  sample at various temperature in water bath. Then, the calcined samples modified with metal ions by adding aqueous solution of rhodium (III) chloride using the equilibrium adsorption method. Lastly, the suspension undergo filtration to obtain filter followed by drying overnight. The photocatalytic activity is tested by mineralization of gas phase acetone to  $\text{CO}_2$  over uncalcined and post-calcined  $\text{Rh}^{3+}/\text{TiO}_2$  in the presence of visible light irradiation. Post-calcined  $\text{Rh}^{3+}/\text{TiO}_2$  sample at  $350^\circ\text{C}$  has 1.5 times higher photocatalytic activity than uncalcined  $\text{Rh}^{3+}/\text{TiO}_2$  sample (Kitano, *et al.*,2017). On the other hand, Camposeco, *et al.* (2018) found that Rh nanoparticles which acts as a co-catalyst that doped on tungsten trioxide ( $\text{WO}_3$ )/ $\text{TiO}_2$  nanotube have better photocatalytic activity under UV light and visible light. Coupling of  $\text{WO}_3$  with  $\text{TiO}_2$  can be classified as type (3) semiconductor heterojunction structure which can form an artificial solid-state Z-scheme photocatalytic system. Thus, the charge carrier are able to pass through the energy barrier which prevent the recombination of electron-hole pairs by transferring photogenerated electron from CB of  $\text{WO}_3$  to VB of  $\text{TiO}_2$  and hole transfer from VB of  $\text{TiO}_2$  to CB of  $\text{WO}_3$  (Gao, *et al.*,2017). Z-scheme system is an improvement for type (3) semiconductor heterojunction structure where remaining electron and holes that interrupted at interface will end up in more negative CB and more positive VB between two connected photocatalysts (Zhang and Jaroniec, 2018). Therefore, Z-scheme photocatalytic system has various advantages such as separated charge carrier exhibit higher redox ability, high spatial charge separation efficiency and enhancement of light absorption for two coupling photocatalysts with narrower  $E_g$  (Q.Xu, *et al.*,2018). As a

result, the doping of Rh nanoparticles on  $\text{WO}_3/\text{TiO}_2$  can enhanced the generation of  $\text{H}_2$  4 times higher as compare to  $\text{WO}_3/\text{TiO}_2$  (Camposeco, *et al.*,2018).

#### 2.6.4 Titanium-Based Photocatalysts

Titania ( $\text{TiO}_2$ ) semiconductor is a well-known heterogeneous photocatalyst because it is inexpensive, non-toxic, stable light absorption and charge transport properties, supporter or dopant for other semiconductor (Singh, Mahalingam and Singh, 2013). However,  $\text{TiO}_2$  has wide band gap energy of 3.2 eV and can only be excited by UV light with wavelength less than 387 nm (H.Li, *et al.*,2018). Referring to the study by Bagheri, *et al.* (2015), there are three commonly known polymorphs of  $\text{TiO}_2$  that occurring naturally such as anatase, rutile and brookite and their crystal structure are shown in Figure 2.9. Rutile is stable phase while anatase and brookite is metastable phase which able to transform irreversibly to rutile phase during heating.

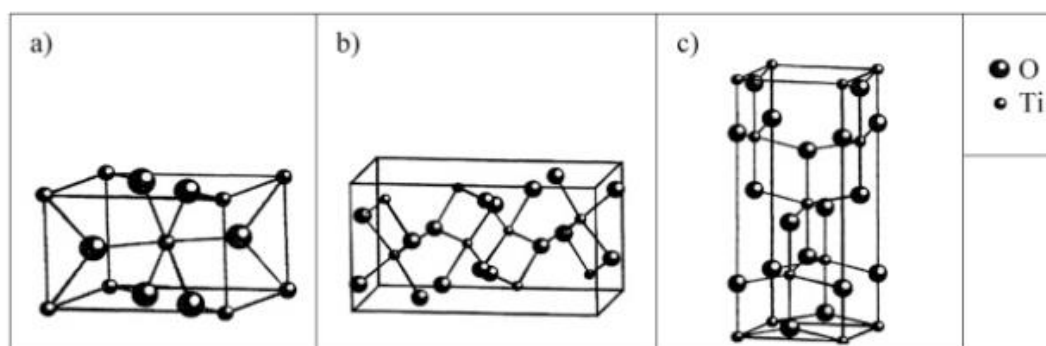


Figure 2.9: Crystal Structure of  $\text{TiO}_2$  for Rutile (a), Brookite (b) and Anatase (c) (Bagheri, *et al.*,2015)

Among various polymorphs of  $\text{TiO}_2$ , Evonik-Degussa P25 which is a mixture of anatase and rutile phase has better photocatalytic performance as compare for pure anatase and rutile (Clarizia, *et al.*,2017). This phenomenon is known as phase junctions which is the physical contacts between two different polymorphs of same materials. Phase junctions in  $\text{TiO}_2$  will allow the transport of charge carrier from one polymorphs to another which reduce the electron-hole recombination effect (Puga, 2016). However, only small part of solar energy can be utilized by  $\text{TiO}_2$  and most of the light energy is wasted. Therefore, Fang, Xing and Zhang (2017) found that modification of  $\text{TiO}_2$  by non-metal or metal doping, noble metal deposition and carbon-based composite can

narrowed the  $E_g$  of  $\text{TiO}_2$ , increased the light absorption spectrum and modified the electron density to prevent charge carrier recombination.

In a study by Chang and Cho (2016), Ag nanoparticles which act as a role of electron receivers doped on  $\text{TiO}_2$  can wider the visible light absorption region. Figure 2.10 presents separation of electron-hole pair over Ag/ $\text{TiO}_2$ . The presence of Ag doped on  $\text{TiO}_2$  can greatly improve the photocatalytic performance due to formation of Ag 4d orbital. The isolated energy level of Ag 4d formed in energy band gap of  $\text{TiO}_2$  can lower the  $E_g$  of  $\text{TiO}_2$  (Ouyang and Ye, 2011). Under the visible light irradiation, the photoinduced electrons are excited from Ag 4d to CB of  $\text{TiO}_2$  for reduction of oxygen to form  $\cdot\text{O}_2^-$ . On the other hand, the photogenerated holes that remain on the isolated energy level responsible for oxidation of  $\text{H}_2\text{O}$  to produce  $\cdot\text{OH}$ . Both  $\cdot\text{O}_2^-$  and  $\cdot\text{OH}$  radical species can be used to degrade the contaminants. The photoexcited electron will be transferred from CB of  $\text{TiO}_2$  to Ag nanoparticles due to more positive  $E_F$  of Ag than CB of  $\text{TiO}_2$ . The electron distribution between visible light irradiated  $\text{TiO}_2$  and Ag nanoparticles can result in equilibration of fermi level until the level close to the CB edge of  $\text{TiO}_2$ . As a result,  $E_g$  is reduced when Ag nanoparticles doped on  $\text{TiO}_2$ .

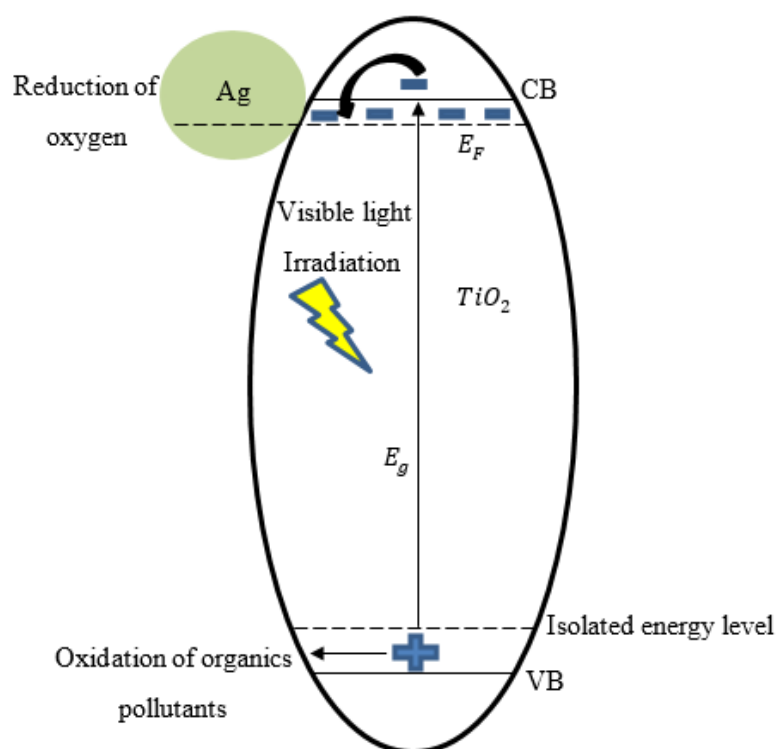


Figure 2.10: Schematic Diagram for Photocatalytic Mechanism of Ag doped  $\text{TiO}_2$  Photocatalysts (Chang and Cho, 2016)

Reddy, *et al.* (2016) found that doping of TiO<sub>2</sub> on polyaniline (PANI) lead to the formation of hybrid photocatalyst with enhanced photocatalytic activity. PANI is one type of conducting polymers which is environmentally friendly, high conductivity and easy to synthesis (Saranya, Rameez and Subramania, 2015). The photocatalytic performance was tested on photodegradation of RhB, MB and phenol under UV light irradiation. Table 2.5 shows the comparison of photocatalytic activity between pure TiO<sub>2</sub> nanoparticles and TiO<sub>2</sub>/PANI photocatalyst after three photocatalytic cycles with each cycle lasts for 200 minutes.

Table 2.5: Photodegradation Rate Between Pure TiO<sub>2</sub> Nanoparticles and TiO<sub>2</sub>/PANI Nanocomposite Photocatalyst

<b>Pure <i>TiO</i><sub>2</sub> Nanoparticles Under UV Light</b>	<b>Organic Pollutants</b>	<b><i>TiO</i><sub>2</sub>/<i>PANI</i> Nanocomposite Photocatalyst Under UV Light</b>	<b>References</b>
<b>34%</b>	RhB	73%	(Reddy, <i>et al.</i> ,2016)
<b>28%</b>	Phenol	51%	
<b>24%</b>	MB	67%	

Based on the result in Table 2.5, TiO<sub>2</sub>/PANI nanocomposite photocatalyst exhibit higher photocatalytic activity than pure *TiO*<sub>2</sub> nanoparticles even though after recycles in the presence of UV irradiation.

### 2.6.5 Zinc-Based Photocatalysts

Zinc oxide (ZnO) is a wurtzite crystal structure and white to yellowish-white crystalline powder that nearly soluble in water (Dimapilis, *et al.*,2018). It is widely used as heterogeneous photocatalyst due to the physiochemical properties of ZnO which promote antibacterial activity, antifouling properties (Al-Fori, *et al.*,2014). The physiochemical properties of ZnO include stability under photochemical corrosion and can absorbs over a larger region of UV spectrum compare to TiO<sub>2</sub> (Nazarkovsky, *et al.*,2017). Besides, the production cost of ZnO nanoparticles is 1/4 of the cost of TiO<sub>2</sub> and Al<sub>2</sub>O<sub>3</sub> based on China market (Liang, *et al.*,2012). However, ZnO has slightly higher E<sub>g</sub> compare to TiO<sub>2</sub> which is 3.37eV with large excitation binding energy (60 meV) (Choi, Kang and Oh, 2012). The wider E<sub>g</sub> of ZnO will limit the visible light absorption which result in fast recombination of photoinduced charges carrier and

reduced photocatalytic quantum efficiency (Gomez-Solís, *et al.*,2015). Therefore, charge carrier recombination effect can be impeded by metal or non-metal doping on ZnO.

Y.Liu, *et al.* (2015) found that Z-scheme metal free polymeric semiconductor material g-C<sub>3</sub>N<sub>4</sub> doped on modified oxygen vacancy rich ZnO (V<sub>o</sub>-ZnO) hybrid photocatalyst can enhanced the visible light photocatalytic performance. Oxygen vacancies play an important role as trap centre to improve the photocatalytic performance (Gomez-Solís, *et al.*,2015). High concentration of oxygen vacancies can result in narrowing E<sub>g</sub> and improve the visible light absorption capability of ZnO (Wang, *et al.*,2012). As a result, E<sub>g</sub> of V<sub>o</sub>-ZnO are narrowed to 3.09eV which allow more production of photogenerated charge carrier responsible for photodegradation of pollutants. Figure 2.11 illustrates the photocatalytic mechanism for g-C<sub>3</sub>N<sub>4</sub> doped V<sub>o</sub>-ZnO.

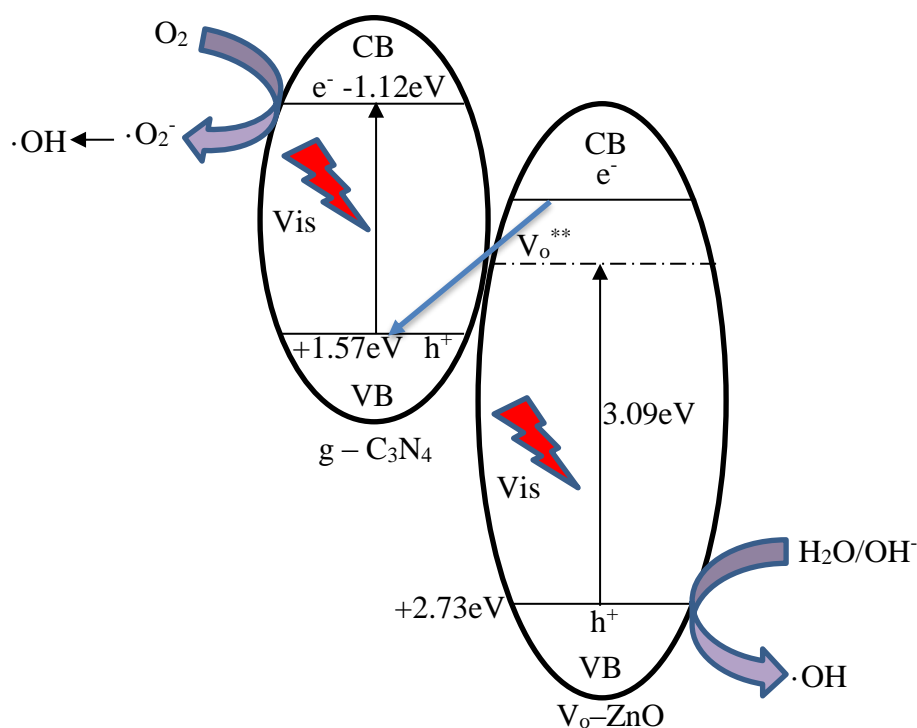


Figure 2.11: Schematic Diagram Illustration of Photocatalytic Reaction Mechanism of g-C<sub>3</sub>N<sub>4</sub>/V<sub>o</sub>-ZnO Hybrid Photocatalyst Under Visible Light Irradiation (Y.Liu, *et al.*,2015)

Based on Figure 2.11, the CB potential of g-C<sub>3</sub>N<sub>4</sub> is more negative than oxidative potential, E<sup>0</sup> (O<sub>2</sub>/·O<sub>2</sub><sup>-</sup> = -0.046 eV). Therefore, the stored photoinduced electron in CB of g-C<sub>3</sub>N<sub>4</sub> can reduce O<sub>2</sub> to yield ·O<sub>2</sub><sup>-</sup> and further react with H<sub>2</sub>O to

form  $\cdot\text{OH}$ . On the other hand, the VB edge potential of  $\text{g-C}_3\text{N}_4$  is more negative than  $E^0$  ( $\text{OH}^-/\text{H}_2\text{O} = +1.99$  eV). Thus, the photogenerated holes in VB of  $\text{g-C}_3\text{N}_4$  cannot react with  $\text{H}_2\text{O}/\text{OH}^-$  to form  $\cdot\text{OH}$ . Under the irradiation of visible light, both  $\text{g-C}_3\text{N}_4$  and  $\text{V}_0\text{-ZnO}$  are excited. Due to the Z-scheme system, the photogenerated electron from CB of  $\text{V}_0\text{-ZnO}$  are transferred to VB of  $\text{g-C}_3\text{N}_4$  resulting in recombination of charge carrier to form  $\text{H}_2\text{O}$ .  $\text{H}_2\text{O}$  generated will further be oxidized in VB of  $\text{V}_0\text{-ZnO}$  to increase the amount of  $\cdot\text{OH}$  produced. The generation of  $\cdot\text{OH}$  is responsible for degradation of contaminants.

### 2.6.6 Copper-Based Photocatalysts

Copper (Cu) based heterogeneous photocatalyst has been widely used due to abundantly available, good selectivity, simple process for semiconductor layer formation, low cost and acceptable photocatalytic (Saraswat, Rodene and Gupta, 2018; Tahir, et al., 2016). Copper oxide ( $\text{CuO}/\text{Cu}_2\text{O}$ ) are the popular p-type semiconductor used as photoelectrodes for degradation of pollutants due to narrower  $E_g$  (2.17eV) (Isherwood, 2017). They can act as photosensitizer with large  $E_g$  photocatalyst to increase the visible light absorption capability. This is because Cu nanoparticles can generate localized surface plasmon resonance (LSPR) under the visible light irradiation for specific wavelength (Zhao, *et al.*, 2016). LSPR is the interaction of light with Cu nanoparticles that are smaller than incident light wavelength to produces a collective oscillation of conduction band electrons. When incident electromagnetic field matches the oscillating electrons on the Cu surface, resonance oscillation is produced. This resonant oscillation will increase the absorption of visible light for specific wavelength (Unser, *et al.*, 2015). However, smaller  $E_g$  will lead to rapid recombination of charge carrier which lower the photocatalytic performance. Therefore, doping and coping of Cu photocatalyst is used for slow down the charge carrier recombination effect, increase interfacial charge carrier transfer and increase the visible light absorption range by creating defect states in band gap (Delsouz Khaki, *et al.*, 2018). Recombination effect is inhibited by both conduction band electron and valence band hole trapped in defect sites.

Referring to the study by Behzadifard, Shariatinia and Jourshabani (2018), hybrid photocatalyst of  $\text{CuO}$  (10 wt%) doped on rare earth perovskite type oxides samarium orthoferrite ( $\text{SmFeO}_3$ ) exhibit better photocatalytic performance for

photodegradation of RhB under visible light irradiation. The semiconductor heterojunction structure for this type of hybrid photocatalyst is type 1. Figure 2.12 presents the photodegradation mechanism of CuO/SmFeO<sub>3</sub> hybrid photocatalyst under the visible light irradiation.

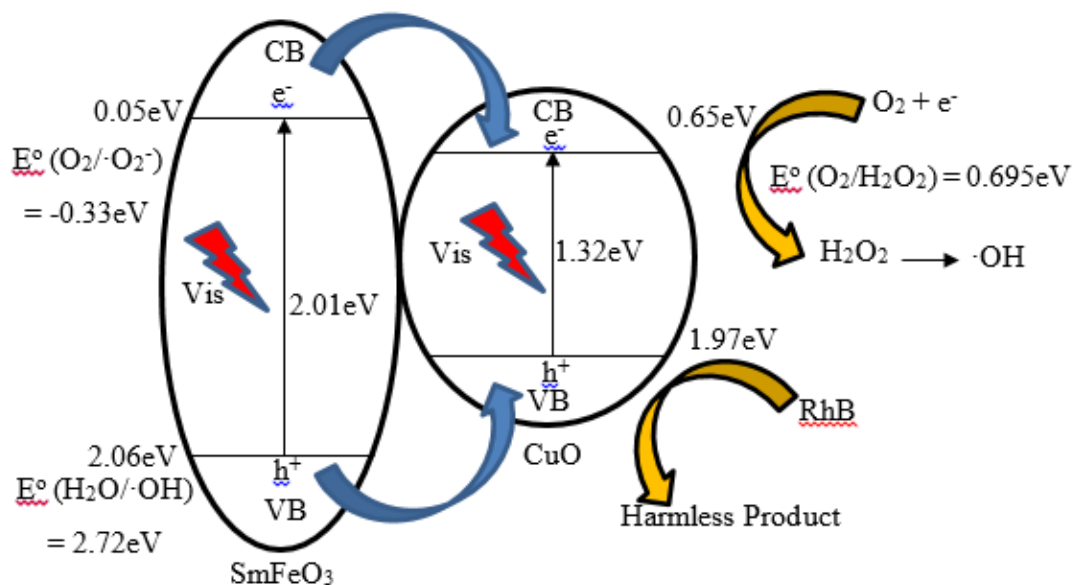


Figure 2.12: Photodegradation Mechanism of CuO/SmFeO<sub>3</sub> nanocomposite for RhB Dye Under Visible Light Irradiation (Behzadifard, Shariatinia and Jourshabani, 2018)

Based on the Figure 2.12, electron-hole pairs are generated on CuO and SmFeO<sub>3</sub> under the irradiation of visible light. The CB edge potential of SmFeO<sub>3</sub> is more negative than CuO, so the photogenerated electron will be transferred to CB of CuO. On the other hand, photoinduced holes will also be transferred to CuO due to more positive VB of SmFeO<sub>3</sub> than CuO. As a result, the charge carrier recombination effect will be retarded. The E<sup>o</sup> of O<sub>2</sub>/·O<sub>2</sub><sup>-</sup> is more negative than CB edge potential of SmFeO<sub>3</sub>, so adsorbed oxygen molecule on the surface of SmFeO<sub>3</sub> will not be reduced to ·O<sub>2</sub><sup>-</sup>. This effect also same for VB of SmFeO<sub>3</sub> which cannot produced ·OH. Furthermore, E<sup>o</sup> of O<sub>2</sub>/H<sub>2</sub>O<sub>2</sub> is more positive than CB edge potential of CuO. Thus, O<sub>2</sub> adsorbed on the surface of CuO will undergo reduction to produce H<sub>2</sub>O<sub>2</sub> which further react to form ·OH. The photogenerated holes on VB of CuO will react directly with adsorbed RhB dye to produce harmless product. The generation of ·OH can ensure complete abatement of pollutants compare to direct react (Rajamanickam and Shanthi, 2016).

### 2.6.7 Nitrogen-Based Photocatalysts

Nitrogen (N) is classified as p-block non-metals that usually doped on TiO<sub>2</sub> to narrow the E<sub>g</sub>, retard the recombination of electron-hole pairs, exhibits broad visible light absorption region and extend the phase transformation temperature for TiO<sub>2</sub> from anatase to rutile (Nasirian and Mehrvar, 2018; Periyat et al., 2009). Thus, improvement of photocatalytic performance under visible light irradiation. This is because nitrogen that introduced into TiO<sub>2</sub> has slightly higher energy level than oxygen which create mid-gap energy state. Mid-gap energy level enables the excitation of electron from mid-gap energy level to CB upon visible light absorption. Therefore, the E<sub>g</sub> is narrower from 3.2eV (undoped TiO<sub>2</sub>) to 2.5eV (N doped TiO<sub>2</sub>) (Ansari, *et al.*, 2016).

Zhang, Yang and Park (2018) found that N doped TiO<sub>2</sub> supported on RGO which fabricated by sol-gel and hydrothermal process exhibit better photodegradation of organic dye under visible light irradiation. Figure 2.13 illustrates the photodegradation mechanism of N doped TiO<sub>2</sub> supported RGO under the presence of visible light. The N 2p situated above the VB which form narrower E<sub>g</sub> that extends the absorption of N/TiO<sub>2</sub> into visible light region. Under the irradiation of visible light, electron from N 2p is excited to CB leaving photogenerated hole in N 2p. The photogenerated electron transferred from N/TiO<sub>2</sub> to high electron mobility RGO. This means RGO can act as electron acceptor and cause separation of electron-hole (Vahidzadeh, Fatemi and Nouralishahi, 2018). The photogenerated electron react with adsorbed oxygen to form  $\cdot\text{O}_2^-$ . On the other hand, the photoinduced holes in N 2p will react with H<sub>2</sub>O to form  $\cdot\text{OH}$ . Both  $\cdot\text{O}_2^-$  and  $\cdot\text{OH}$  involve in photodegradation of organic pollutants.

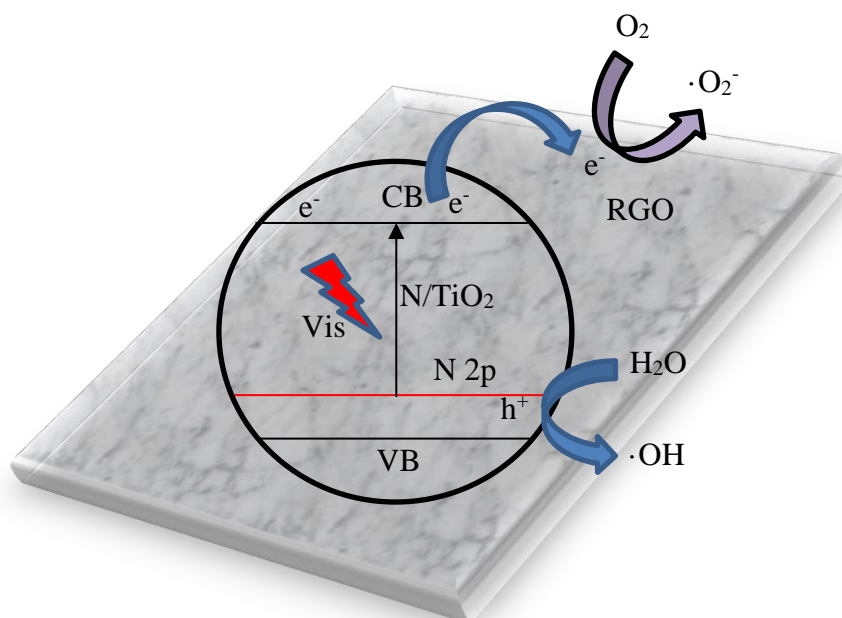


Figure 2.13: Schematic Diagram of Photodegradation Mechanism For N/TiO<sub>2</sub>/RGO Nanocomposite (Zhang, Yang and Park, 2018)

### 2.6.8 Graphene-Based Photocatalysts

Graphene is a one atom thick planar sheet of 2D sheet of  $sp^2$  bonded carbon atoms densely packed in honeycomb crystal lattice (Choi, *et al.*, 2010). It can be stacked to form 3D graphite, rolled to form 1D nanotubes and wrapped to form 0D fullerene (graphene quantum dots) which provide possibility to construct various heterojunctions structure for hybrid photocatalyst (Allen, Tung and Kaner, 2010; Li *et al.*, 2018). Graphene is a zero  $E_g$  semiconductor that has higher specific surface area, good interfacial contact with adsorbents and good electric electron-hole pairs mobility (Choi, *et al.*, 2010). Therefore, it would improve the photocatalytic performance and inhibit the recombination of charge carrier. Putri, *et al.* (2015) found that the zero  $E_g$  is due to antibonding  $\pi^*$  orbitals (CB) and bonding  $\pi$  orbitals (VB) degenerate and touch at Brillouin zone corners. By chemical doping, bandgap will form between  $\pi$  and  $\pi^*$  which convert graphene into semiconductor and promote more active sites for pollutants adsorption. The higher the dopant concentration, bandgap is found to be wider and better electrical conductivity (Rani and Jindal, 2013). Graphene oxide (GO) can be formed by bonding of graphene sheets with oxygen containing chemical groups whereas chemical reduction of GO sheets by reducing agent such as glucose and hydrazine will form RGO (Pérez del Pino, *et al.*, 2018; Shahbazi, Payan and Fattahi,

2018). For GO, oxygen containing group will form covalent bonds with semiconductor which damage the original orbitals and cause separation of  $\pi$  and  $\pi^*$  orbital that create lower  $E_g$  (Yeh, *et al.*,2013).

Referring to the study by Han, *et al.* (2015), N doped graphene (NGR) can enhance the photocatalytic activity. The size of N atom is same as the carbon atom and N atom contains five valence electron which is available to form covalent bonds with carbon atom. Therefore, the  $E_g$  of NGR is less compare to undoped graphene due to formation of more covalent bond (Yeh, *et al.*,2013). Besides, each graphitic N atom will contribute extra electron to graphene  $\pi$  system (Usachov, *et al.*,2011). The electron donation will enhance the electronic conductivity so that photogenerated charge carrier transferred rapidly to the surface of another semiconductor to retard the electron-hole pairs recombination. Furthermore, NGR will allow more absorption of visible light due to presence of carbon and N atom that reduce the reflection of visible light. Liu, *et al.* (2016) found that N doped TiO<sub>2</sub> nanowire supported on N- doped graphene (N-TiO<sub>2</sub>/NG) which fabricated by facile hydrothermal method using urea as nitrogen source. The photocatalytic efficiency is tested by photodegradation of MB dye under visible light irradiation. Figure 2.14 illustrates the photodegradation mechanism for N-TiO<sub>2</sub>/NG. Under the irradiation of visible light, photoexcitation process occurs in both N-TiO<sub>2</sub> and NG. Excitation energy require for N-TiO<sub>2</sub> will be less due to present of N 2p which lower  $E_g$ . The photogenerated electron from more negative CB edge potential of N-TiO<sub>2</sub> will be transferred to less negative CB edge potential of NG. Meanwhile, the photoinduced hole will be transfer from more positive VB edge potential to less positive VB edge potential. As a result, photogenerated electron capture O<sub>2</sub> on the surface to form  $\cdot O_2^-$  while photoinduced hole oxidize H<sub>2</sub>O to produce  $\cdot OH$ .

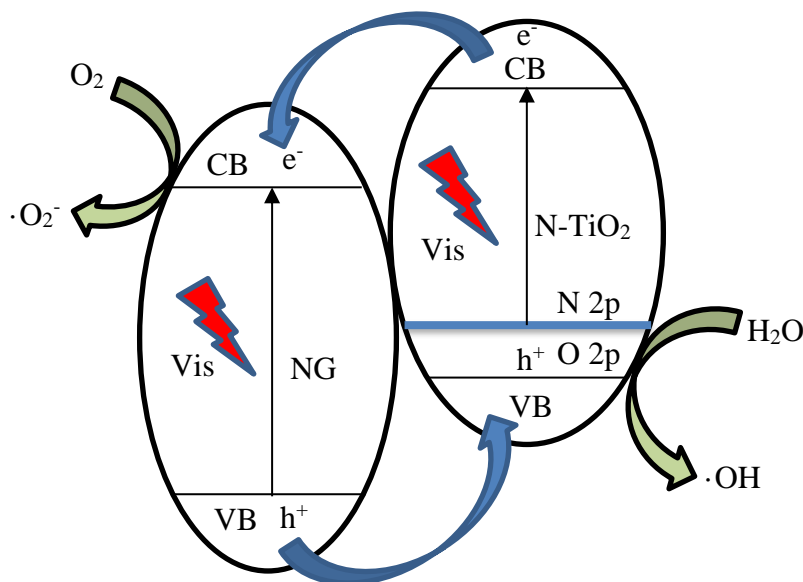


Figure 2.14: Schematic Diagram of Photodegradation Mechanism of N-TiO<sub>2</sub>/NG for MB Under Visible Light Irradiation (Liu, *et al.*,2016)

### 2.6.9 CQDs-Based Photocatalysts

Carbon quantum dots (CQDs) is carbon atom that form quasi-spherical shape normally with a high quantum yield, low toxicity and good stability (Lei, *et al.*,2016; Das, *et al.*,2018). CQDs are a new kind of 0D carbon nanoparticles with particle size of between 2 and 10 nm and with a predominant graphitic character ( $sp^2$  carbon) merged by  $sp^3$  type carbon inclusions (Shi Ying Lim, *et al.*,2014). Since CQDs particles size is extremely small and CQDs can exhibit up converted photoluminescence (UPCL) (Aghamali, *et al.*,2018). UCPL means wavelength emitted by CQDs upon light absorption is less than absorbed light wavelength. Thus, range of light wavelength that composite can absorb developed into visible region and near infrared red region. For an example, excitation wavelength range from 600 nm – 800 nm irradiate up – converted emissions located in the range of 375 - 550 nm (Hu, *et al.*,2018). CQDs fabrication methods usually involve oxidation which make the CQDs have O<sub>2</sub> containing functional group such as carboxyl, -COOH, carbonyl. -CO and hydroxyl, -OH. Figure 2.15 presents typical chemical structure of CQDs where it exists conjugated  $\pi$  structure.

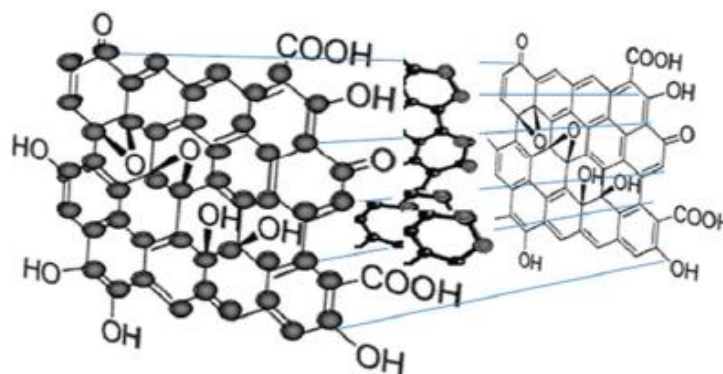


Figure 2.15: Chemical Structure of CQDs (Lim, Shen and Gao, 2015)

The surface functional groups depend on type of resources used to produce CQDs. Different sized of CQDs and different surface functional groups have different energy gaps and exhibit different photoluminescence properties (Cui, *et al.*,2017). Han, *et al.* (2014) found that introduction of CQDs to another semiconductor can improve the photocatalytic activity under visible light irradiation due to highly electron-accepting or electron-donating capability. However, CQDs can exhibit excellent electron donating and accepting because it consists of conjugated  $\pi$  structure (Di, *et al.*,2015). There are two approaches to synthesize quantum sized CQDs which are “top-down” and “bottom-up” methods as shown in Figure 2.16 (daSilva Souza, *et al.*,2018). Top down strategies involve physical or chemical breakage of carbon rich materials such as graphite, active carbon and carbon nanotube. On the other hand, bottom up strategies involve polycondensation of biocompatible carbon source molecules such as carbohydrates organic acid and natural resources (Choi, *et al.*,2017).

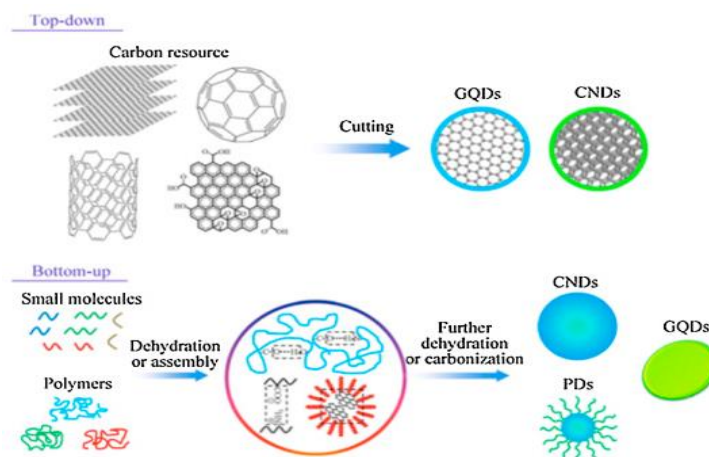


Figure 2.16: Schematic Chemical Structure of CQDs Formed From Two Different Approaches (Namdari, Negahdari and Eatemadi, 2017)

The benefit of production CQDs from natural renewable source such as chitosan gel, lysine, watermelon peel and pomelo peel are cost effective and eco-friendly (Das, Bandyopadhyay and Pramanik, 2018). Top down methods include arch discharge, laser ablation and electrochemical oxidation while bottom up methods include pyrolysis, hydrothermal carbonization and microwave assisted methods (Das, Bandyopadhyay and Pramanik, 2018). Among top down and bottom up methods, microwave assisted heating (MAH) identified high efficiency to synthesize CDs due to time saving, non-hazardous, smaller nanometres size and producing high quantum yield (QY) (Borse, *et al.*,2017).

Ke, Garg and Ling (2014) found that nitrogen doped CDs can efficiently induce charge delocalization, lower work function of carbon and enhance the photoluminescence properties due to size of N atom similar to carbon atom which is available to form covalent bonds with carbon atom. Thus, large conjugated carbon structure of CDs was broken and induced the surface defects of CDs which lead to better electronic conductivity properties to accelerate electron transport as well as increase specific surface area for adsorption of pollutants (Li, *et al.*,2017). Besides, heteroatom sulphur, S doping also have the same function as the N which can significantly improve electron concentration of CQD and photo excitation performance (Zhang *et al.*,2018). Lysine is one of the naturally abundant amino acids present in high protein food such as egg, meat and soybean which contains nitrogen atom (Choi *et al.*,2017). Based on M.Li, *et al.* (2018) study, N, S co-doped CQDs (N,

S-CQDs) supported on TiO<sub>2</sub> (P25) has enhance photocatalytic performance on photoreduction of CO<sub>2</sub> due to 2 important role of N, S-CQDs. N, S-CQDs can act as both photo-sensitizers and electron reservoirs in this photocatalyst composite system. Firstly, under visible light irradiation, N, S-CQDs with high N and S doping levels can suppress non-radiative quenching by reducing inner layer energy traps between sp<sup>2</sup>-domains, leading to high photoluminescence quantum yield. Thus, highly advantageous for the sensitization of TiO<sub>2</sub> since more photo-generated electrons will be transferred from CB of N, S-CQDs to TiO<sub>2</sub> to drive photodegradation reaction due to N doping lower the work function of CQDs (Shi, *et al.*,2017). Secondly, N, S-CQDs can absorb and convert broad range of visible light region which extended into near infrared region (Huo, *et al.*,2017). Therefore, converted light with shorter wavelength could excite TiO<sub>2</sub> to produce more charge carrier responsible for photodegradation. Lastly, the charge separation in TiO<sub>2</sub> leads to photogenerated electron transfer to N, S-CQDs which act as the active sites for photodegradation.

## **2.7 N, S Co-Doped CQDs/TiO<sub>2</sub> Deposited on PSF UF Membrane**

In summary, N, S-CQDs/TiO<sub>2</sub> entrapped on PSF membrane was fabricated in this research to photodegrade DCF pharmaceutical pollutant under the UV-Vis light irradiation. PSF membrane was used as UF membrane due to low cost, good thermal stability, superior film forming ability and strong acid and alkaline resistance. However, PSF has prone to fouling due to its hydrophobic properties and bad UV resistance (Wang, *et al.*,2017). In other words, free radicals generation will deteriorate PSF membrane properties and cause a reduction in membrane molar mass. Thus, chemical cleaning and back-flushing are required. This will shorten membrane lifespan and lead to higher operating cost. Referring to the study by Yang, *et al.* (2007), blending the PSF membrane with nano-TiO<sub>2</sub> can have super hydrophilicity, UV resistance and able to degrade bacteria. Based on Figure 2.15, CQDs are terminated by oxygen moieties on their surface such as carboxylate and hydroxyl group which can improve the hydrophilicity. During membrane casting, hydrophilic CQD/TiO<sub>2</sub> nanoparticles migrate to water/PSF membrane interface. This reduce interface energy and increase hydrophilic particles on PSF membrane surface which reduce membrane fouling. Hydrophilicity is an important parameter which can affect the permeate flux and antifouling properties of membrane. It can be determined by contact angle with

water. The contact angle of PSF is  $84.7^\circ$  and it will decrease which depends on the amount of  $\text{TiO}_2$  (wt %) added. Currently, the main problem is  $\text{TiO}_2$  has a wide  $E_g$  which causes radiative recombination to occur. Thus,  $\text{TiO}_2$  photocatalytic membrane can be improved by doping with CQDs. Although CQDs doping does not have a significant effect on  $E_g$ , it can increase the quantum photoluminescence yield by extending the absorption wavelength to the infrared region. Besides, CQDs can exhibit both electron transfer and electron reservoir properties due to its conjugated  $\pi$  structure. Hence, it can prevent the charge carrier recombination effect. However, the higher work function of CQDs still remains a major challenge where a large amount of energy is required to remove photogenerated electrons from the CB of CQDs and transfer them to the CB of  $\text{TiO}_2$ . Therefore, nitrogen and sulphur codoped CQDs have been introduced to lower the work function due to the broken down of conjugated  $\pi$  structure by the formation of covalent bonds between nitrogen and carbon atoms. A low work function indicates that more photogenerated electrons can be stored and transferred rapidly.

## CHAPTER 3

### METHODOLOGY

#### 3.1 General Preview

In this chapter, the focus on fabrication of photocatalytic membrane which can exhibit high photoluminescence behaviour and excellent membrane permeability for removal of DCF pharmaceutical waste. Fabrication process can be done by first preparing hybrid photocatalyst which was N, S co-doped CQDs supported on TiO<sub>2</sub> followed by incorporation with PSF type membrane using in-situ phase inversion.

#### 3.2 Materials and Chemicals

Materials and chemical reagents that had been used in this experiment for preparing N, S-CQDs/TiO<sub>2</sub> on PSF membrane are listed in Table 3.1. Model pollutant used was DCF at concentration of 10 ppm.

Table 3.1: Material and Chemical Used in Experiment and Their Specifications

<b>Materials / Chemicals</b>	<b>Purity</b>	<b>Brand</b>	<b>Purpose</b>
<b>Egg Yolk</b>	-	-	Source of NCQDs
<b>Sulphuric Acid, H<sub>2</sub>SO<sub>4</sub></b>	95-98 %	R&M	Decompose egg yolk to get intermediate product Source of sulphur heteroatom doping
<b>Nitric acid, HNO<sub>3</sub></b>	65 %	Sigma-Aldrich	Decompose egg yolk and formation of TiO <sub>2</sub>
<b>Deionized Water</b>	100 %	-	To ensure absent of ion in the sample
<b>Titanium Dioxide (TiO<sub>2</sub>) Powder with Particle Size of 21 nm</b>	100 %	Sigma-Aldrich	Source of hybrid photocatalyst

Table 3.1: Continued

<b>Materials / Chemicals</b>	<b>Purity</b>	<b>Brand</b>	<b>Purpose</b>
<b>Polysulfone (PSF) with Nominal Size of 2 mm</b>	100 %	Sigma Aldrich	Photocatalytic membrane casting solution
<b>Polyvinylpyrrolidone (PVP) Solution</b>	100 %	Sigma Aldrich	Photocatalytic membrane casting solution
<b>N-methyl-2-pyrrolidone (NMP) Solution</b>	99.5 %	Sigma Aldrich	Photocatalytic membrane casting solution
<b>Diclofenac (DCF) Powder</b>	100 %	Alfa Aesar	Model pollutant

### 3.3 Instruments and Equipments

The instruments and equipment used for this experiment are tabulated in Table 3.2 with their model and function.

Table 3.2: Model and Function of Instruments and Equipments

<b>Instrument/Equipment</b>	<b>Brand/Model</b>	<b>Function</b>
<b>Vacuum Oven</b>	-	To dry boiled egg yolk at 80°C
<b>N<sub>2</sub> Atmosphere Tube Furnace</b>	Lenton, UK / LTF 12/100/940/3216CC	To calcine N doped precursor at 300 °C
<b>Syringe</b>	Sigma Aldrich	To withdraw DCF solution every 20 minutes for determination of concentration
<b>Visible Lamp with 80 W (&gt; 400 nm)</b>	-	To provide visible light irradiation
<b>UV Lamp with 80 W (&lt; 380 nm)</b>	-	To provide UV light irradiation

Table 3.2: Continued

<b>Instrument/Equipment</b>	<b>Brand/Model</b>	<b>Function</b>
<b>Fourier Transform Infrared Spectroscopy (FTIR)</b>	Nicolet/IS10	To analyse chemical functional group based on absorption of infrared radiation
<b>X-ray Diffraction (XRD)</b>	Shidmazu/XRD-6000	To perform phase identification of crystalline structure
<b>Scanning Electron Microscope (SEM) Equipped Energy Dispersive X-ray (EDX)</b>	Hitachi/S-3400N	To check surface morphology and chemical composition
<b>Ultraviolet – visible Spectrophotometer (UV-Vis)</b>	Cary 100	To determine maximum absorption peak wavelength To measure initial and final concentration of DCF
<b>Clean Glass</b>	-	To coated with membrane casting solution
<b>Magnetic Stirrer with Hot Plate</b>	IKA	To heat up and homogeneously stir solution
<b>Film Applicator</b>	-	To spread casting solution onto glass
<b>Coagulant Bath</b>	-	To fill N, S-CQDs/TiO <sub>2</sub> photocatalyst solution and coagulate PSF membrane

### 3.4 Overall Research Flowchart

The summarized of the overall research flowchart is shown in the Figure 3.1.

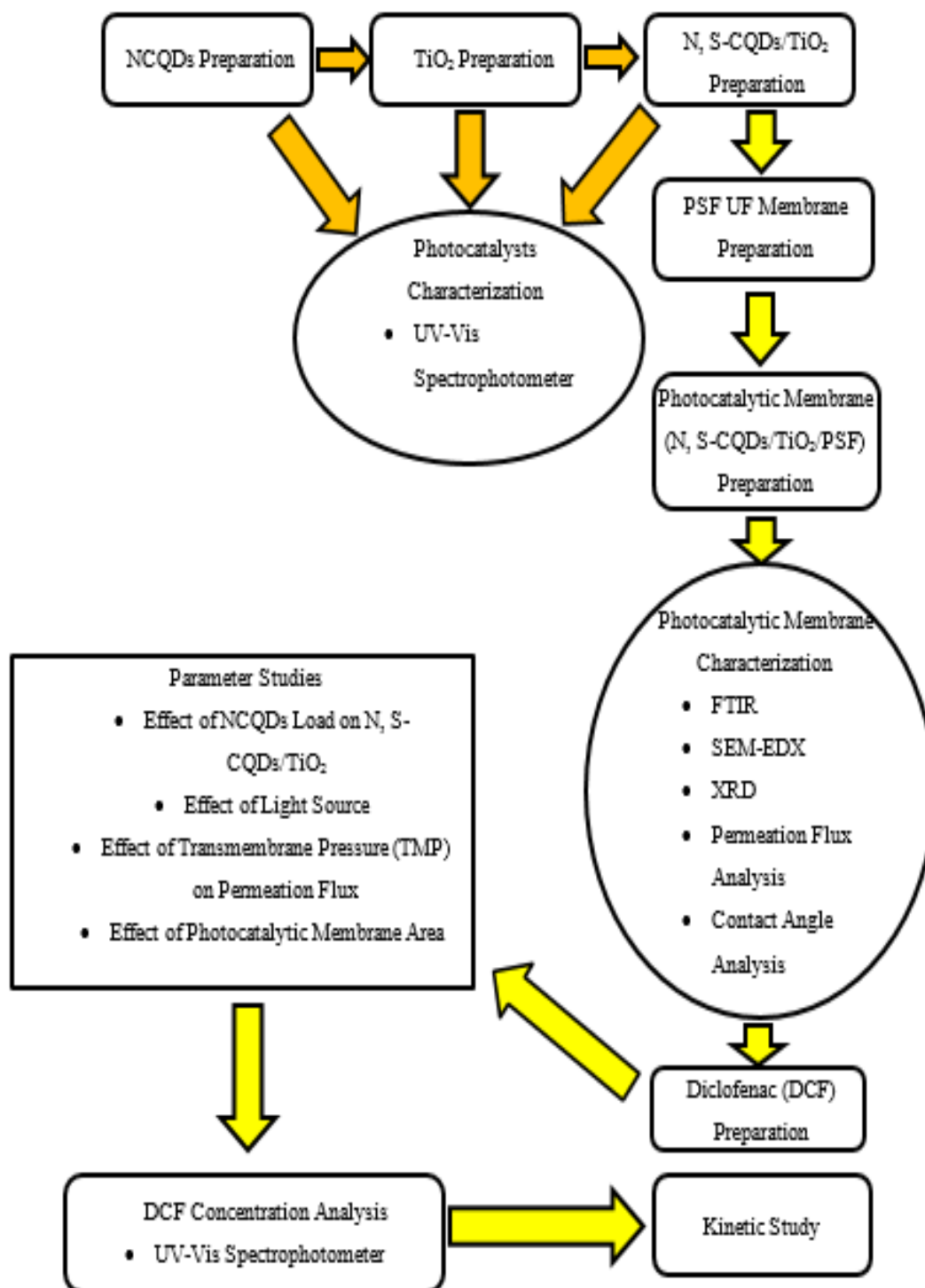


Figure 3.1: Overall Flow Diagram of the Research

### 3.5 Experiment Procedures for Preparation of N, S-CQDs/TiO<sub>2</sub> Photocatalysts Solution

Firstly, a normal chicken egg bought from supermarket was boiled and the before egg yolk was separated from egg white. The purpose of using egg yolk instead of egg white was because it has high amino acid content which contain N atoms. Then, the boiled egg yolk was put into vacuum oven and dried for 80°C. After that, the dried and mashed egg yolk was put into tube furnace and heated up to 300°C under N<sub>2</sub> atmosphere for 3 hours at a heating rate of 5 °C/min to produce black and sticky N doped CQDs powder. Next, the sample was cooled to room temperature for one day and a mixture of H<sub>2</sub>SO<sub>4</sub> and HNO<sub>3</sub> were added to certain loading of NCQDs powder at 120 °C for 6 hours to get N, S-CQDs/TiO<sub>2</sub>. The ratio of concentrated acid added was 3:1 based on volume/volume percent (v/v %) which was 150 ml of H<sub>2</sub>SO<sub>4</sub> and 50 ml of HNO<sub>3</sub>. As shown in Figure 3.2, this process was conducted inside the fume cupboard and reflux condition was used because it will emit yellowish brown acidic gas which indicated the formation of N, S-CQDs photocatalyst (Martins et al.,2016).



Figure 3.2: Reflux Process to Produce Yellowish brown N, S-CQDs Photocatalyst Solution

Later, 0.2g of TiO<sub>2</sub> powder was added to the resulting N, S-CQDs solution and stir for 2 hours for doping of N, S-CQDs nanoparticles on TiO<sub>2</sub>. Next, 400 ml of deionized water was mixed with N, S-CQDs/TiO<sub>2</sub> photocatalyst solution and further stirred for 30 minutes.

### **3.6 Experiment Procedures for Preparation of PSF UF Membrane**

Membrane casting solution need PSF, polyvinylpyrrolidone (PVP) and N-methyl-2-pyrrolidone (NMP). NMP was the solvent for casting solution while PVP was used as an additive to enhance the hydrophilicity of PSF membrane to increase the membrane porosity (Barzin, *et al.*,2004). Firstly, PSF was filled in a 250 ml beaker and dried in an oven at 65°C overnight to remove the moisture content. To prepare 50g of casting solution, 17 % PSF and 1.0 % of PVP with respect to weight of 17 % PSF were dissolved in 83 % NMP at 60 °C. The solution was covered with a thin film to avoid entered of moisture from environment and stirred using magnetic stirrer until it became transparent and homogeneous as shown in Figure 3.3 (a). Then, let the resulting homogeneous membrane casting solution cooled down to room temperature for overnight to remove bubbles and degassed prior to use.

### **3.7 Experiment Procedures for Fabrication of N, S-CQDs/TiO<sub>2</sub> Photocatalysts Entrapped on PSF UF Membrane**

Referring to the study by Zhang, et al. (2017), in-situ phase inversion method was used to prepare MMM to improve anti-fouling properties of membrane. For this method, yellowish N, S-CQDs/TiO<sub>2</sub> photocatalyst solution as coagulant bath which allowing the formation of photocatalytic membrane and immobilization of N, S-CQDs/TiO<sub>2</sub> nanoparticles onto membrane surface simultaneously. For membrane casting section, the prepared membrane casting solution was spread onto a dry and clean glass plate using a casting blade adjusted to 200 µm thick as shown in Figure 3.3 (b). After that, the casted glass plate was smoothly immersed into the coagulant bath which filled with as prepared N, S-CQDs/TiO<sub>2</sub> photocatalyst solution. The N, S-CQDs/TiO<sub>2</sub> photocatalysts entrapped on PSF UF membrane was formed after complete coagulation as shown in Figure 3.3 (c). Lastly, the resulting photocatalytic membrane was immersed inside the photocatalyst solution coagulant bath and covered with

aluminium foil for one day prior to use. This is to ensure complete entrapment of photocatalysts and avoid the photocatalytic membrane exposed to light irradiation.

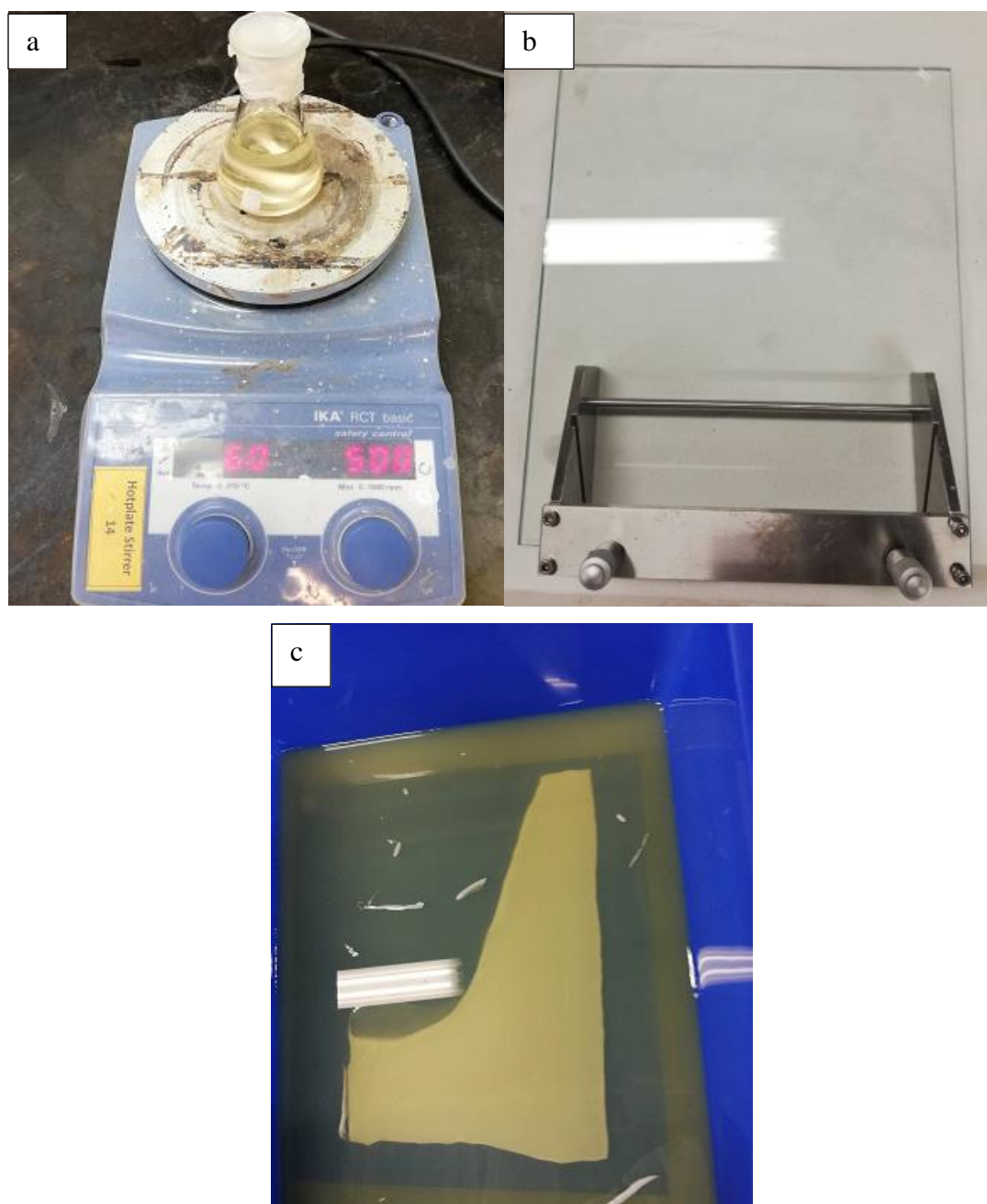


Figure 3.3 Fabrication Process of Photocatalytic Membrane; (a) Preparation of Membrane Casting Solution (b) Membrane Casting Using the Casting Blade (c) In-situ Phase Inversion Process in Water Bath

### 3.8 Characterization of Photocatalyst Solution and Photocatalytic Membrane

#### 3.8.1 Characterization of Photocatalyst Solution

Photocatalyst characterization is an essential step that must be carried out in order to understand the nature of photocatalyst. By knowing the characteristics of photocatalyst, their performance can be explained. In this research, photocatalyst had been characterized by UV-vis spectrophotometer.

##### 3.8.1.1 Ultraviolet-Visible (UV-Vis) Spectrophotometer

The strong absorption peak wavelength,  $\lambda$  for TiO<sub>2</sub> and different loading of NCQDs on N, S-CQDs/TiO<sub>2</sub> was obtained by using UV-Vis spectrophotometer. By knowing the specific  $\lambda$  for each of the photocatalysts, photodegradation efficiency for each type of photocatalyst was roughly estimated from the shift of light absorption range after N, S-CQDs doping. Besides, this allowed the comparison of photocatalyst  $E_g$  before doping and after doping. The  $E_g$  can be calculated from band gap energy formula as shown in Equation 3.1.

$$E_g = \frac{hc}{\lambda} = \frac{1.2408 \times 10^{-6}}{\lambda} \quad (3.1)$$

where

$E_g$  = band gap energy (eV)

$h$  = planck's constant ( $4.1359 \times 10^{-15}$  Js)

$c$  = light velocity ( $3 \times 10^8$  m/s)

$\lambda$  = absorption threshold wavelength (m)

From Equation 3.1,  $E_g$  is inversely proportional to  $\lambda$ . This indicates the higher the  $\lambda$ , the smaller the  $E_g$ . Small  $E_g$  allows more electron to excite from highest energy occupied molecular orbital (HOMO) to lowest energy unoccupied molecular orbital (LUMO) through the absorption of light.

### **3.8.2 Characterization of Photocatalytic Membrane**

Photocatalytic membrane characterization is an important step that must be carried out to check the dispersibility of photocatalyst on the UF membrane. It allowed an insight to determine the composition, chemical structure, particle size, mean pore size of membrane, particles structure, pore structure and chemical properties. In this research, photocatalytic membrane was characterized by FTIR, XRD and SEM-EDX.

#### **3.8.2.1 Fourier Transform Infrared (FTIR) Spectroscopy**

FTIR was non-destructive analysis that could be performed on Perkin Elmer spectrophotometer equipped with a 45 ° diamond/ ZnSe universal attenuated total reflectance sample holder. It could identify organic and inorganic catalyst both as solid or liquid phase. Structural features of TiO<sub>2</sub> and N, S-CQDs/TiO<sub>2</sub> PSF UF membrane could be examined by FTIR in the range of 4000-500 cm<sup>-1</sup> on a pressed KBr tablet. Principle of FTIR to analyse chemical functional group presence in functional group was detecting the vibrations that characterize chemical bonds based on the absorption of infrared radiation. FTIR spectrum is a graph of infrared light absorbance or transmittance as a function of frequency or wavenumber, cm<sup>-1</sup>. It depends on amount of light absorbed by the photocatalyst as transmittance is smaller when more light was absorbed. In this analysis, it was expected that all pure PSF signature peaks were visible in the composite membrane which can indicated the entrapment of N, S-CQDs/TiO<sub>2</sub> nanoparticles did not change the PSF membrane structure. This results could be checked based on FTIR peak assignment as shown in Figure 3.4.

Peak Position (cm <sup>-1</sup> )	Peak assignment
1583	Aromatic ring quadrant stretch
1485	Aromatic semi-ring stretch
1405	CH <sub>3</sub> in/out of phase stretch
1322	Sulfone SO <sub>2</sub> out of phase stretch
1296	C-O-C aryl ether in phase stretch
1241	Sulfone SO <sub>2</sub> in phase stretch
1149	S-O symmetric stretch
1103	S = O asymmetric stretch
1014	C = O-C aryl out of phase stretch
870	Aromatic para-substituted adjacent H wagging
834	Aromatic para-substituted adjacent H wagging
717	Aromatic C-H ring in plane bend
690	C-S-C out of phase stretch
558	SO <sub>2</sub> scissors deformation

Figure 3.4: FTIR Peak Assignment for PSF Membrane (Kuvarega, *et al.*,2018)

### 3.8.2.2 X-Ray Diffraction (XRD)

Crystallization phase structure analysis was performed by XRD to study the crystalline phase, crystalline size and crystalline structure of TiO<sub>2</sub> and N, S-CQDs/TiO<sub>2</sub> PSF membrane. In this analysis, 40 kV and 40 mA was used for XRD patterns. X-ray tube consists of continuous mode with CuK $\alpha$  radiation ( $\lambda = 0.15406$  nm), Ni filtered (0.02 mm) and masked (11.6 mm) and collimated with Soller slits (0.04 rad). Measurements was carried out in the range of  $2\theta$  ranging from 10 – 80 ° with scanning rate of 4° per minute. From XRD spectra, there was no significant change in XRD pattern between TiO<sub>2</sub> and N, S-CQDs /TiO<sub>2</sub> photocatalytic membrane. Hence, it can be showed that PSF polymer membrane was mainly amorphous because XRD can only detect crystalline structure instead of amorphous. For TiO<sub>2</sub> and N, S-CQDs/TiO<sub>2</sub> photocatalytic membrane, the crystallize size could be calculated from Debye Scherrer's formula as shown in Equation 3.2 (M.Li, *et al.*,2018).

$$d = k\lambda \times (\beta \cos\theta)^{-1} \quad (3.2)$$

where

$d$  = crystallite size, nm

$k$  = constant for CuK $\alpha$  (0.94)

$\beta$  = full width at half maximum (FWHM)

$\theta$  = angle between incoming X-ray and reflected lattice plane

### 3.8.2.3 Energy Dispersive X-Ray (EDX) Attached Scanning Electron Microscopy (SEM)

Surface morphology and surface elemental composition were investigated by SEM-EDX. SEM was to determine the photocatalytic membrane structure and dispersion of uniform size photocatalyst inside PSF membrane under 5000×, 1500×, 1000× and 500×. Cross-sections were prepared by cryogenically fracturing the membrane in liquid nitrogen. In another words, it could check whether excess photocatalyst has been supported on PSF UF membrane. If there is an excess of photocatalyst, the viscosity of solution is very high due to aggregation of nanoparticles and exist a delayed phase separation during layering process, causing membrane skin layer to be thicken and reduction of hydroxyl group (Q.Wang, *et al.*,2017). Thus, mass transfer of water molecules was limited which resulted in decreased water flux. EDX elemental analysis could detect the presence of TiO<sub>2</sub> and N, S-CQDs/TiO<sub>2</sub> nanoparticles present in membrane. This can be checked through the present of elemental image such as Ti, C, N, S and O.

### 3.8.2.4 Membrane Pore Analysis

In order to determine the permeation flux of membrane, porosity of membrane,  $\varepsilon$  and mean pore radius,  $r_m$  of fabricated membrane were calculated according to gravimetric method and Guerout-Elford-Ferry equation as shown in Equation 3.3 and 3.4 (Li et al., 2019). The membrane thickness was measured by using dial thickness gauge as shown in Figure 3.5.

$$\varepsilon (\%) = \frac{(W_w - W_d)}{\frac{\rho_H}{(W_w - W_d)} + \frac{W_d}{\rho_c}} \quad (3.3)$$

where

$W_w$  = weight of wet membrane (g)

$W_d$  = weight of dry membrane (g)

$\rho_H$  = density of water (0.998 g/cm<sup>3</sup>)

$\rho_c$  = density of PSF (1.24 g/cm<sup>3</sup>)

$$r_m = \sqrt{\frac{(2.9-1,7\varepsilon) \times 8\mu l q}{\varepsilon \times A \times \Delta P}} \quad (3.4)$$

where

$\mu$  = water viscosity ( $8.9 \times 10^{-4}$  Pa s)

$l$  = membrane thickness (m)

$q$  = volume of permeate water per unit time ( $\text{m}^3 \text{s}^{-1}$ )

$A$  = effective filtration area ( $0.001256 \text{ m}^2$ )

$\Delta P$  = load pressure (Pa)



Figure 3.5: Measurement of Membrane Thickness Using Dial Gauge Thickness

### 3.8.3 Membrane Permeation Flux

Membrane permeate flux is an important parameter to be studied to determine flux improvement of photocatalytic membrane. The pure water flux was conducted under three different transmembrane pressure (TMP): 1 bar, 2 bar and 3 bar. Thus, the flux was analysed based on the plot of permeate flux against TMP. Permeate flux of membrane could be calculated using Equation 3.5 (Chen, Fang and Chen, 2017).

$$J_p = V/(A \times t) \quad (3.5)$$

where

$J_p$  = membrane permeation flux at time  $t$  ( $L/m^2$  hr)

$V$  = volume of permeate (L)

$A$  = cross sectional area of membrane ( $m^2$ )

$t$  = filtration time (hours)

### 3.9 Experimental Set-up for Photodegradation Process

The experiment was carried out in batch mode. The photocatalytic performance of N, S-CQDs/TiO<sub>2</sub> deposited on PSF membrane was determined by measure the rate of photodegradation of DCF solution under visible light, UV light and environment light irradiation. A strip of square shape with certain dimension of photocatalytic membrane was suspended in 200 ml of DCF solution with concentration of 10 ppm under stirring condition. Prior to photocatalytic reactions, the photocatalytic membrane was immersed in the DCF solution for 30 minutes in the dark condition to reach adsorption-desorption equilibrium. Then, the photodegradation process was conducted under three different photo sources respectively. 10 ml of DCF solution were taken out in a 30 minutes interval using syringe for 120 minutes including initial DCF concentration before and after dark condition. Then, the concentration of collected samples were determined by UV-vis spectrophotometer. The photocatalytic membrane experimental set up shows in Figure 3.6.

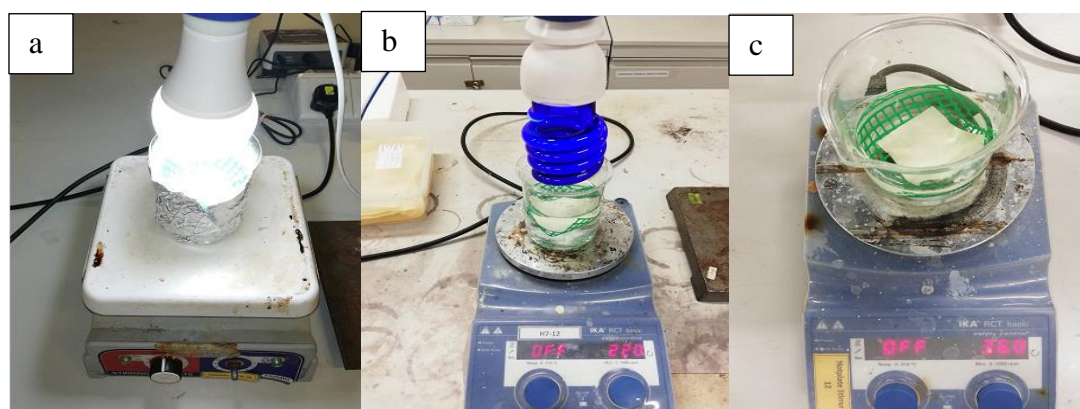


Figure 3.6: Schematic Illustration of Photocatalysis Experiment; (a) Visible Light Irradiation (b) UV Light Irradiation (c) Environment Light Irradiation

### 3.10 Experimental Set-up for Permeation Flux Test

TiO<sub>2</sub> and N, S-CQD/TiO<sub>2</sub> with differ loading of NCQDs embedded UF membrane were characterized by measuring the pure water flux. Experiment was conducted in a dead end cell (250 ml volume) with a membrane effective surface area of 12.56 cm<sup>2</sup> (Vatanpour, et al.,2011). The photocatalytic membrane was left on a small rigid circular metal plate and placed inside the cell. The cell was connected with a pressure gauge and pressurized nitrogen gas was used to force the water through the membrane as shown in Figure 3.7. Each of the photocatalytic membrane was initially pressurized at 4 bar for 30 minutes, then the pressure was adjusted to operating pressure of 3, 2 and 1 bar. The water flux was calculated using Equation 3.3 based on amount of time used to fill 100 ml of filtrate (water) in 250 ml of beaker.



Figure 3.7: Experimental Set Up of Permeation Flux Test

### 3.11 Parameter Studies

#### 3.11.1 Effect of NCQDs Loading on N, S-CQDs/TiO<sub>2</sub>

The effect of NCQDs loading on N, S-CQDs/TiO<sub>2</sub> is an important parameter to be investigated to find the optimum photocatalyst loading for maximizing the photodegradation efficiency of DCF and achieve higher permeate flux. The effect of NCQDs loading was studied using 1.0 g, 1.5 g, and 2.0 g. Different weight of NCQDs were mixed with 0.2g of prepared TiO<sub>2</sub> in the reflux process before phase inversion process. The formation of hybrid photocatalyst at different NCQDs loading was carried toward the formation of photocatalytic membrane and photodegradation efficiency was tested. The loading of NCQDs, TiO<sub>2</sub>, PSF, PVP and NMP for the formulation of photocatalytic membrane were showed in Table 3.3.

Table 3.3: Formulation of Photocatalytic Membrane

NCQDs Loading (g)	TiO <sub>2</sub> Loading (g)	Loading (g) Based On 50g of Casting Solution		
		PSF	PVP	NMP
0 (Blank Control)	0.2	8.5	0.085	41.5
1	0.2	8.5	0.085	41.5
1.5	0.2	8.5	0.085	41.5
2	0.2	8.5	0.085	41.5

#### 3.11.2 Effect of Light Sources

The effect of light sources on photodegradation of DCF were studied using environment light, 80 W of visible lamp as visible light source and 80 W of UV lamp as UV light source. Different light sources have their own wavelength which can be used as an indicator to determine the photoluminescence efficiency for each type of photocatalytic membrane. Environment light, visible light and UV light have a wavelength of >380 nm, >400 nm and <380 nm respectively.

#### 3.11.3 Effect of Photocatalytic Membrane Area

The effect of membrane area on photodegradation of DCF were conducted using different size of membrane which was 5 cm × 5 cm, 4 cm × 4 cm and 3 cm × 3 cm. Different membrane area will give different photodegradation efficiency due to dispersibility of nanoparticles and amount of active sites available for the photocatalysis process.

### 3.11.4 Effect of Transmembrane Pressure (TMP)

For permeation flux analysis, instead of membrane fouling, TMP is also an important parameter that can affect the permeation flux of membrane. TMP is driving force or pressure gradient of membrane that require to press water through the membrane. TMP is needed because water will experience a great resistance to pass through the membrane due to different pore size of membrane. However, if the pressure is continuously applied, it will experience flux decline. Hence, effect of TMP must be studied so that appropriate TMP can be selected and membrane can operate at longer time without cleaning.

### 3.12 Kinetic Study

Kinetic model has been investigated and studied to predict the rate of photodegradation efficiency of DCF pharmaceutical waste. Referring to the study by Hou, *et al.* (2012), photodegradation kinetics of DCF in UF photocatalytic membrane can be described by Langmuir – Hinshelwood model as shown in Equation 3.6.

$$r = -dC/dt = kKC/(1 + KC) \quad (3.6)$$

where

$r$  = reaction rate (mg/L min)

$C$  = concentration of DCF (mg/L)

$t$  = treatment time (minutes)

$k$  = reaction rate constant of surface active site (mg/L min)

$K$  = langmuir adsorption equilibrium constant of DCF (L/mg)

At low DCF concentration (< 15 mg/L) and weak adsorption, KC factor is negligible in respect to unity and Equation 3.6 can be rewritten to pseudo – first order kinetics as shown in Equation 3.7 (Zhou, *et al.*,2018). Concentration of DCF after treatment time,  $t$  can be found through integration of Equation 3.7 as shown in Equation 3.8.

$$r = -dC/dt = kKC = k_{app}C \quad (3.7)$$

$$\ln(C/C_0) = -kKt = -k_{app}t \quad (3.8)$$

where

$k_{app}$  = apparent rate constant of first order,  $k_{app} = kK$

$C_0$  = initial DCF solution concentration after adsorption equilibrium in dark (mg/L)

A plot of  $\ln(C_0/C)$  vs  $t$  gives a straight line and  $k_{app}$  represents gradient of straight line. From Equation 3.8,  $K$  is a constant and depend on type of pollutant used while  $k$  dependent on photocatalyst amount, solution pH and  $C_0$ .

### 3.13 UV-Vis Spectrophotometer

Changes in concentration of DCF solution were determined using UV-Vis spectrophotometer. Remaining DCF concentration in sample can be determined by using UV-Vis spectrophotometry. Prior the photodegradation experiment, a calibration curve of absorbance versus concentration was plotted using initial known DCF solution concentration which was 10 ppm. Based on Beer-Lambert Law, absorbance is directly proportional to DCF concentration. Hence, the identified DCF absorption can be converted to concentration through plotted calibration curve as shown in Figure 3.8. The photodegradation efficiency can be calculated through Equation 3.9.

$$\text{Photodegradation Efficiency}(\%) = [1 - (C_t/C_0) \times 100\%] \quad (3.9)$$

where

$C_0$  = initial DCF concentration, mg/L (ppm)

$C_t$  = DCF concentration at time  $t$ , mg/L (ppm)

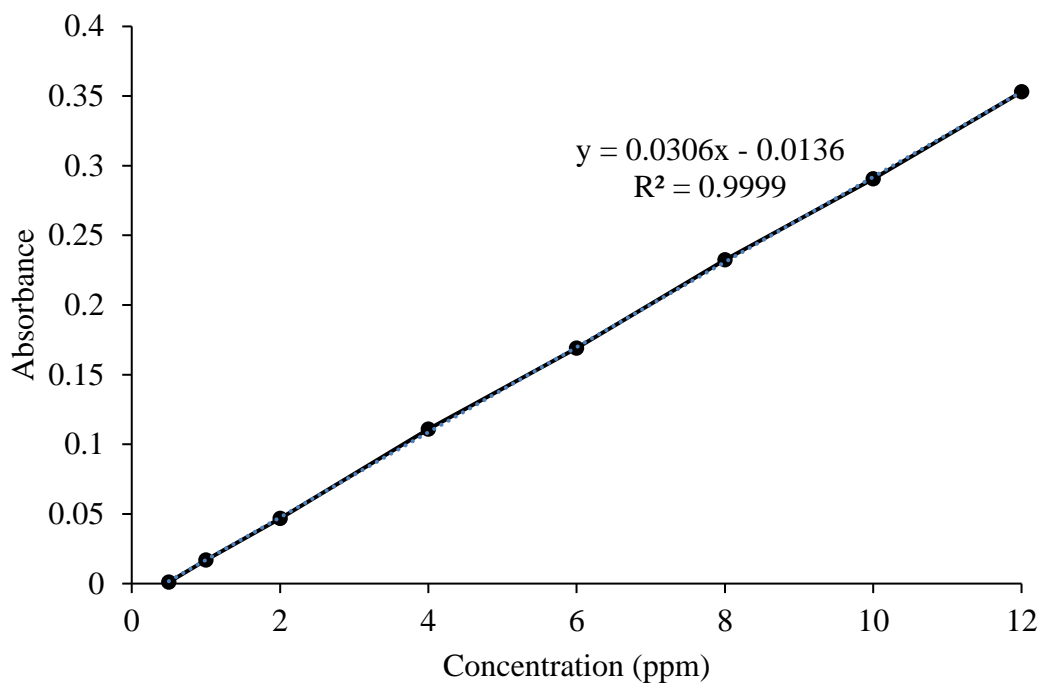


Figure 3.8: Calibration Curve for DCF Model Pollutant

### 3.14 Gantt Chart

The schedule for final year FYP II presented in Figure 3.9.

Week	1	2	3	4	5	6	7	8	9	10	11	12	13	14
Laboratory Work Planning	■	■												
Laboratory Work			■	■	■	■	■	■	■					
Characterization										■	■			
Chapter 4 and 5												■	■	
Compilation and Presentation														■

Figure 3.9: FYP II Schedule

## CHAPTER 4

### RESULTS AND DISCUSSION

#### 4.1 Introduction

Laboratory tests were conducted to investigate the performance of the synthesized N, S-CQDs/TiO<sub>2</sub> MMM. Related analytical instrument such as UV-vis spectrophotometer, FTIR, XRD, SEM and EDX were used to characterize the composition, chemical structure, crystallinity and size of the synthesized photocatalytic membrane. Furthermore, the possible mechanism of photocatalytic degradation for DCF and their kinetic model were proposed. Lastly, overall performance of pure TiO<sub>2</sub> membrane and N, S-CQDs/TiO<sub>2</sub> membrane with different NCQDs loading were compared by conducting photodegradation and permeation flux test.

##### 4.1.1 UV-Vis Absorption Spectra of TiO<sub>2</sub> and N, S-CQDs/TiO<sub>2</sub>

In order to investigate the functions of N, S-CQDs dopant, the light absorption property of pristine TiO<sub>2</sub> and different loading of NCQDs on N, S-CQDs/TiO<sub>2</sub> hybrid composites were analysed through UV-Vis spectrophotometer. Figure 4.1 shows different optical properties between TiO<sub>2</sub> and N, S-CQDs/TiO<sub>2</sub> composite with different loading. Compare to pristine TiO<sub>2</sub>, N, S-CQDs/TiO<sub>2</sub> have a broad UV-Vis absorption below 400 nm. Besides, it can be observed that the absorption intensity of N, S-CQDs/TiO<sub>2</sub> hybrid composites increase with increasing loading of NCQDs. In addition, 1.5g and 2.0g N, S-CQDs/TiO<sub>2</sub> composite have better absorption intensity near visible light range (400 nm). This confirms that N, S-CQDs dopant has an ability to shift the light absorption range of TiO<sub>2</sub> from UV region to visible light region. On the other hand, 2.0g N, S-CQDs/TiO<sub>2</sub> possesses lower absorption intensity near visible light range compare to 1.5g N, S-CQDs/TiO<sub>2</sub>. Referring to the study by Han, et al. (2014), weak visible light absorption by higher loading N, S-CQDs/TiO<sub>2</sub> is due to over dose of NCQDs nanoparticles on the surface of N, S-CQDs/TiO<sub>2</sub> which tend to aggregate together and form lager particles (>10 nm). Table 4.1 shows the bandgap energy for each type of photocatalyst which can calculated by bandgap equation as shown in Equation 3.1.

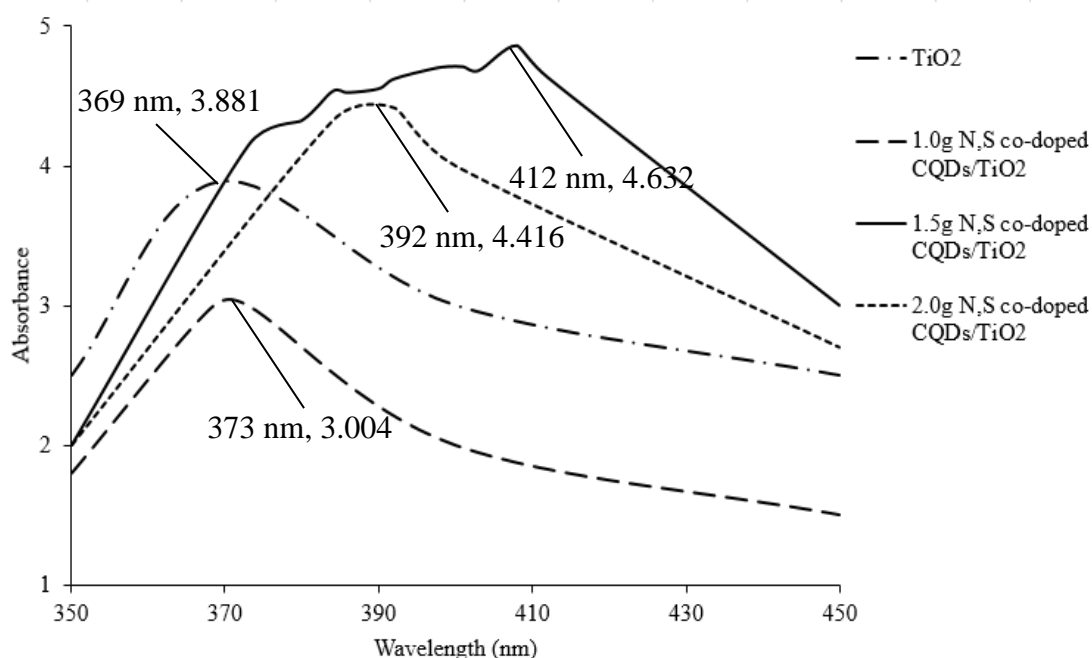


Figure 4.1: UV-Vis Absorption (ABS) Spectra of  $\text{TiO}_2$  and Different Loading of NCQDs on N, S-CQDs/ $\text{TiO}_2$  Composite

Table 4.1: Bandgap Energy for  $\text{TiO}_2$  and N, S-CQDs/ $\text{TiO}_2$  with Different Loading

Photocatalyst	Maximum Absorption Peak Wavelength (nm)	Bandgap Energy (eV)
$\text{TiO}_2$	369	3.363
1.0g N, S-CQDs/ $\text{TiO}_2$	373	3.327
1.5g N, S-CQDs/ $\text{TiO}_2$	412	3.012
2.0g N, S-CQDs/ $\text{TiO}_2$	392	3.165

#### 4.1.2 Fourier Transform Infrared (FTIR)

Figure 4.2, 4.3 and 4.4 showed FTIR spectrum of different loading of N, S-CQDs/ $\text{TiO}_2$  membrane in the wavelength range of  $500\text{--}3900\text{ cm}^{-1}$ . According to the study by Kuvarega, et al. (2018), all pure PSF signature peaks were visible in the composite membranes. The peak at  $1583\text{ cm}^{-1}$  indicated the characteristic stretch of aromatic ring quadrant. The peak of  $1241\text{ cm}^{-1}$  was associated with phase stretching of sulfone ( $\text{SO}_2$ ). The peak of  $1014\text{ cm}^{-1}$  represented C=O=C aryl out of phase stretch. The peak at  $834\text{ cm}^{-1}$  meant aromatic para-substituted adjacent H wagging. The peak of  $690\text{ cm}^{-1}$  and  $558\text{ cm}^{-1}$  was associated with C-S-C out of phase stretch and  $\text{SO}_2$  scissors deformation. This confirms that the entrapped of N, S-CQDs/ $\text{TiO}_2$  nanoparticles did not disrupt the polymer structure. Besides, FTIR spectra reveals two important peak at  $3438\text{ cm}^{-1}$  and weak peak at  $1660\text{ cm}^{-1}$ , which correspond to O-H and C=O stretching vibrations

(Aghamali, et al.,2018). The new appeared peaks in N, S-CQDs/TiO<sub>2</sub> composite at 2974 cm<sup>-1</sup> (CH<sub>2</sub>), 1157 cm<sup>-1</sup> (C=O), 1492 cm<sup>-1</sup> (N-H), 635 cm<sup>-1</sup> (C-S-C) and 1221 cm<sup>-1</sup> (C=S) are ascribed to the addition of N, S-CQDs, evidently confirming the existence of N and S in the N, S-CQDs/TiO<sub>2</sub> composite (Nemati, et al.,2018; Hu, et al.,2018). It can be confirmed that NCQDs had abundant amino and carboxyl group on their surface from the above mentioned peak. Based on the Figure 4.3, it can be observed that 1.0g N, S-CQDs/TiO<sub>2</sub> have a broad peak centred at 3438 cm<sup>-1</sup> compared to TiO<sub>2</sub> membrane due to the presence of many hydroxyl groups on the N, S-CQDs. Thus, it can be confirmed that doping of N, S-CQDs on TiO<sub>2</sub> membrane can greatly improve the hydrophilicity.

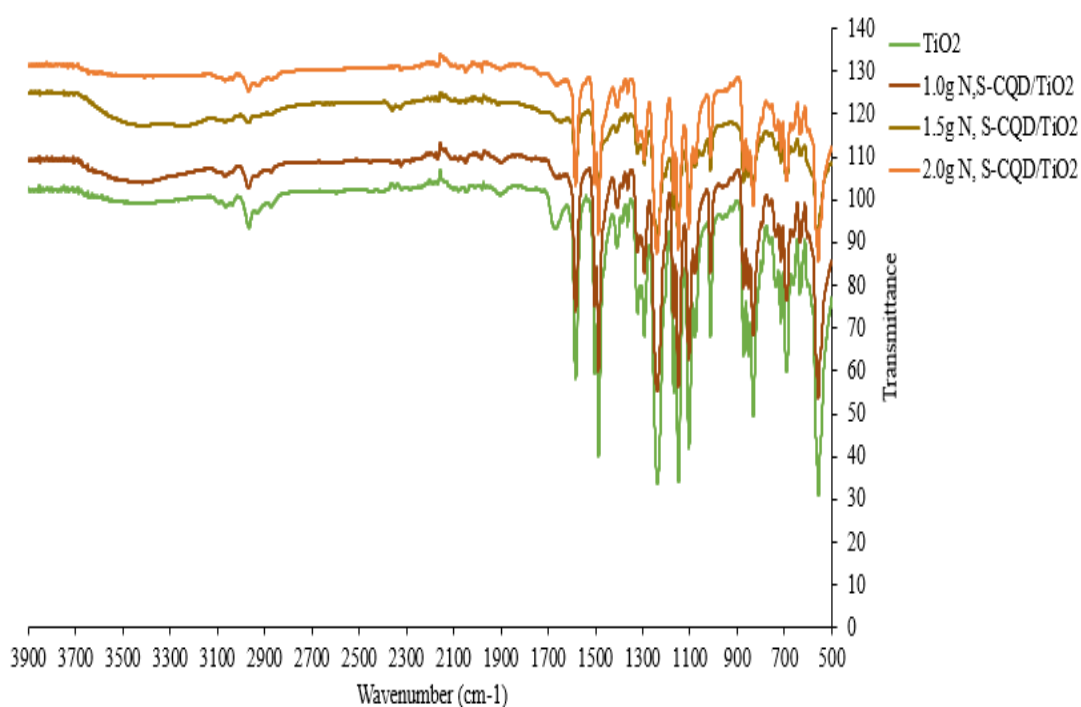


Figure 4.2: FTIR Spectra of Pure and Photocatalytic PSF Membrane in the Wavelength Range Between 500–3900 cm<sup>-1</sup>

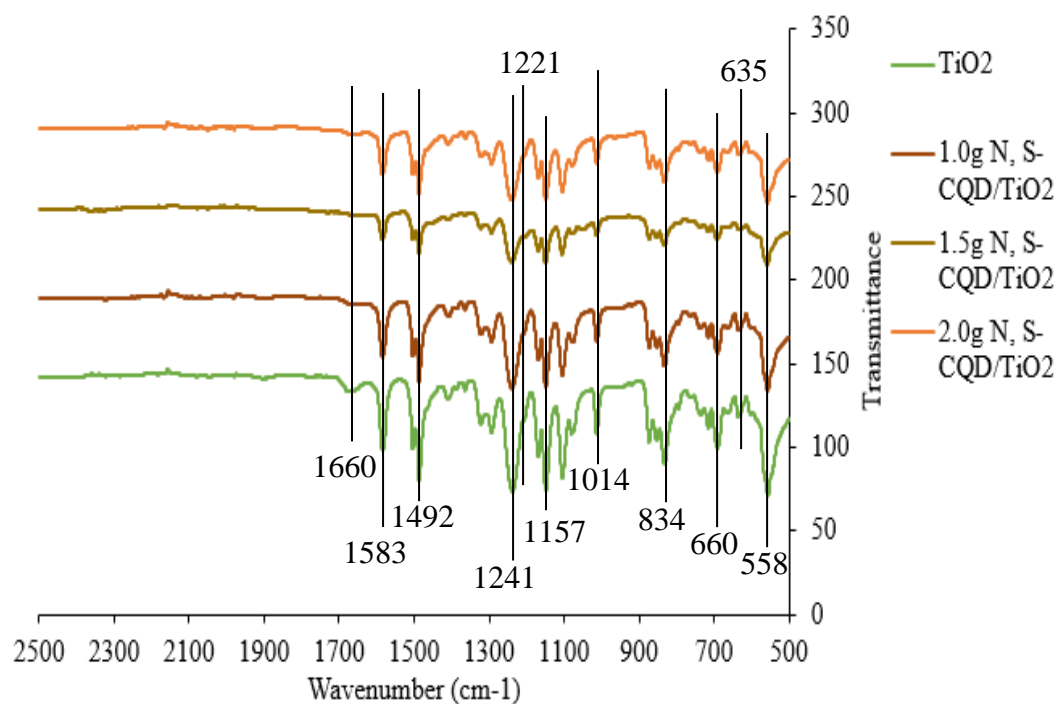


Figure 4.3: FTIR Spectra of Pure and Photocatalytic PSF Membrane in the Wavelength Range Between 500–2500  $\text{cm}^{-1}$

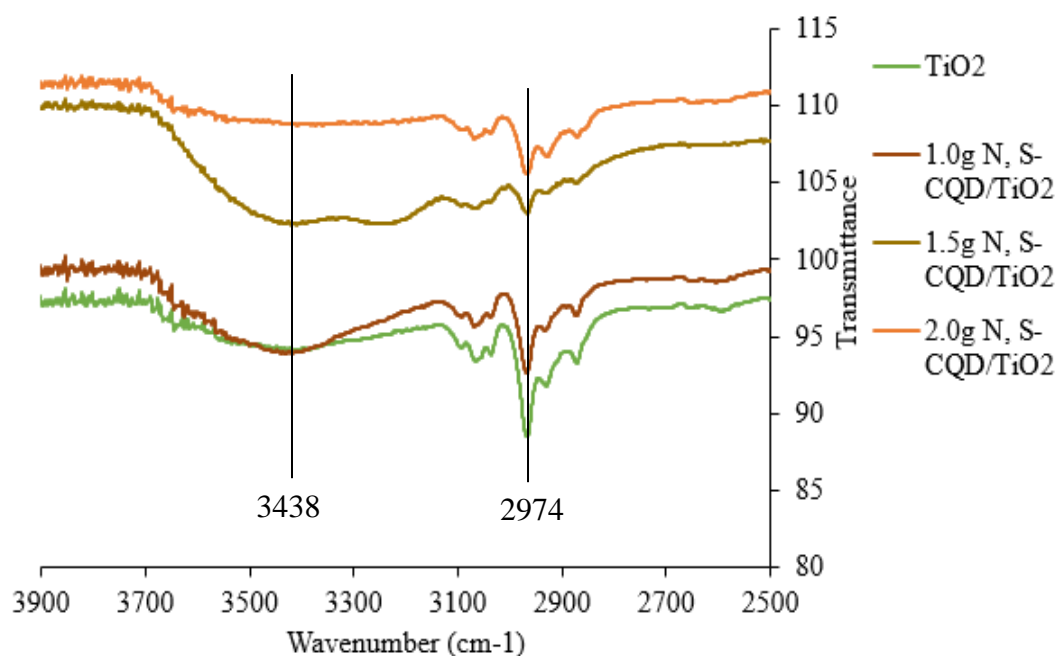


Figure 4.4: FTIR Spectra of Pure and Photocatalytic PSF Membrane in the Wavelength Range Between 2500–3900  $\text{cm}^{-1}$

### 4.1.3 XRD Analysis of TiO<sub>2</sub> and N, S-CQDs/TiO<sub>2</sub>

The phase structure of the as synthesized TiO<sub>2</sub> and N, S-CQDs/TiO<sub>2</sub> composites membrane were determined by XRD. Based on Figure 4.5, both diffraction pattern of TiO<sub>2</sub> and N, S-CQDs/TiO<sub>2</sub> composites exhibited same characteristic diffraction peaks of TiO<sub>2</sub>. The additional peaks at approximately 2θ values of 23°, 38°, 45°, 65° and 78° corresponding to (1 0 1), (0 0 4), (2 0 0), (2 0 4) and (3 0 1) lattice planes of anatase TiO<sub>2</sub> (Zhang, et al.,2016). This indicates that N, S-CQDs loading did not change the crystallographic phase of TiO<sub>2</sub> supports. Ge, Zhu and Rudolph (2011) found that PSF polymer was mainly amorphous and presented one prominent peak at 2θ =18.23°. Besides, it can be confirmed that N, S-CQDs were deposited on the TiO<sub>2</sub> surface instead of incorporated into it due to no shift in diffraction peak of hybrid nanocomposites compared to pure TiO<sub>2</sub> (Fontelles-Carceller, et al.,2017). According to Zhang, et al. (2013), the absence of N, S-CQDs signal in Figure 4.5 can be explained by small quantity, low crystallinity and high dispersion of N, S-CQDs in N, S-CQDs/TiO<sub>2</sub> composites.

On the other hand, average crystallite size can be calculated using Debye Scherrer's formula as shown in Equation 3.2. The average crystallite size was calculated based on three strongest peak appeared in XRD spectra. Based on Table 4.2, it can be observed that with the increasing of NCQDs loading, the crystallite size increase which gives more open structure of photocatalytic membrane. Thus, higher permeation flux can be obtained. However, when there is an excessive of NCQDs loading, the crystallite size decrease and even lower than crystallite size of TiO<sub>2</sub>. This would probably due to irregular positioning and aggregation of NCQDs nanoparticles on membrane pore which result in much lower flux.

Table 4.2: Crystallite Size of TiO<sub>2</sub> and Different Loading of N, S-CQDs/TiO<sub>2</sub> Photocatalytic Membrane

Photocatalytic Membrane	Crystallite Size (nm)
TiO <sub>2</sub>	69.693
1.0g N, S-CQDs/TiO <sub>2</sub>	71.573
1.5g N, S-CQDs/TiO <sub>2</sub>	72.610
2.0g N, S-CQDs/TiO <sub>2</sub>	66.860

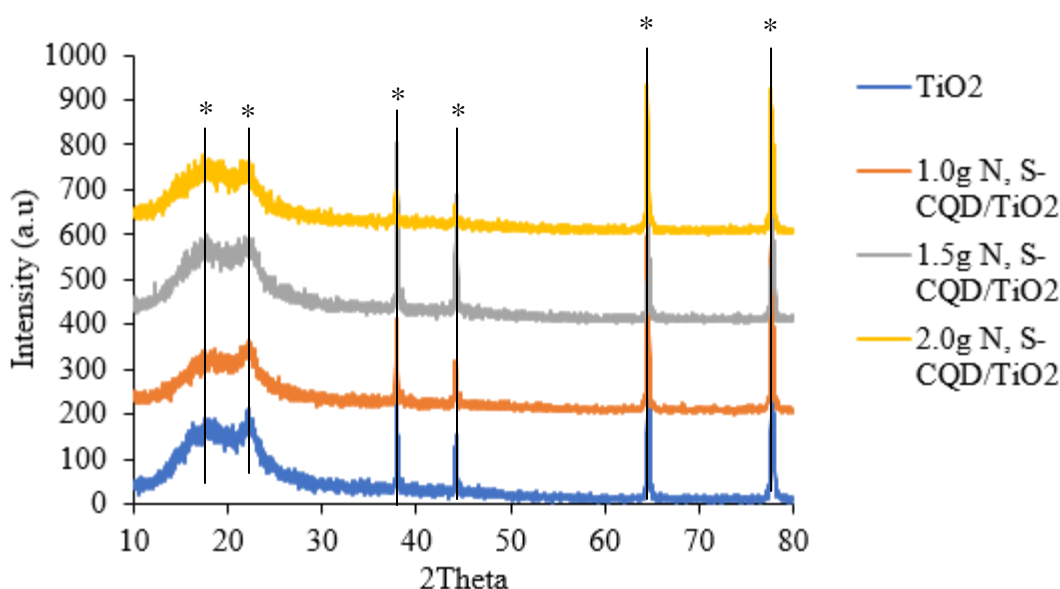


Figure 4.5: XRD Patterns of  $\text{TiO}_2$  and N, S-CQDs/ $\text{TiO}_2$  Composites with Different Amount of NCQDs

#### 4.1.4 Morphology and Composition Analysis of $\text{TiO}_2$ and N, S-CQDs/ $\text{TiO}_2$ Photocatalytic Membrane

In order to understand the influence of photocatalyst embedding on the PSF membrane structure and overall composition, the plane and cross-section of photocatalytic membrane prepared from  $\text{TiO}_2$ , 1.0g N, S-CQDs/ $\text{TiO}_2$ , 1.5g N, S-CQDs/ $\text{TiO}_2$  and 2.0g N, S-CQDs/ $\text{TiO}_2$  were observed using SEM-EDX. The photocatalytic membrane specimens were coated with conducting layer before the observations. The plane view of as prepared mixed matrix membrane showed in Figure 4.6 while the cross sectional view showed in Figure 4.7 - 4.10. Based on Figure 4.6, all of the images show a highly porous surface with some small  $\text{TiO}_2$  nanoparticles loaded on photocatalytic membrane surface. Besides, the addition of N, S-CQDs results in an increment of pore size in skin layer compared with pure  $\text{TiO}_2$  PSF membrane. N, S-CQDs particles cannot be observed on the membrane surface due to the magnification of the SEM. The pore structure of 1.5g and 2.0g N, S-CQDs/ $\text{TiO}_2$  membrane was not clearly be observed due to irregular positioning of nanoparticles and higher concentration of sol in the coagulation bath which forms a dense selective top layer on the membrane surface (Zhang, et al.,2017).

Referring to the cross sectional view, all the photocatalytic membrane exhibits a typical asymmetric structure consists of thin dense top layer and a finger like porous supporting later. As indicated from the three figure of cross sectional view of

photocatalytic membrane, 2.0g N, S-CQDs/TiO<sub>2</sub> composite membrane has narrower pore size which followed by TiO<sub>2</sub>, 1.0g N, S-CQDs/TiO<sub>2</sub> and 1.5g N, S-CQDs/TiO<sub>2</sub>. Furthermore, it can be noticed that the introduction of hydrophilic N, S-CQDs nanoparticles had widen the pore channels of supporting layer of hybrid membrane compare to pure TiO<sub>2</sub> membrane. As the loading of NCQDs increased, it can be observed that intermediate layer showed a sponge like structure as shown in Figure 4.8 and 4.9. This can be observed that the finger like pores in the TiO<sub>2</sub> membrane bottom gradually become bigger which was due to the enhancement of the mass transfer of water molecules during phase inversion process (Wang, et al.,2017). When the content of NCQDs increased to 2.0g, the pore walls started to formation in sub layer and macro-void size reduced as shown in Figure 4.10 (Vatanpour, et al.,2011). Hence, the porosity of the membrane was decreased. This might due to delay in liquid-liquid de-mixing process arising from the higher viscosity of sol and lower phase inversion rate (Rawindran et al., 2019).

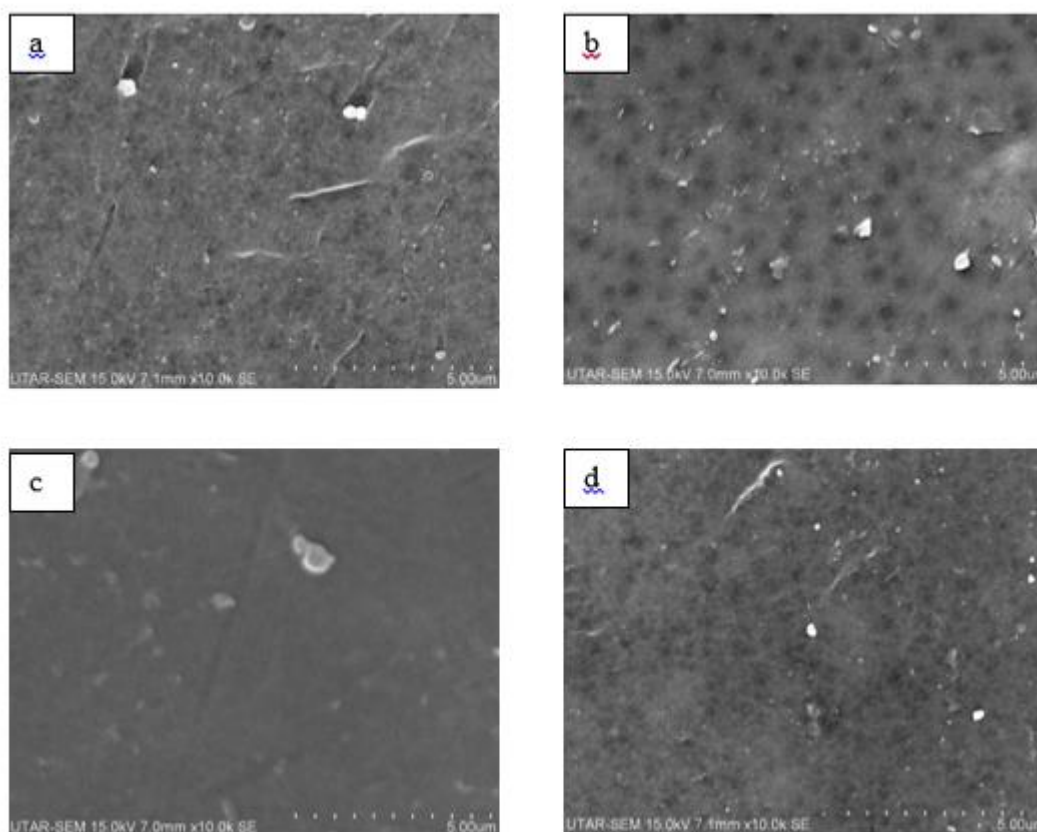


Figure 4.6: SEM Images of Photocatalytic Membrane; (a) TiO<sub>2</sub> (b) 1.0g N, S-CQDs/TiO<sub>2</sub> (c) 1.5g N, S-CQDs/TiO<sub>2</sub> (d) 2.0g N, S-CQDs/TiO<sub>2</sub>

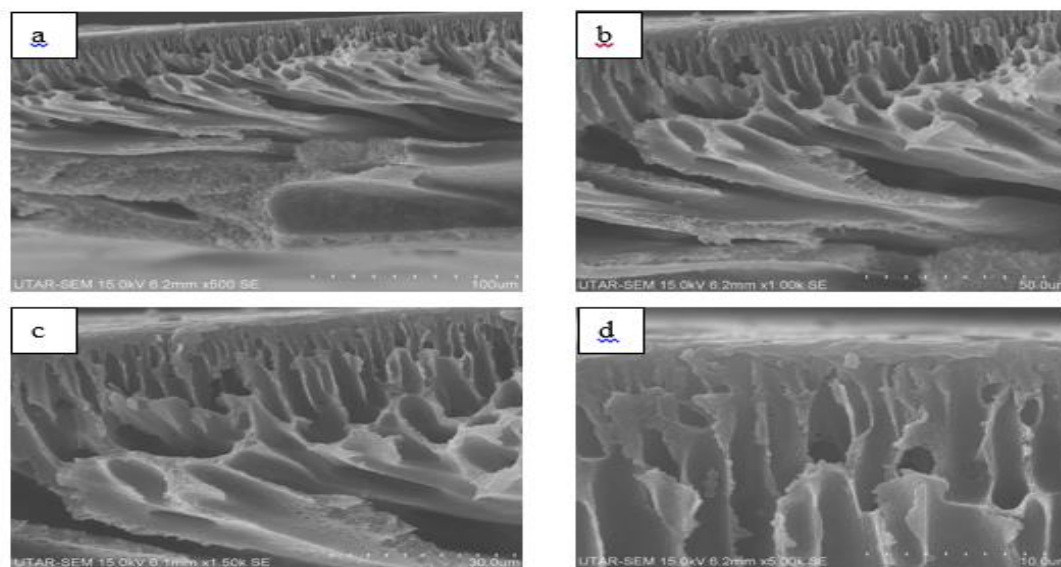


Figure 4.7: SEM Image of Cross Sectional View of TiO<sub>2</sub> Membrane at Four Magnification; (a) ×500 (b) ×1000 (c) ×1500 (d) ×5000

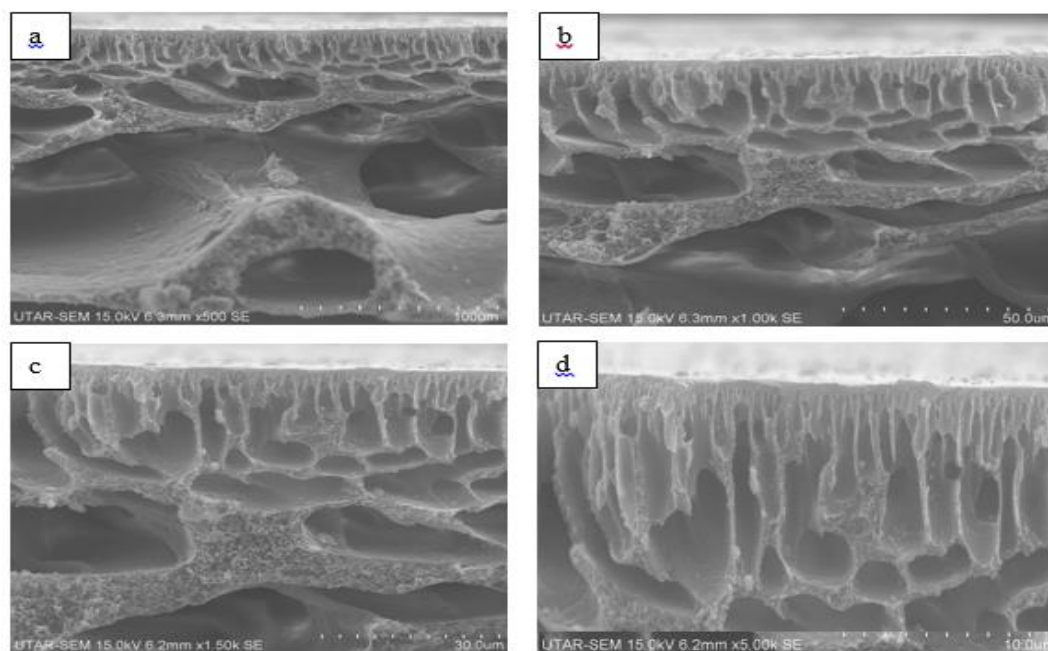


Figure 4.8: SEM Image of Cross Sectional View of 1.0g N, S-CQDs/TiO<sub>2</sub> Membrane at Four Magnification; (a) ×500 (b) ×1000 (c) ×1500 (d) ×5000

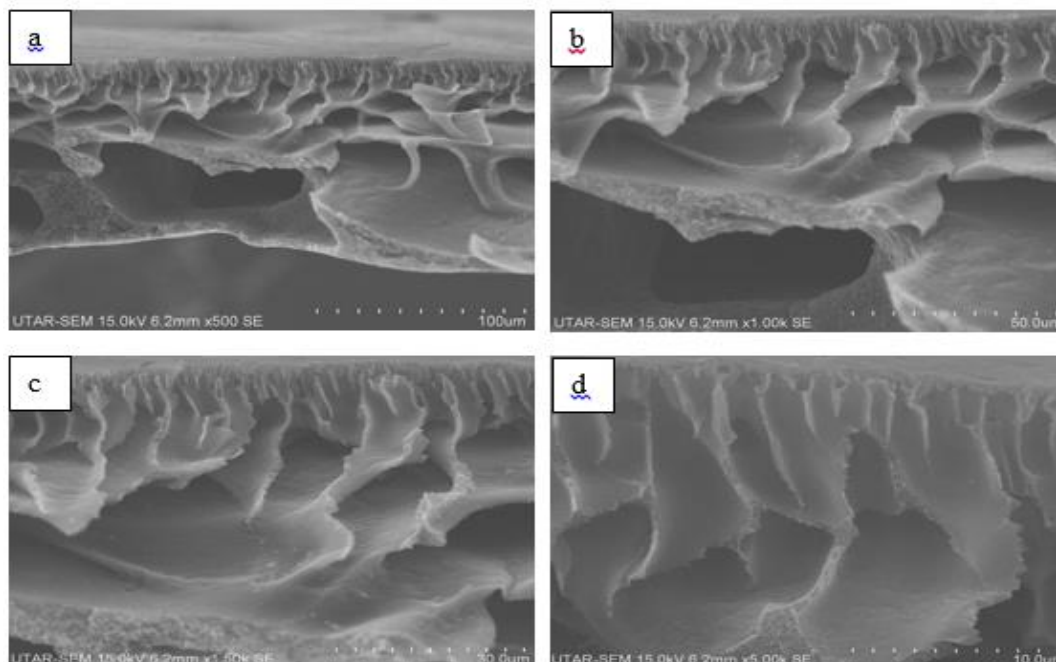


Figure 4.9: SEM Image of Cross Sectional View of 1.5g N, S-CQDs/TiO<sub>2</sub> Membrane at Four Magnification; (a)  $\times 500$  (b)  $\times 1000$  (c)  $\times 1500$  (d)  $\times 5000$

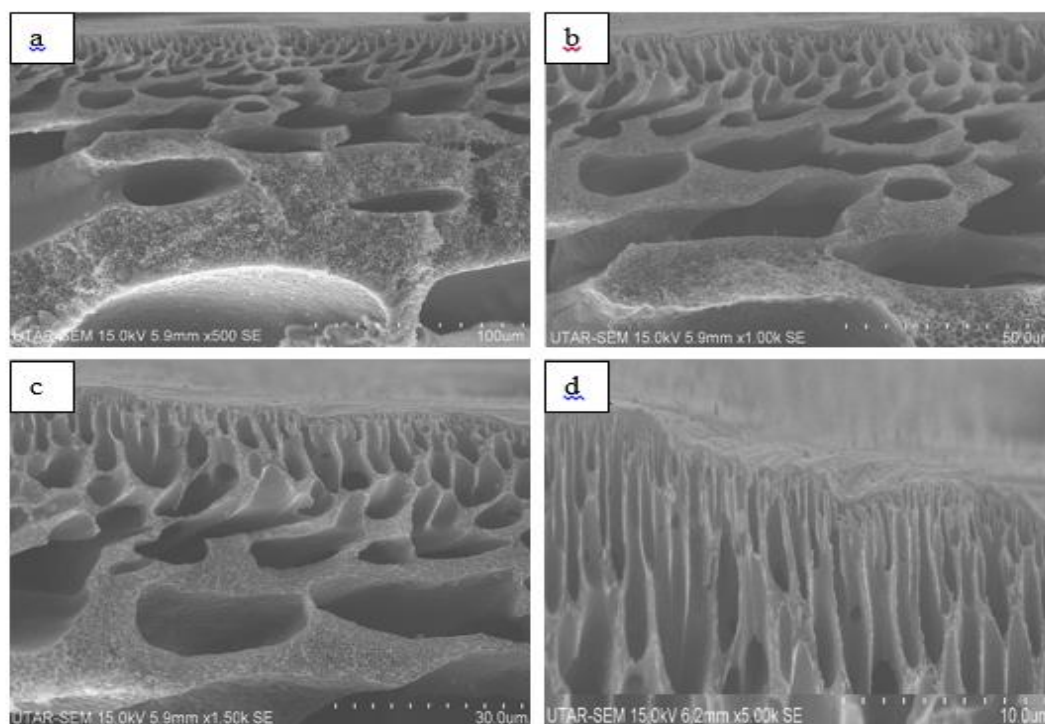


Figure 4.10: SEM Image of Cross Sectional View of 2.0g N, S-CQDs/TiO<sub>2</sub> Membrane at Four Magnification; (a)  $\times 500$  (b)  $\times 1000$  (c)  $\times 1500$  (d)  $\times 5000$

The elemental compositions of the mixed matrix membranes were confirmed through EDX analysis as shown in Figure 4.11. From the EDX spectra, peaks associated with composition of carbon (C), oxygen (O) and sulphur (S) confirming that the membrane was indeed pure PSF (Kuvarega et al., 2018a). The pure TiO<sub>2</sub> membrane showed an additional peak of titanium (Ti) due to the presence of TiO<sub>2</sub> and no peak for N was noticed from the analysis. This indicated that the membrane only incorporated with TiO<sub>2</sub> photocatalyst. For 1.5g N, S-CQDs/TiO<sub>2</sub> membrane, there was an additional peak of nitrogen (N), Ti and increment of S content compare to pure TiO<sub>2</sub> membrane. This confirming the incorporation of N, S-CQDs/TiO<sub>2</sub> photocatalyst in the membrane (Bento, Correa and Pillis, 2019; Zhang, et al.,2016). On the other hand, EDX results can be used to check the hydrophilicity of photocatalytic membrane by determine the changes of ratio of N to C. The ratio of N to C is 0.0254 for 1.0g N, S-CQDs/TiO<sub>2</sub> membrane and 0.0169, 0.0208 for 1.5g N, S-CQDs/TiO<sub>2</sub> and 2.0g N, S-CQDs/TiO<sub>2</sub> composite membrane respectively. The ratio of N to C is smaller when NCQDs loading increase to 1.5g, suggesting that some functional group containing N was converted into carboxylic functional group and result in higher hydrophilicity (Zhang, et al.,2017). The N to C ratio increase when NCQDs loading is 2.0g due to the present of excessive N and deficit of C. This will lead to flux decline because formation of carbon chemical bond to form carboxylic functional group was limited.

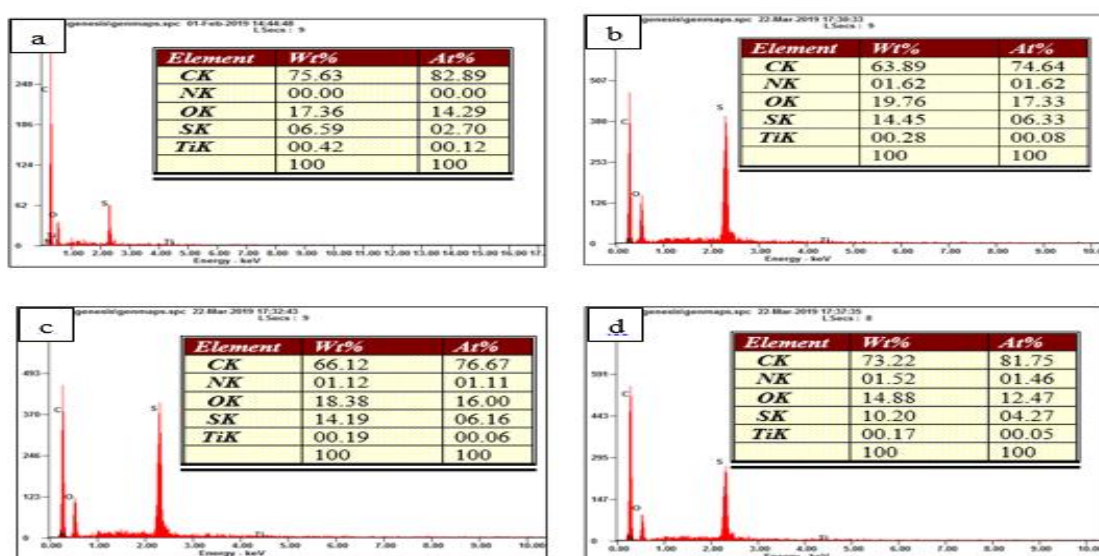


Figure 4.11: EDX Analysis; (a) TiO<sub>2</sub> Membrane (b) 1.0g N, S-CQDs/TiO<sub>2</sub> Membrane (c) 1.5g N, S-CQDs/TiO<sub>2</sub> Membrane (d) 2.0g N, S-CQDs/TiO<sub>2</sub> Membrane

## 4.2 Photocatalytic Performance of Prepared Photocatalytic Membrane

The photocatalytic ability for degradation of prepared 10 ppm DCF model pollutant via 25 cm<sup>2</sup> of TiO<sub>2</sub> and N, S-CQDs/TiO<sub>2</sub> membrane with differ content were evaluated under three photo sources which are UV light irradiation ( $\lambda < 380$  nm), visible light irradiation ( $\lambda > 400$  nm) and environment light irradiation ( $\lambda > 380$  nm) as shown in Figure 4.12, 4.13 and 4.14. C<sub>0</sub> is the initial concentration of DCF while C is the corresponding concentration in real time. Before the photodegradation experiment was carried out, an adsorption–desorption equilibrium was carried out for 30 minutes.

As notice from the three figures, DCF has been greatly degraded in the first 30 minutes during dark condition of adsorption – desorption equilibrium. This results is mainly due to adsorption for DCF which is positively correlated with the amounts of NCQDs in the hybrid composites. Referring to the study by Hu, et al. (2018), the contribution of N, S-CQDs improved the absorbability for DCF which is the main reasons for enhanced photocatalytic performance among all of the N, S-CQDs/TiO<sub>2</sub> composites.

The rate of photodegradation after the 30 minutes adsorption–desorption equilibrium mostly increased when N, S-CQDs/TiO<sub>2</sub> were incorporated into the PSF membrane. Referring to Figure 4.13, no obvious DCF removal was observed using the pure TiO<sub>2</sub> membrane after 2 hours visible light irradiation. This is because the strong absorption peak for TiO<sub>2</sub> photocatalyst at around 370 nm (Figure 4.4) which is more suitable to be excited by low wavelength UV light. The strong absorption peak at 370 nm means TiO<sub>2</sub> photocatalyst able to gain much excitation energy under this UV light wavelength and release more photogenerated electron to degrade the pollutant. On the other hand, the increment of photodegradation efficiency at irradiation time between 30 minutes and 150 minutes for each type of photocatalytic membrane under three different photo sources were showed in Table 4.3, 4.4 and 4.5. Based on Table 4.3, pure TiO<sub>2</sub> membrane has the highest photodegradation rate under UV light irradiation among the three photo sources. This was because UV light irradiation can gave the highest photodegradation rate due to shorter wavelength (<380 nm) which provided TiO<sub>2</sub> sufficient photoexcitation energy. Hence, TiO<sub>2</sub> photocatalyst had sufficient energy to overcome the wide band gap energy of TiO<sub>2</sub> and excited the electron from VB to CB (H.Li, *et al.*,2018).

Then, light sources study was further tested using visible light and environmental light irradiation. As shown in Table 4.4 for visible light photodegradation test, the changes of photodegradation efficiency increase from 2.71% for 1.0g N, S-CQDs/TiO<sub>2</sub> membrane to 12.59 % at 1.5g N, S-CQDs/TiO<sub>2</sub> membrane and then dropped to 10.65% at 2.0g N, S-CQDs/TiO<sub>2</sub>. For environment light photodegradation test, the changes of photodegradation efficiency increase from 13.01% for 1.0g N, S-CQDs/TiO<sub>2</sub> membrane to 13.72 % at 1.5g N, S-CQDs/TiO<sub>2</sub> membrane and then dropped to 13.53% at 2.0g N, S-CQDs/TiO<sub>2</sub> as shown in Table 4.5. Based on these two results, it revealed that the addition of an appropriate amount of NCQDs on N, S-CQDs could improve the photocatalytic performance of TiO<sub>2</sub>. The results show that although more NCQDs loaded on N, S-CQDs/TiO<sub>2</sub> composite could help to promote the adsorption of DCF, superfluous DCF accumulation on photocatalyst surface might suppress the substance migration and the active sites of TiO<sub>2</sub> surface also would be buried by overloaded NCQDs (Hu, et al.,2018). These resulted in a hindrance of photodegradation process which explained the lower photocatalytic quantum efficiency for 2.0g N, S-CQDs/TiO<sub>2</sub> compared to 1.5g N, S-CQDs/TiO<sub>2</sub> composite membrane. Besides, the bandgap energy of 1.5g N, S-CQDs/TiO<sub>2</sub> composite membrane was lower than 2.0g N, S-CQDs/TiO<sub>2</sub> composite membrane as shown in Table 4.1. As a result, 2.0g N, S-CQDs/TiO<sub>2</sub> photocatalytic membrane can produced lesser amount of photogenerated electrons and holes which were responsible for DCF photodegradation as compared to 1.5g N, S-CQDs/TiO<sub>2</sub> photocatalytic membrane. This is because 2.0g N, S-CQDs/TiO<sub>2</sub> composite membrane need more excitation energy to overcome the wide band gap energy. On the other hand, 1.0g N, S-CQDs/TiO<sub>2</sub> composite membrane exhibited much lower photodegradation efficiency as compared to 1.5g and 2.0g composite membrane. This was because it had higher band gap energy which required more excitation energy to overcome the band gap and excite the localized electron from VB to CB. Besides, recombination of charge carriers which was faster than interfacial charge transfer happened where the mobilized electron in CB fell to VB and recombined with hole due to lower energy available in CB as compared to higher band gap energy (Jo, *et al.*,2018). Based on the three studies, the optimum loading of NCQDs was found to be 1.5g composite membrane. As it can be observed from Figure 4.13 and 4.14, photocatalytic activity of

1.5g N, S-CQDs/TiO<sub>2</sub> was higher than the pure TiO<sub>2</sub> and other mixed matrix membranes.

Comparing the photodegradation performance of the membranes under visible light and environment light, 1.5g N, S-CQDs/TiO<sub>2</sub> membrane exhibited the highest photodegradation efficiency under environment light irradiation which was 76.73%. For TiO<sub>2</sub>, 1.0g N, S-CQDs/TiO<sub>2</sub> and 2.0g N, S-CQDs/TiO<sub>2</sub> of composite membrane, the photodegradation efficiency is 12.21%, 15.79% and 54.80%. The 1.5g N, S-CQDs/TiO<sub>2</sub> nanohybrids displays a strong and wide emission peak centred at around 380 nm to 410 nm as shown in Figure 4.4. It indicates that the optimum loading of NCQDs incorporated on N, S-CQDs/TiO<sub>2</sub> had shifted and broadening the light absorption wavelength from UV range to visible light range. Thus, light absorption range for 1.5g N, S-CQDs/TiO<sub>2</sub> become wider and resulted in higher photocatalysis performance. Besides, it could be observed that the photodegradation efficiency of 1.0g N, S-CQDs/TiO<sub>2</sub> was almost the same as pure TiO<sub>2</sub> membrane as the photoluminescence (PL) emission of 1.0g N, S-CQDs/TiO<sub>2</sub> nanohybrid composite was greatly weakened at the peak around 390 to 410 nm. This was because the TiO<sub>2</sub> nanoparticles had negligible emission at visible light range and lower loading of NCQDs in the mixed matrix membrane could not shift the light absorption range completely from UV to visible light range and lead to the recombination of photogenerated electron and hole.

From the above mentioned results, the doping of N and S heteroatom onto N, S-CQDs/TiO<sub>2</sub> could significantly improve the photocatalytic performance of pure TiO<sub>2</sub> under environment light irradiation. Such enhancement can be explained as follows. Firstly, the introduction of photosensitizer N, S-CQDs to TiO<sub>2</sub> could effectively favors the spectral response ranging from UV to visible light through newly formed N-Ti-O, Ti-O-C and Ti-O-S chemical bonds between NCQDs and TiO<sub>2</sub> photocatalysts (Aghamali, et al.,2018; Bento, Correa and Pillis, 2019). The shift of light absorption range was due to the introduction of N, S heteroatoms and carbon energy levels. The introduction of N atom will create a mid-gap energy state, Ti<sup>3+</sup> defect below the CB. Meanwhile, S atom will give S 3p atomic orbital at higher energy than the O 2p atomic which shift the VB of TiO<sub>2</sub> upward according to Pauling electronegativity concept (Yan et al., 2017). Thus, the combination of both N and S heteroatom can lowered the band gap energy of TiO<sub>2</sub> as shown in Table 4.1 (Ansari,

*et al.*,2016). Secondly, the smaller particle size of N, S-CQDs exhibited UCPL property due to quantum confinement which could absorb and convert visible light (longer wavelength) into shorter wavelength to excite TiO<sub>2</sub> to generate more hydroxyl radical for the DCF degradation (Aghamali, *et al.*,2018). Thirdly, N, S-CQDs exhibited excellent electron transfer and reservoir due to the conjugated  $\pi$  structure form by N heteroatom binds the neighbour carbon atoms in the form of double bonds (Di et al., 2015; Liang et al., 2018). For the electron reservoir properties, the excess excited or received mobile photogenerated electron could move from CB of TiO<sub>2</sub> to N, S-CQDs which delayed the charge carriers recombination in TiO<sub>2</sub>. Lastly, referring to the study by Ke, Garg and Ling (2014), the doping of N and S atom could lower the work function of N, S-CQDs compared to solely CQDs. By lowering the work function, a large barrier between N, S-CQDs and TiO<sub>2</sub> was formed. In another words, more photogenerated electron could efficiently transfer from CB of N, S-CQDs to CB of TiO<sub>2</sub> through Schottky junction until the fermi energy level reached equilibrium (Li, *et al.*,2017). Hence, more hydroxyl radicals were generated by TiO<sub>2</sub> to degrade the DCF.

From the above discussion, 1.5g N, S-CQDs mixed matrix membrane as the highest photodegradation efficiency under environment light will be used for further studies and discussed in the following section.

Table 4.3: Changes of Photodegradation Efficiency under UV Light Irradiation

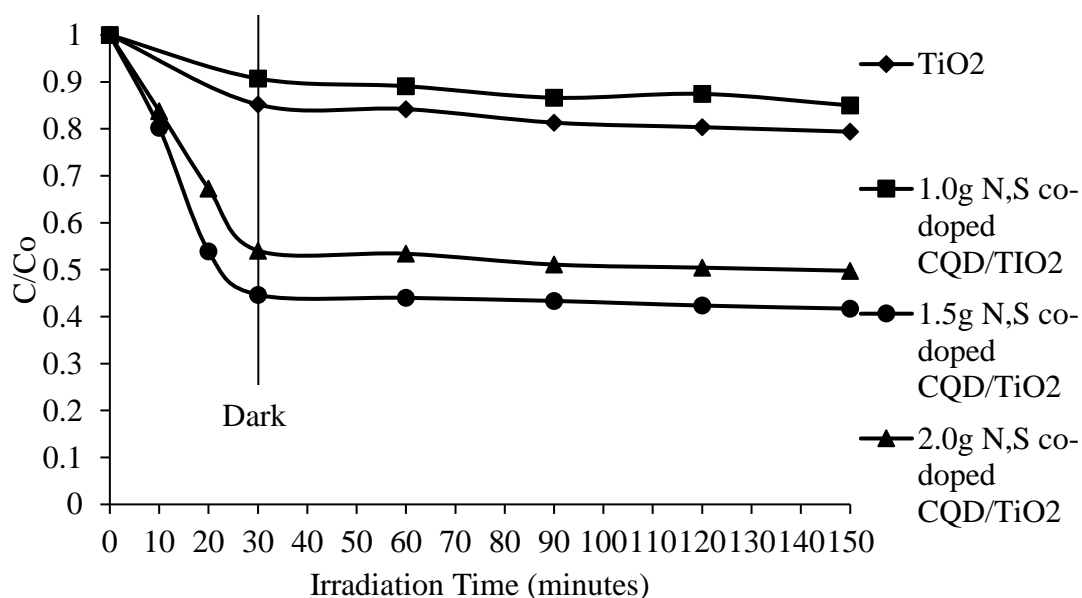
Photocatalytic Membrane	Photodegradation Efficiency (%) at Specific Irradiation Time		Increment of Photodegradation Efficiency (%)
	30 minutes	150 minutes	
TiO <sub>2</sub>	14.81	20.61	5.80
1.0g N, S-CQDs/TiO <sub>2</sub>	9.27	15.00	5.73
1.5g N, S-CQDs/TiO <sub>2</sub>	55.34	58.30	2.96
2.0g N, S-CQDs/TiO <sub>2</sub>	45.94	50.23	4.30

Table 4.4: Changes of Photodegradation Efficiency under Visible Light Irradiation

Photocatalytic Membrane	Photodegradation Efficiency (%) at Specific Irradiation Time		Increment of Photodegradation Efficiency (%)
	30 minutes	150 minutes	
TiO <sub>2</sub>	0.67	3.34	2.67
1.0g N, S-CQDs/TiO <sub>2</sub>	13.80	16.50	2.71
1.5g N, S-CQDs/TiO <sub>2</sub>	48.49	61.08	12.59
2.0g N, S-CQDs/TiO <sub>2</sub>	35.60	46.24	10.65

Table 4.5: Changes of Photodegradation Efficiency under Environment Light Irradiation

Photocatalytic Membrane	Photodegradation Efficiency (%) at Specific Irradiation Time		Increment of Photodegradation Efficiency (%)
	30 minutes	150 minutes	
TiO <sub>2</sub>	1.22	12.21	10.99
1.0g N, S-CQDs/TiO <sub>2</sub>	2.79	15.79	13.01
1.5g N, S-CQDs/TiO <sub>2</sub>	63.01	76.73	13.72
2.0g N, S-CQDs/TiO <sub>2</sub>	41.27	54.80	13.53

Figure 4.12: Photocatalytic Degradation of DCF Pharmaceutical Waste in the Presence of TiO<sub>2</sub> and N, S-CQDs/TiO<sub>2</sub> Membrane with Different Amount of NCQDs under UV Light Irradiation

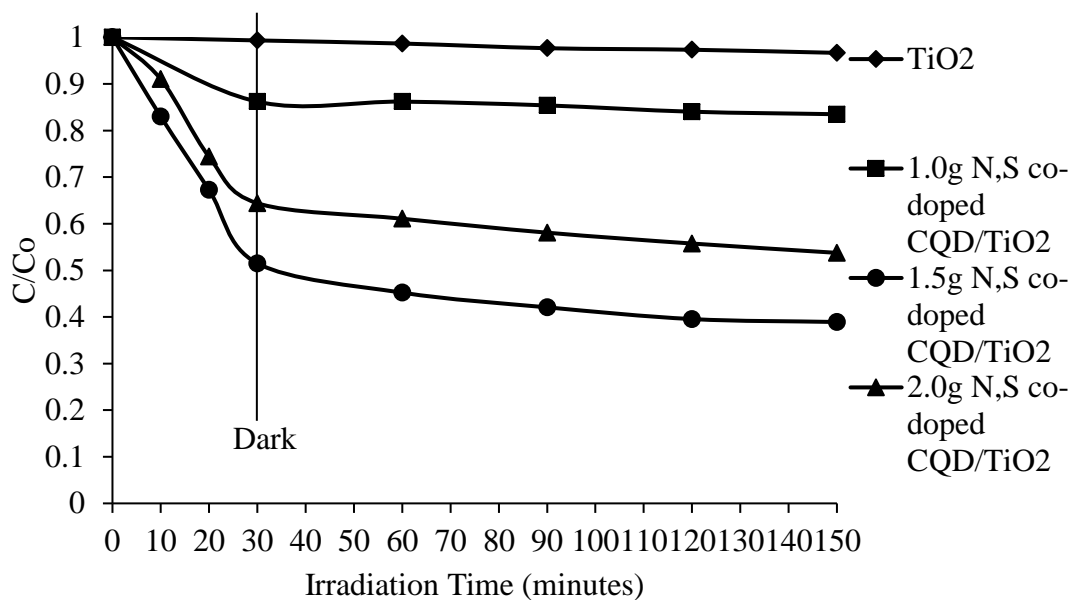


Figure 4.13: Photocatalytic Degradation of DCF Pharmaceutical Waste in the Presence of TiO<sub>2</sub> and N, S-CQDs/TiO<sub>2</sub> Membrane with Different Amount of NCQDs under Visible Light Irradiation

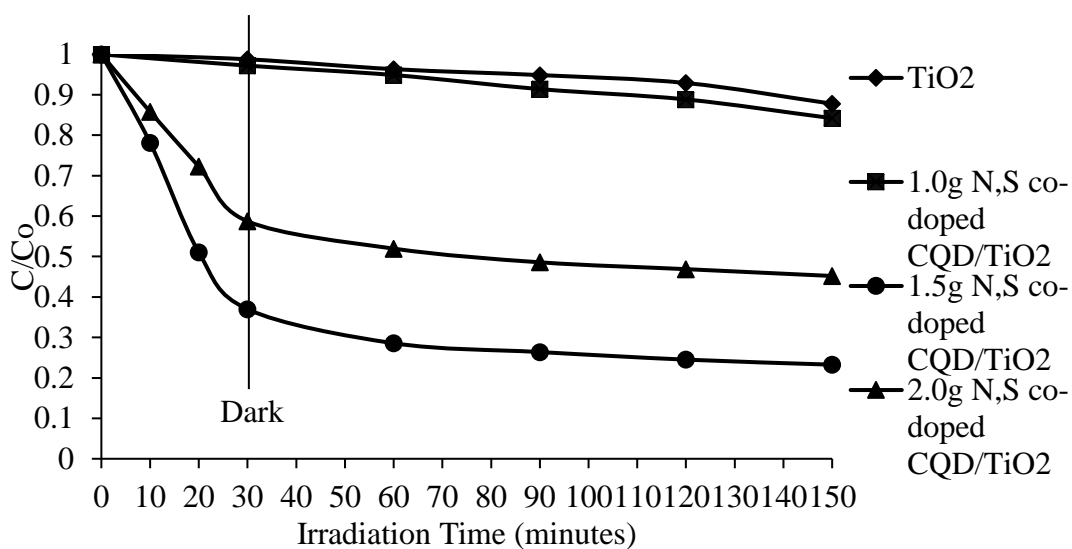


Figure 4.14: Photocatalytic Degradation of DCF Pharmaceutical Waste in the Presence of TiO<sub>2</sub> and N, S-CQDs/TiO<sub>2</sub> Membrane with Different Amount of NCQDs under Environment Light Irradiation

### 4.3 Effect of Photocatalytic Membrane Area on Photocatalytic Performance

The effect of membrane area on the photodegradation process was studied using 1.5g N, S-CQDs/TiO<sub>2</sub> under initial DCF concentration of 10 ppm, environment light irradiation and contact time of 2 hours. Before exposed to environment light, the 10 ppm DCF solution together with photocatalytic membrane inside a beaker were covered with aluminium foil in dark condition for 30 minutes to reach adsorption-desorption equilibrium. The exposed surface area of photocatalytic membrane is a key factor in photodegradation process. Based on the Figure 4.15, the photodegradation efficiency increase 13.65% from membrane area of 9 cm<sup>2</sup> to 25 cm<sup>2</sup>. This was because more active sites of N, S-CQDs/TiO<sub>2</sub> photocatalysts on PSF membrane were available for the photodegradation and guarantees a good contact between photocatalysts and the DCF pollutants. Although increasing photocatalytic membrane area can gives higher photodegradation efficiency, oversize of membrane area will result in bigger foot print, higher fabrication and membrane cleaning cost.

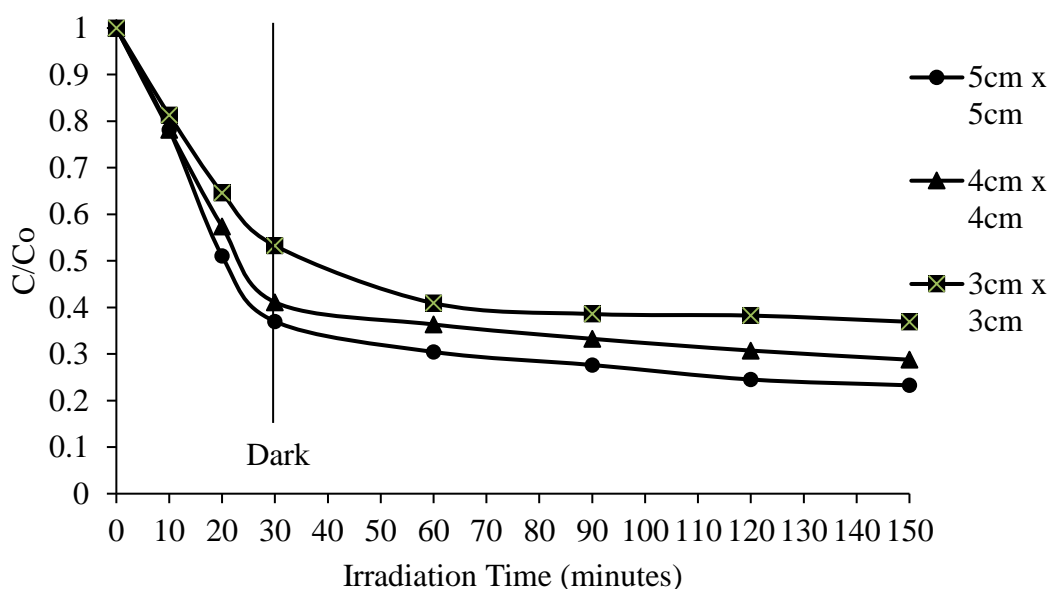


Figure 4.15: Photocatalytic Degradation of DCF Pharmaceutical Waste in the Presence of 1.5g N, S-CQDs/TiO<sub>2</sub> Membrane with Different Membrane Area under Environment Light Irradiation

#### 4.4 Photodegradation Kinetics under Environment Light

The photodegradation kinetics of DCF in N, S-CQDs/TiO<sub>2</sub> composites PSF membrane follow a pseudo-first order kinetic equation:  $\ln(C_0/C) = kt$  (where  $C_0$  and  $C$  are the equilibrium concentration of adsorption and the concentration of DCF at the environment light irradiation time,  $t$ , respectively, and  $k$  is the apparent rate constant). Figure 4.16 represents the plots of  $\ln(C_0/C)$  against irradiation time of the photocatalytic membrane. The plot presents a linear relationship, which means that the photodegradation of DCF on the photocatalytic membrane obeys the rules of a first order reaction kinetics. The apparent reaction rate constants are 0.0008, 0.0011, 0.0088 and 0.0048 min<sup>-1</sup> for TiO<sub>2</sub>, 1.0g N, S-CQDs/TiO<sub>2</sub> 1.5g N, S-CQDs/TiO<sub>2</sub> and 2.0g N, S-CQDs/TiO<sub>2</sub>. Thus, the photocatalytic reaction rate of 1.5g N, S-CQDs/TiO<sub>2</sub> is 11, 8 and 1.833 times larger than that of TiO<sub>2</sub>, 1.0g N, S-CQDs/TiO<sub>2</sub> and 2.0g N, S-CQDs/TiO<sub>2</sub> respectively. The reaction rate constant of 1.5g N, S-CQDs/TiO<sub>2</sub> exceed the undoped TiO<sub>2</sub> which confirms that N, S-CQDs/TiO<sub>2</sub> with suitable NCQDs loading can greatly improve the photocatalytic performance of solely TiO<sub>2</sub>.

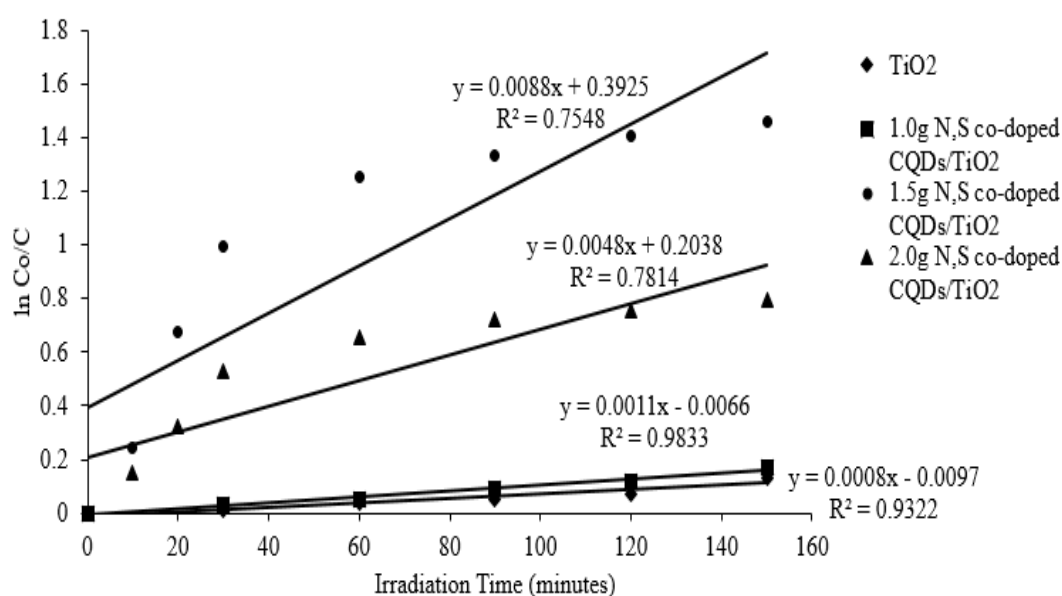


Figure 4.16: Plots of  $\ln(C_0/C)$  Versus Irradiation Time of TiO<sub>2</sub> and N, S-CQDs/TiO<sub>2</sub> with Different NCQDs Loading under Environment Light Irradiation

## 4.5 Hydrophilicity and UF Photocatalytic Membrane Performance

### 4.5.1 Hydrophilicity of Photocatalytic Membrane

The membrane surface hydrophilicity was based on the presence of hydrophilic nanoparticles which can greatly affect the flux ability of membrane. The membrane surface hydrophilicity can be determined by measuring the static water contact angle (SWCA) over the membrane surface using goniometer. The contact angle results for pure TiO<sub>2</sub> membrane and N, S-CQDs/TiO<sub>2</sub> membrane with different NCQDs loading were shown in Table 4.6. As shown in Table 4.6, the SWCA was decreased as the loading of NCQDs photocatalyst was increased in the MMM from 66.67° to 49.71°. This reported that deposition of N, S-CQDs onto TiO<sub>2</sub> improved the hydrophilicity of TiO<sub>2</sub> membrane as a few of hydrophilic N, S-CQDs nanoparticles adsorb and stick on the membrane surface (Yang et al., 2007a). Hence, surface density of hydrophilic hydroxyl groups increased and resulted in improved hydrophilicity (Yong et al., 2019). On the other hand, 2.0g N, S-CQDs/TiO<sub>2</sub> MMM showed the highest contact angle due to excessive loading of NCQDs that aggregate and positioned irregularly on the membrane surface.

Table 4.6: Contact Angle of Different Type of MMM

Mixed Matrix Membrane	Contact Angle (°)
Pure TiO <sub>2</sub>	66.67
1.0g N, S-CQDs/TiO <sub>2</sub>	56.74
1.5g N, S-CQDs/TiO <sub>2</sub>	49.71
2.0g N, S-CQDs/TiO <sub>2</sub>	67.17

### 4.5.2 UF Photocatalytic Membrane Performance

The effect of incorporation of N, S-CQDs with TiO<sub>2</sub> on the permeability of photocatalytic membrane was studied under three different transmembrane pressure (TMP) as shown in Figure 4.17. It can be observed that pure water permeation flux increased with increasing TMP, maximizing at 3 bar, as it is the principle driving force responsible for membrane filtration (Bhattacharya et al., 2019). Effect of TMP on permeation flux can be studied using pure TiO<sub>2</sub> membrane. Figure 4.18 indicates that permeation flux increased steadily with increasing TMP, with 203.72 L/m<sup>2</sup>hr at 1 bar, 427.98 L/m<sup>2</sup>hr at 2 bar and reaching the highest flux of 699.26 L/m<sup>2</sup>hr at 3 bar. Besides, from any TMP observation, the permeability of the pure TiO<sub>2</sub> photocatalytic

membrane increased with the increment of NCQDs loading and then rapidly decreased when the loading of NCQDs reached 2.0g of the photocatalyst. For TMP of 1 bar, the permeation flux of pure TiO<sub>2</sub> membrane is 203.7185 L/m<sup>2</sup>hr and increased steadily until it reached 277.798 L/m<sup>2</sup>hr at 1.5g N,S-CQDs/TiO<sub>2</sub> membrane and dropped to 188.6282 L/m<sup>2</sup>hr at 2.0g N,S-CQDs/TiO<sub>2</sub> membrane. From the permeation flux, it can be concluded that optimum loading of NCQDs was 1.5g because it showed greatly improvement in hydrophilicity properties and provide more open asymmetric membrane structure to attract water molecules to flow into the membrane matrix and promote them to pass through the membrane under TMP driving force (Yang, et al.,2007). Moreover, 1.5g N, S-CQDs/TiO<sub>2</sub> showed more porous structure compare to other mixed matrix membrane as shown in Figure 4.9. The improved in hydrophilicity of pure TiO<sub>2</sub> membrane was due to doping of hydroxyl group of N, S-CQDs nanoparticles as discussed in Section 4.1.1. Doping of hydroxyl group could speed up solvent and non-solvent de-mixing process which facilitated the formation of porous structure (Rawindran, et al.,2019). The overall mechanism of the in-situ phase inversion process was that hydrophilic N,S-CQDs/TiO<sub>2</sub> nanoparticles migrate spontaneously to the interface between UF membrane and water to reduce the interfacial energy and causing an increase of deposition of hydrophilic nanoparticles on the surface of membrane (Vatanpour, et al.,2011).

Hydrophilicity plays an important role in affecting membrane porosity. Based on Table 4.7, membrane porosity increased with the increasing NCQDs loading up to 1.5g and decrease afterwards. The porosity of pure TiO<sub>2</sub> membrane increased from 79.88% to 81.07% and 81.29% for 1.0g N, S-CQDs/TiO<sub>2</sub> and 1.5g N, S-CQDs/TiO<sub>2</sub> nanohybrid membrane. However, excessive NCQDs loading will showed negative effect on membrane porosity and permeation flux. From Table 4.7 and Figure 4.17, the porosity of 2.0g N, S-CQDs /TiO<sub>2</sub> membrane dropped to 78.88% and showed the lowest permeation flux compare to others mixed matrix membrane. This might due to in the increment of the viscosity of prepared sol which could hinder the exchange rate between NMP and N, S-CQDs /TiO<sub>2</sub> sol during the polymer precipitation process. Thus, aggregation of irregular positioning of N, S-CQDs /TiO<sub>2</sub> nanoparticles on the membrane pore and reduced the effective surface area of nanoparticles (Kuvarega, et al.,2018). As a consequences, lesser porous membrane was produced and resulted in lower permeation flux (Vatanpour, et al.,2011). Similar trend was also observed for

mean pore size as shown in Table 4.6. The average pore size increased from 73.70 $\mu\text{m}$  for  $\text{TiO}_2$  membrane to 74.60 $\mu\text{m}$ , 77.20 $\mu\text{m}$ , 73.10 $\mu\text{m}$  for 1.0g N, S-CQDs/ $\text{TiO}_2$ , 1.5g N, S-CQDs/ $\text{TiO}_2$  and 2.0g N, S-CQDs/ $\text{TiO}_2$  membrane respectively. Based on the mean pore size result, we can further confirmed that 1.5g N, S-CQDs/ $\text{TiO}_2$  membrane had the highest flux compare to others membrane due to bigger pore size allowed for water to pass through. Meanwhile, the smallest pore size of 2.0g N, S-CQDs/ $\text{TiO}_2$  MMM was due to the blocking of membrane pores and less connected between membrane pore structures (Zhang, et al.,2017) as discussed in Section 4.1.4.

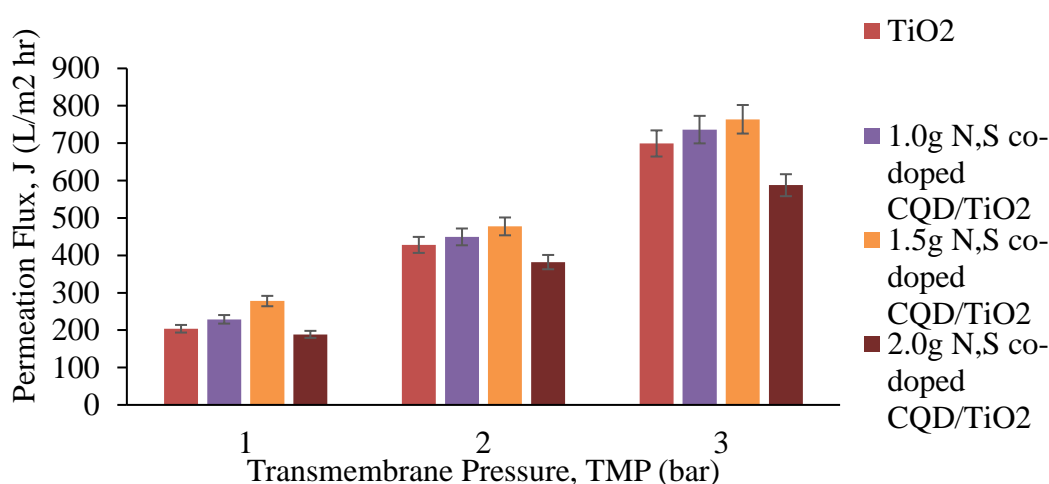


Figure 4.17: Pure Water Flux of  $\text{TiO}_2$  and N, S-CQDs / $\text{TiO}_2$  UF Membrane with Different Amount of NCQDs

Table 4.7: Porosity and Mean Pore Radius of Different Mixed Matrix Membrane Based on Load Pressure of 1 bar

Photocatalytic Membrane	Porosity, $\epsilon$ (%)	Mean Pore Radius, $r_m$ ( $\mu\text{m}$ )
$\text{TiO}_2$	79.88	73.70
1.0g N, S-CQDs/ $\text{TiO}_2$	81.07	74.60
1.5g N, S-CQDs/ $\text{TiO}_2$	81.29	77.20
2.0g N, S-CQDs/ $\text{TiO}_2$	78.88	73.10

#### 4.6 Possible Mechanism of Photodegradation Process

Based on the results discussed in section 4.1-4.5, a plausible mechanism for photocatalytic degradation by N, S-CQDs/TiO<sub>2</sub> MMM was proposed schematically shown in Figure 4.18. The mechanism for this MMM can be explained as follows. Firstly, the adsorption of DCF on the PSF membrane surface deposited with N, S-CQDs/TiO<sub>2</sub> photocatalyst. Secondly, when the MMM is exposed to environment light, the localized electron in VB of TiO<sub>2</sub> and N,S doped CQDs can be excited to their CB respectively and generate holes in VB. It can be noticed that CB of N, S-CQDs was located above CB of TiO<sub>2</sub> due to more negative fermi energy of N, S-CQDs compared to TiO<sub>2</sub> (Zhang and Jaroniec, 2018) which providing a driving force for photogenerated electron injection. Therefore, photogenerated electrons will flow from CB of N, S-CQDs to CB TiO<sub>2</sub>, which form the Schottky junction in the N, S-CQDs/TiO<sub>2</sub> MMM and generate an electromagnetic field that can improve the efficiency of charge carrier separation (Chen, et al.,2017). This confirmed that N, S-CQDs nanoparticles can act as an electron donor. The transfer of delocalized photogenerated electron from CB of N, S-CQDs to CB of TiO<sub>2</sub> resulting in generation of Ti<sup>3+</sup> defects in TiO<sub>2</sub> matrix and favour the O<sub>2</sub> adsorption on MMM surface (Hu, et al.,2018). Thus, more superoxide radical could be generated to degrade DCF effectively. Thirdly, deposition of N, S-CQDs on TiO<sub>2</sub> can widen the light absorption range and help harnessing the full spectrum of environment light. This can be related to the UCPL properties of N, S-CQDs that could emit shorter light wavelength (< 380nm) from longer absorbed light wavelength (> 400nm) (Aghamali, *et al.*,2018). In another words, it means emission energy of photon from light source was larger than the excitation energy. Lastly, N, S-CQDs photocatalyst can act as an electron acceptor where photogenerated electron on CB of TiO<sub>2</sub> tend to transfer to N, S-CQDs. This will result in an efficient electrons and holes separation and enhanced photocatalytic activity (Zhang, et al.,2016). As a result, the photoinduced electrons on the surface of MMM can further oxidize H<sub>2</sub>O to produce hydroxyl radical. Meanwhile, superoxide radical would be formed by combination of photogenerated electron with the adsorbed dissolved oxygen molecules on MMM. Both of these radicals were extremely strong oxidants for decomposition of DCF. After decomposition, DCF will become a non-toxic and smaller size by-product which can easily filtered out by PSF membrane.

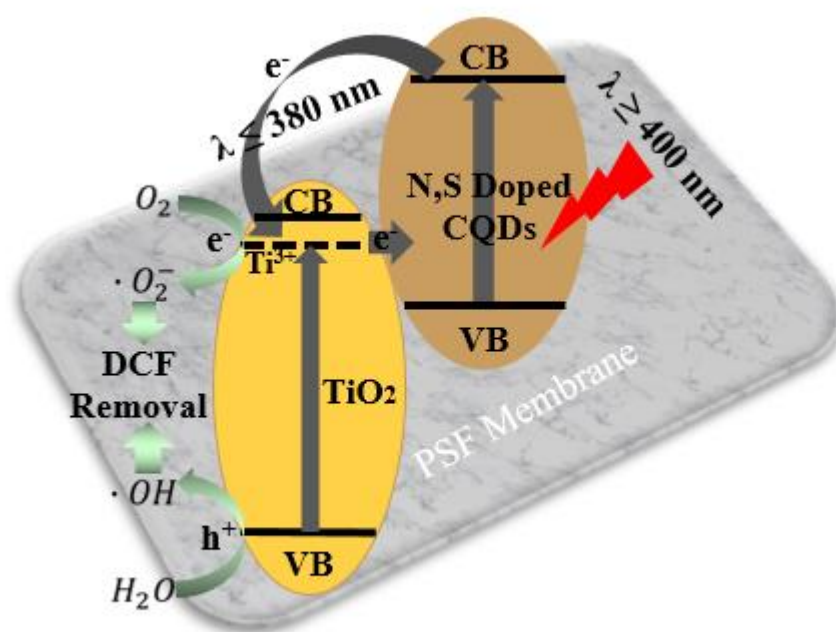


Figure 4.18: Schematic Illustration of the Proposed Photocatalytic Mechanism of N, S-CQDs/TiO<sub>2</sub> MMM under Environment Light Irradiation

## CHAPTER 5

### CONCLUSION AND RECOMMENDATIONS

#### 5.1 Conclusions

In this work, a novel of pure TiO<sub>2</sub> PSF membrane had been successfully improved through incorporation with N, S-CQDs nanoparticles for the employment in the simultaneous photodegradation and separation of DCF pharmaceutical waste in water. The fabricated MMM were characterized by XRD, SEM-EDX, FTIR and SWCA analysis. We found that the N, S-CQDs/TiO<sub>2</sub> nanoparticles were firmly deposited onto PSF membrane and the resulting MMM exhibited excellent photodegradation ability for removing DCF from water under environment light irradiation. Besides, N, S-CQDs/TiO<sub>2</sub> MMM showed improved hydrophilicity and pure water permeation flux compare to pure TiO<sub>2</sub> MMM due to the presence of hydrophilic oxygen containing functional group on PSF membrane surface and increase in porosity. The N, S-CQDs/TiO<sub>2</sub> MMM with 1.5g NCQDs loading showed the highest photodegradation efficiency and pure water permeation flux. Beyond 1.5g NCQDs loading, agglomeration of NCQDs nanoparticles was detected from the characterization study that eventually lower the MMM performance. Besides that, it was found that 1.5g N, S-CQDs/TiO<sub>2</sub> membrane with area of 25cm<sup>2</sup> give the highest photodegradation efficiency due to the presence of more active sites responsible for photodecomposition. Result also revealed that exposure of MMM to TMP affect the pure water permeation flux. Futhermore, Langmuir Hinshelwood kinetic model capable of describing the photodecomposition of DCF was derived. From the model, it was found that N, S-CQDs/TiO<sub>2</sub> MMM with 1.5g NCQDs loading had the highest reaction rate constant of 0.0088 min<sup>-1</sup>. The optimum operating condition were found achieving at the NCQDs loading of 1.5g, MMM area of 25cm<sup>2</sup> and under environmental light source, giving rise to the photodegradation efficiency of 76.73 % and membrane permeation flux of 277.79 L/m<sup>2</sup> hr under 1 bar of TMP. However, there are still some rooms for improvement for fabricating a MMM by entrapping nanostructure materials in substrate to reduce leaching of nanoparticles from the substrate (Pahasup-anan, et al.,2018). Moreover, fabrication of MMM can be done by blending method instead of coating method to ensure evenly dispersion of nanoparticles on membrane surface. In

summary, N, S-CQDs/TiO<sub>2</sub> PSF membrane have great potential for water purification applications, which however required to be explored more thoroughly before it can be commercialized.

## 5.2 Recommendations

There are few recommendations can be suggested in this work in order to further understand the photodegradation and permeation flux performance of MMM in pharmaceutical waste removal. The recommendations are explained as follows.

- i. To study the photodecomposition performance using different types of pharmaceutical waste such as SMX, BZF and CBZ.
- ii. To study the photodegradation performance of pharmaceutical waste using different combinations of hybrid photocatalyst.
- iii. Use a higher loading of TiO<sub>2</sub> nanoparticles to be doped with N, S-CQDs nanoparticles.
- iv. To study the hydrophilicity of MMM by reducing the dosage of membrane pore modifier such as PVP.
- v. To explore additional treatment steps of N, S-CQDs/TiO<sub>2</sub> membrane for stable binding of hybrid nanoparticles to PSF membrane surface.

## REFERENCES

- Adityosulindro, S., Barthe, L., González-Labrada, K., Jáuregui Haza, U.J., Delmas, H. and Julcour, C., 2017. Sonolysis and sono-fenton oxidation for removal of ibuprofen in wastewater. *Ultrasonics Sonochemistry*, 39, pp. 889–896.
- Aghamali, A., Khosravi, M., Hamishehkar, H., Modirshahla, N. and Behnajady, M.A., 2018. Preparation of novel high performance recoverable and natural sunlight-driven nanocomposite photocatalyst of Fe<sub>3</sub>O<sub>4</sub>/C/TiO<sub>2</sub>/N-CQDs. *Materials Science in Semiconductor Processing*, 87(6), pp. 142–154.
- Al-Fori, M., Dobretsov, S., Myint, M.T.Z. and Dutta, J., 2014. Antifouling properties of zinc oxide nanorod coatings. *Biofouling*, 30(7), pp. 871–882.
- Allen, M.J., Tung, V.C. and Kaner, R.B., 2010. Honeycomb carbon: A review of graphene. *Chemical Reviews*, 110(1), pp. 132–145.
- Ansari, S.A., Khan, M.M., Ansari, M.O. and Cho, M.H., 2016. Nitrogen-doped titanium dioxide (N-doped TiO<sub>2</sub>) for visible light photocatalysis. *New Journal of Chemistry*, 40(4), pp. 3000–3009.
- Atabaev, T.S., Hossain, M.A., Lee, D., Kim, H.K. and Hwang, Y.H., 2016. Pt-coated TiO<sub>2</sub> nanorods for photoelectrochemical water splitting applications. *Results in Physics*, 6, pp. 373–376.
- Bagheri, S., Mohd Hir, Z.A., Yousefi, A.T. and Abdul Hamid, S.B., 2015. Progress on mesoporous titanium dioxide: Synthesis, modification and applications. *Microporous and Mesoporous Materials*, 218, pp. 206–222.
- Bagheripour, E., Moghadassi, A.R., Hosseini, S.M., Van derBruggen, B. and Parvizian, F., 2018. Novel composite graphene oxide/chitosan nanoplates incorporated into PES based nanofiltration membrane: Chromium removal and antifouling enhancement. *Journal of Industrial and Engineering Chemistry*, 62, pp. 311–320.
- Bakac, A., 2006. Aqueous rhodium(iii) hydrides and mononuclear rhodium(ii) complexes. *Dalton Transactions*, 13, pp. 1589–1596.
- Bansal, P., Verma, A. and Talwar, S., 2018. Detoxification of real pharmaceutical wastewater by integrating photocatalysis and photo-fenton in fixed-mode. *Chemical Engineering Journal*, 349, pp. 838–848.
- Barzin, J., Madaeni, S.S., Mirzadeh, H. and Mehrabzadeh, M., 2004. Effect of polyvinylpyrrolidone on morphology and performance of hemodialysis membranes prepared from polyether sulfone. *Journal of Applied Polymer Science*, 92(6), pp. 3804–3813.
- Behzadifard, Z., Shariatnia, Z. and Jourshabani, M., 2018. Novel visible light driven CuO/SmFeO<sub>3</sub> nanocomposite photocatalysts with enhanced photocatalytic activities for degradation of organic pollutants. *Journal of Molecular Liquids*, 262, pp. 533–548.

Bento, R.T., Correa, O.V and Pillis, M.F., 2019. Photocatalytic activity of undoped and sulfur-doped TiO<sub>2</sub> films grown by MOCVD for water treatment under visible light. *Journal of the European Ceramic Society*.

Bhattacharya, P., Mukherjee, D., Dey, S., Ghosh, S. and Banerjee, S., 2019. Development and performance evaluation of a novel CuO/TiO<sub>2</sub> ceramic ultrafiltration membrane for ciprofloxacin removal. *Materials Chemistry and Physics*, 229, pp. 106–116.

Bion, N. and Duprez, D., 2016. Water splitting as a tool for obtaining insight into metal–support interactions in catalysis. *Comptes Rendus Chimie*, 19(10), pp. 1326–1336.

Bojarska, M., Nowak, B., Skowroński, J., Piątkiewicz, W. and Gradoń, L., 2017. Growth of ZnO nanowires on polypropylene membrane surface. Characterization and reactivity. *Applied Surface Science*, 391, pp. 457–467.

Borse, V., Thakur, M., Sengupta, S. and Srivastava, R., 2017. N-doped multi-fluorescent carbon dots for ‘turn off-on’ silver-biothiol dual sensing and mammalian cell imaging application. *Sensors and Actuators B: Chemical*, 248, pp. 481–492.

Byrne, C., Subramanian, G. and Pillai, S.C., 2017. Recent advances in photocatalysis for environmental applications. *Journal of Environmental Chemical Engineering*.

Camposeco, R., Castillo, S., Rodriguez-González, V., Hinojosa-Reyes, M., Medina-Álvarez, M.I. and Mejía-Centeno, I., 2018. Promotional effect of Rh nanoparticles on WO<sub>3</sub>/TiO<sub>2</sub> titanate nanotube photocatalysts for boosted hydrogen production. *Journal of Photochemistry and Photobiology A: Chemistry*, 353, pp. 114–121.

Çelik, A., Casey, E. and Hasar, H., 2018. Degradation of oxytetracycline under autotrophic nitrifying conditions in a membrane aerated biofilm reactor and community fingerprinting. *Journal of Hazardous Materials*, 356, pp. 26–33.

Chan, Y.Y., Lim, K.K., Lim, K.H., Teh, C.H., Kee, C.C., Cheong, S.M., Khoo, Y.Y., Baharudin, A., Ling, M.Y., Omar, M.A. and Ahmad, N.A., 2017. Physical activity and overweight/obesity among Malaysian adults: Findings from the 2015 National Health and morbidity survey (NHMS). *BMC Public Health*, 17(1), pp.1–12.

Chang, L.H. and Cho, C.P., 2016. Exploration of silver decoration concentration to enhance photocatalytic efficiency of titanium dioxide photocatalysts. *Solid State Sciences*, 62, pp. 112–120.

Chen, C.-J., Fang, P.-Y. and Chen, K.-C., 2017. Permeate flux recovery of ceramic membrane using TiO<sub>2</sub> with catalytic ozonation. *Ceramics International*, 43, pp. S758–S764.

Chen, L., Moon, J.-H., Ma, X., Zhang, L., Chen, Q., Chen, L., Peng, R., Si, P., Feng, J., Li, Y., Lou, J. and Ci, L., 2018. High performance graphene oxide nanofiltration membrane prepared by electrospaying for wastewater purification.

Chen, Q., Wang, Y., Wang, Y., Zhang, X., Duan, D. and Fan, C., 2017. Nitrogen-doped carbon quantum dots/Ag<sub>3</sub>PO<sub>4</sub> complex photocatalysts with enhanced visible light driven photocatalytic activity and stability. *Journal of Colloid and Interface Science*, 491, pp. 238–245.

Chen, S., Zhao, W., Liu, W. and Zhang, S., 2008. Preparation, characterization and activity evaluation of p–n junction photocatalyst p-ZnO/n-TiO<sub>2</sub>. *Applied Surface Science*, 255(5, Part 1), pp. 2478–2484.

Choi, K., Kang, T. and Oh, S.G., 2012. Preparation of disk shaped ZnO particles using surfactant and their PL properties. *Materials Letters*, 75, pp. 240–243.

Choi, W., Lahiri, I., Seelaboyina, R. and Kang, Y.S., 2010. Synthesis of graphene and its applications: A review. *Critical Reviews in Solid State and Materials Sciences*, 35(1), pp. 52–71.

Choi, Y., Thongsai, N., Chae, A., Jo, S., Kang, E.B., Paoprasert, P., Park, S.Y. and In, I., 2017. Microwave-assisted synthesis of luminescent and biocompatible lysine-based carbon quantum dots. *Journal of Industrial and Engineering Chemistry*, 47, pp. 329–335.

Clarizia, L., Vitiello, G., Pallotti, D.K., Silvestri, B., Nadagouda, M., Lettieri, S., Luciani, G., Andreozzi, R., Maddalena, P. and Marotta, R., 2017. Effect of surface properties of copper-modified commercial titanium dioxide photocatalysts on hydrogen production through photoreforming of alcohols. *International Journal of Hydrogen Energy*, 42(47), pp. 28349–28362.

Cui, B., Feng, X.T., Zhang, F., Wang, Y.L., Liu, X.G., Yang, Y.Z. and Jia, H.S., 2017. The use of carbon quantum dots as fluorescent materials in white LEDs. *Xinxing Tan Cailiao/New Carbon Materials*.

Cui, Z.F., Jiang, Y. and Field, R.W., 2010. Chapter 1: Fundamentals of pressure driven membrane separation processes BT. *Membrane Technology*. Oxford: Butterworth-Heinemann, pp. 1–18.

Darowna, D., Wróbel, R., Morawski, A.W. and Mozia, S., 2017. The influence of feed composition on fouling and stability of a polyethersulfone ultrafiltration membrane in a photocatalytic membrane reactor. *Chemical Engineering Journal*, 310, pp.360–367.

Das, P., Ganguly, S., Mondal, S., Bose, M., Das, A.K., Banerjee, S. and Das, N.C., 2018. Heteroatom doped photoluminescent carbon dots for sensitive detection of acetone in human fluids. *Sensors and Actuators B: Chemical*, 266, pp. 583–593.

Das, R., Bandyopadhyay, R. and Pramanik, P., 2018. Carbon quantum dots from natural resource: A review. *Materials Today Chemistry*, 8, pp. 96–109.

Delsouz Khaki, M.R., Shafeeyan, M.S., Raman, A.A.A. and Daud, W.M.A.W., 2018. Evaluating the efficiency of nano-sized Cu doped TiO<sub>2</sub>/ZnO photocatalyst under visible light irradiation. *Journal of Molecular Liquids*, 258, pp. 354–365.

Department of Environmental, 2016. Malaysia environmental quality report 2016.

Di, J., Xia, J., Ge, Y., Li, H., Ji, H., Xu, H., Zhang, Q., Li, H. and Li, M., 2015. Novel visible-light-driven CQDs/Bi<sub>2</sub>WO<sub>6</sub> hybrid materials with enhanced photocatalytic activity toward organic pollutants degradation and mechanism insight. *Applied Catalysis B: Environmental*, 168–169, pp. 51–61.

Dijkshoorn, J.P., Schutyser, M.A.I., Wagterveld, R.M., Schroën, C.G.P.H. and Boom, R.M., 2017. A comparison of microfiltration and inertia-based microfluidics for large scale suspension separation. *Separation and Purification Technology*.

Dimapilis, E.A.S., Hsu, C.-S., Mendoza, R.M.O. and Lu, M.-C., 2018. Zinc oxide nanoparticles for water disinfection. *Sustainable Environment Research*, 28(2), pp. 47–56.

Dires, S., Birhanu, T., Ambelu, A. and Sahilu, G., 2018. Antibiotic resistant bacteria removal of subsurface flow constructed wetlands from hospital wastewater. *Journal of Environmental Chemical Engineering*, 6(4), pp. 4265–4272.

Divya, K.S., Chandran, A., Reethu, V.N. and Mathew, S., 2018. Enhanced photocatalytic performance of RGO/Ag nanocomposites produced via a facile microwave irradiation for the degradation of Rhodamine B in aqueous solution. *Applied Surface Science*, 444, pp. 811–818.

Djennad, M., Benachour, D. and Schomäcker, R., 2012. Partitioning of substrate within aqueous micelle systems by using dead end and cross flow membrane Filtrations. In: *Procedia Engineering*, pp. 70-77.

Dong, J., Ye, J., Ariyanti, D., Wang, Y., Wei, S. and Gao, W., 2018. Enhancing photocatalytic activities of titanium dioxide via well-dispersed copper nanoparticles. *Chemosphere*, 204, pp. 193–201.

El-Abasawi, N.M., Attia, K.A.M., Abo-serie, A.A.M., Morshedy, S. and Abdel-Fattah, A., 2018. Simultaneous determination of rosuvastatin and propranolol in their binary mixture by synchronous spectrofluorimetry. *Spectrochimica Acta Part A: Molecular and Biomolecular Spectroscopy*, 198, pp. 322–330.

Evingür, G.A. and Pekcan, Ö., 2016. Optical energy band gap of PAAm-GO composites. *Composite Structures*, 183(1), pp. 212–215.

Fan, J., Debruyne, M., Budarin, V.L., Gronnow, M.J., Shuttleworth, P.S., Breeden, S., Macquarrie, D.J. and Clark, J.H., 2013. Direct microwave-assisted hydrothermal depolymerization of cellulose. *Journal of the American Chemical Society*, 135(32), pp. 11728–11731.

Fang, W., Xing, M. and Zhang, J., 2017. Modifications on reduced titanium dioxide photocatalysts: A review. *Journal of Photochemistry and Photobiology C: Photochemistry Reviews*, 32, pp. 21–39.

Feier, B., Florea, A., Cristea, C. and Săndulescu, R., 2018. Electrochemical detection and removal of pharmaceuticals in waste waters. *Current Opinion in Electrochemistry*.

Fent, K., Weston, A.A. and Caminada, D., 2006. Ecotoxicology of human pharmaceuticals. *Aquatic Toxicology*.

Friedman, N.D., Temkin, E. and Carmeli, Y., 2016. The negative impact of antibiotic resistance. *Clinical Microbiology and Infection*, 22(5), pp. 416–422.

Gałęcki, K., Hunter, K., Daňková, G., Rivera, E., Tung, L.W. and Mc Sherry, K., 2016. Experimental and theoretical investigation of bezafibrate binding to serum albumins. *Journal of Luminescence*, 177, pp. 235–241.

Ganiyu, S.O., VanHullebusch, E.D., Cretin, M., Esposito, G. and Oturan, M.A., 2015. Coupling of membrane filtration and advanced oxidation processes for removal of pharmaceutical residues: A critical review. *Separation and Purification Technology*.

Gao, B., Chen, W., Liu, J., An, J., Wang, L., Zhu, Y. and Sillanpää, M., 2018. Continuous removal of tetracycline in a photocatalytic membrane reactor (PMR) with ZnIn<sub>2</sub>S<sub>4</sub> as adsorption and photocatalytic coating layer on PVDF membrane. *Journal of Photochemistry and Photobiology A: Chemistry*, 364, pp. 732–739.

Gao, H., Zhang, P., Hu, J., Pan, J., Fan, J. and Shao, G., 2017. One-dimensional Z-scheme TiO<sub>2</sub>/WO<sub>3</sub>/Pt heterostructures for enhanced hydrogen generation. *Applied Surface Science*, 391, pp. 211–217.

Gentile, G.J., Cruz, M.C., Rajal, V.B. and Fidalgo de Cortalezzi, M.M., 2018. Electrostatic interactions in virus removal by ultrafiltration membranes. *Journal of Environmental Chemical Engineering*, 6(1).

Gomez-Solís, C., Ballesteros, J.C., Torres-Martínez, L.M., Juárez-Ramírez, I., Díaz Torres, L.A., Elvira Zarazua-Morin, M. and Lee, S.W., 2015. Rapid synthesis of ZnO nano-corncoobs from Nital solution and its application in the photodegradation of methyl orange. *Journal of Photochemistry and Photobiology A: Chemistry*, 298, pp. 49–54.

Habibpanah, A.A., Pourhashem, S. and Sarpoolaky, H., 2011. Preparation and characterization of photocatalytic titania-alumina composite membranes by sol-gel methods. *Journal of the European Ceramic Society*, 31(15), pp. 2867–2875.

Han, B., Liu, S., Tang, Z.-R. and Xu, Y.-J., 2015. Electrostatic self-assembly of CdS nanowires-nitrogen doped graphene nanocomposites for enhanced visible light photocatalysis. *Journal of Energy Chemistry*, 24(2), pp. 145–156.

Han, M., Zhu, S., Lu, S., Song, Y., Feng, T., Tao, S., Liu, J. and Yang, B., 2018. Recent progress on the photocatalysis of carbon dots: Classification, mechanism and applications. *Nano Today*.

Han, Y., Huang, H., Zhang, H., Liu, Y., Han, X., Liu, R., Li, H. and Kang, Z., 2014. Carbon quantum dots with photoenhanced hydrogen-bond catalytic activity in aldol condensations. *ACS Catalysis*, 4(3), pp. 781–787.

Han, Y., Xu, Z. and Gao, C., 2013. Ultrathin graphene nanofiltration membrane for water purification. *Advanced Functional Materials*, 23(29), pp. 3693–3700.

Hatat-Fraile, M., Liang, R., Arlos, M.J., He, R.X., Peng, P., Servos, M.R. and Zhou, Y.N., 2017. Concurrent photocatalytic and filtration processes using doped TiO<sub>2</sub> coated quartz fiber membranes in a photocatalytic membrane reactor. *Chemical Engineering Journal*, 330, pp. 531–540.

He, Z., Cheng, X., Kyzas, G.Z. and Fu, J., 2016. Pharmaceuticals pollution of aquaculture and its management in China. *Journal of Molecular Liquids*, 223, pp. 781–789.

Horovitz, I., Avisar, D., Baker, M.A., Grilli, R., Lozzi, L., DiCamillo, D. and Mamane, H., 2016. Carbamazepine degradation using a N-doped TiO<sub>2</sub> coated photocatalytic membrane reactor: Influence of physical parameters. *Journal of Hazardous Materials*, 310, pp. 98–107.

Hou, D., Goei, R., Wang, X., Wang, P. and Lim, T.-T., 2012. Preparation of carbon-sensitized and Fe–Er codoped TiO<sub>2</sub> with response surface methodology for bisphenol A photocatalytic degradation under visible-light irradiation. *Applied Catalysis B: Environmental*, 126, pp. 121–133.

Hu, Y., Xie, X., Wang, X., Wang, Y., Zeng, Y., Pui, D.Y.H. and Sun, J., 2018. Visible-light upconversion carbon quantum dots decorated TiO<sub>2</sub> for the photodegradation of flowing gaseous acetaldehyde. *Applied Surface Science*, 440, pp. 266–274.

Huang, H., Yu, J., Guo, H., Shen, Y., Yang, F., Wang, H., Liu, R. and Liu, Y., 2018. Improved antifouling performance of ultrafiltration membrane via preparing novel zwitterionic polyimide. *Applied Surface Science*, 427, pp. 38–47.

Huang, J.-J., Lin, C.-C. and Wu, D.-S., 2017. Antireflection and passivation property of titanium oxide thin film on silicon nanowire by liquid phase deposition. *Surface and Coatings Technology*, 320, pp. 252–258.

Huang, Z., Gao, Z., Gao, S., Wang, Q., Wang, Z., Huang, B. and Dai, Y., 2017. Facile synthesis of S-doped reduced TiO<sub>2</sub> with enhanced visible-light photocatalytic performance. *Cuihua Xuebao/Chinese Journal of Catalysis*, 38(5), pp. 821–830.

Hubadillah, S.K., Othman, M.H.D., Matsuura, T., Ismail, A.F., Rahman, M.A., Harun, Z., Jaafar, J. and Nomura, M., 2018. Fabrications and applications of low cost ceramic membrane from kaolin: A comprehensive review. *Ceramics International*.

Huggett, D.B., Brooks, B.W., Peterson, B., Foran, C.M. and Schlenk, D., 2002. Toxicity of select beta adrenergic receptor-blocking pharmaceuticals ( $\beta$ -blockers) on aquatic organisms. *Archives of Environmental Contamination and Toxicology*, 43(2), pp. 229–235.

Huo, P., Guan, J., Zhou, M., Ma, C., Liu, X., Yan, Y. and Yuan, S., 2017. Carbon quantum dots modified CdSe loaded reduced graphene oxide for enhancing photocatalytic activity. *Journal of Industrial and Engineering Chemistry*, 50, pp. 147–154.

Iglesias, O., Rivero, M.J., Urriaga, A.M. and Ortiz, I., 2016. Membrane-based photocatalytic systems for process intensification. *Chemical Engineering Journal*.

Iio, S., Yonezu, A., Yamamura, H. and Chen, X., 2016. Deformation modeling of polyvinylidenedifluoride (PVDF) symmetrical microfiltration hollow-fiber (HF) membrane. *Journal of Membrane Science*, 497, pp. 421–429.

Inagaki, M., Park, K.C. and Endo, M., 2010. Carbonization under pressure. *Xinxing Tan Cailiao/New Carbon Materials*.

Isherwood, P.J.M., 2017. Copper zinc oxide: Investigation into a p-type mixed metal oxide system. *Vacuum*, 139, pp. 173–177.

Isidori, M., Nardelli, A., Pascarella, L., Rubino, M. and Parrella, A., 2007. Toxic and genotoxic impact of fibrates and their photoproducts on non-target organisms. *Environment International*, 33(5), pp. 635–641.

Jain, A., Balasubramanian, R. and Srinivasan, M.P., 2016. Hydrothermal conversion of biomass waste to activated carbon with high porosity: A review. *Chemical Engineering Journal*, 283, pp. 789–805.

Janssens, R., Mandal, M.K., Dubey, K.K. and Luis, P., 2017. Slurry photocatalytic membrane reactor technology for removal of pharmaceutical compounds from wastewater: Towards cytostatic drug elimination. *Science of the Total Environment*.

Ji, Y., Qian, W., Yu, Y., An, Q., Liu, L., Zhou, Y. and Gao, C., 2017. Recent developments in nanofiltration membranes based on nanomaterials. *Chinese Journal of Chemical Engineering*.

Jiang, G., Geng, K., Wu, Y., Han, Y. and Shen, X., 2018. High photocatalytic performance of ruthenium complexes sensitizing g-C<sub>3</sub>N<sub>4</sub>/TiO<sub>2</sub> hybrid in visible light irradiation. *Applied Catalysis B: Environmental*, 227, pp. 366–375.

Jo, Y.K., Lee, J.M., Son, S. and Hwang, S.J., 2018. 2D inorganic nanosheet-based hybrid photocatalysts: Design, applications, and perspectives. *Journal of Photochemistry and Photobiology C: Photochemistry Reviews*.

Jung, J., Ryu, J.H., Choi, S.Y., Park, K.Y., Song, W.J., Yu, Y.J., Jang, Y. sung, Park, J. and Kweon, J., 2018. Autopsy study of irreversible foulants on polyvinylidene fluoride hollow-fiber membranes in an immersed microfiltration system operated for five years. *Separation and Purification Technology*, 199, pp. 1–8.

Kanakaraju, D., Glass, B.D. and Oelgemöller, M., 2018. Advanced oxidation process-mediated removal of pharmaceuticals from water: A review. *Journal of Environmental Management*, 219, pp. 189–207.

Kandy, M.M. and Gaikar, V.G., 2018. Photocatalytic reduction of CO<sub>2</sub> using CdS nanorods on porous anodic alumina support. *Materials Research Bulletin*, 102, pp. 440–449.

Karaolia, P., Michael-Kordatou, I., Hapeshi, E., Drosou, C., Bertakis, Y., Christofilos, D., Armatas, G.S., Sygellou, L., Schwartz, T., Xekoukoulotakis, N.P. and Fatta-Kassinos, D., 2018. Removal of antibiotics, antibiotic-resistant bacteria and their associated genes by graphene-based TiO<sub>2</sub> composite photocatalysts under solar radiation in urban wastewaters. *Applied Catalysis B: Environmental*, 224, pp. 810–824.

Ke, Y., Garg, B. and Ling, Y.-C., 2014. Waste chicken eggshell as low-cost precursor for efficient synthesis of nitrogen-doped fluorescent carbon nanodots and their multi-functional applications. *RSC Advances*, 4(102), pp. 58329–58336.

Khan, A., Sherazi, T.A., Khan, Y., Li, S., Naqvi, S.A.R. and Cui, Z., 2018. Fabrication and characterization of polysulfone/modified nanocarbon black composite antifouling ultrafiltration membranes. *Journal of Membrane Science*, 554, pp. 71–82.

Kitano, S., Hashimoto, K. and Kominami, H., 2011. Photocatalytic mineralization of volatile organic compounds over commercial titanium (IV) oxide modified with rhodium (III) ion under visible light irradiation and correlation between physical properties and photocatalytic activity. In: *Catalysis Today*. pp. 404–409.

Kitano, S., Sadakiyo, M., Kato, K., Yamauchi, M., Asakura, H., Tanaka, T., Hashimoto, K. and Kominami, H., 2017. Effects of the structure of the Rh<sup>3+</sup> modifier on photocatalytic performances of an Rh<sup>3+</sup>/TiO<sub>2</sub> photocatalyst under irradiation of visible light. *Applied Catalysis B: Environmental*, 205, pp. 340–346.

Kitano, S., Tanaka, A., Hashimoto, K. and Kominami, H., 2016. Metal ion-modified TiO<sub>2</sub> photocatalysts having controllable oxidative performance under irradiation of visible light. *Applied Catalysis A: General*, 521, pp. 202–207.

Ko, C.C., Ali, A., Drioli, E., Tung, K.L., Chen, C.-H., Chen, Y.R. and Macedonio, F., 2018. Performance of ceramic membrane in vacuum membrane distillation and in vacuum membrane crystallization. *Desalination*, 440, pp. 48–58.

Kourde-Hanafi, Y., Loulergue, P., Szymczyk, A., Van derBruggen, B., Nachtnebel, M., Rabiller-Baudry, M., Audic, J.-L., Pölt, P. and Baddari, K., 2017. Influence of PVP content on degradation of PES/PVP membranes: Insights from characterization of membranes with controlled composition. *Journal of Membrane Science*, 533, pp. 261–269.

Kumar, A., Kumar, P., M.S., A., Singh, D.P., Behera, B. and Jain, S.L., 2018. A bridged ruthenium dimer (Ru–Ru) for photoreduction of CO<sub>2</sub> under visible light irradiation. *Journal of Industrial and Engineering Chemistry*, 61, pp. 381–387.

Kuvarega, A.T., Khumalo, N., Dlamini, D. and Mamba, B.B., 2018. Polysulfone/N,Pd co-doped TiO<sub>2</sub> composite membranes for photocatalytic dye degradation. *Separation and Purification Technology*, 191(July 2017), pp. 122–133.

- Lei, D., Yang, W., Gong, Y., Jing, J., Nie, H., Yu, B. and Zhang, X., 2016. Non-covalent decoration of carbon dots with folic acid via a polymer-assisted strategy for fast and targeted cancer cell fluorescence imaging. *Sensors and Actuators B: Chemical*, 230, pp. 714–720.
- Leong, S., Razmjou, A., Wang, K., Hapgood, K., Zhang, X. and Wang, H., 2014. TiO<sub>2</sub> based photocatalytic membranes: A review. *Journal of Membrane Science*, 472, pp. 167–184.
- Li, H., Ji, J., Cheng, C. and Liang, K., 2018. Preparation of phenol-formaldehyde resin-coupled TiO<sub>2</sub> and study of photocatalytic activity during phenol degradation under sunlight. *Journal of Physics and Chemistry of Solids*, 122, pp. 25–30.
- Li, M., Wang, M., Zhu, L., Li, Y., Yan, Z., Shen, Z. and Cao, X., 2018. Facile microwave assisted synthesis of N-rich carbon quantum dots/dual-phase TiO<sub>2</sub> heterostructured nanocomposites with high activity in CO<sub>2</sub> photoreduction. *Applied Catalysis B: Environmental*, 231, pp. 269–276.
- Li, X., Li, J., Cui, Z. and Yao, Y., 2016. Modeling of filtration characteristics during submerged hollow fiber membrane microfiltration of yeast suspension under aeration condition. *Journal of Membrane Science*, 510, pp. 455–465.
- Li, X., Shen, R., Ma, S., Chen, X. and Xie, J., 2018c. Graphene-based heterojunction photocatalysts. *Applied Surface Science*, 430, pp. 53–107.
- Li, Z., Zhang, Y., Niu, Q., Mou, M., Wu, Y., Liu, X., Yan, Z. and Liao, S., 2017. A fluorescence probe based on the nitrogen-doped carbon dots prepared from orange juice for detecting Hg<sup>2+</sup> in water. *Journal of Luminescence*, 187, pp. 274–280.
- Liang, S., Xiao, K., Mo, Y. and Huang, X., 2012. A novel ZnO nanoparticle blended polyvinylidene fluoride membrane for anti-irreversible fouling. *Journal of Membrane Science*, 394–395, pp. 184–192.
- Liang, Y., Shen, Y.F., Liu, C.L. and Ren, X.Y., 2018. Effects of chemical bonds between nitrogen and its neighbor carbon atoms on fluorescence properties of carbon quantum dots. *Journal of Luminescence*, 197, pp.285–290.
- Lien, L.T.Q., Hoa, N.Q., Chuc, N.T.K., Thoa, N.T.M., Phuc, H.D., Diwan, V., Dat, N.T., Tamhankar, A.J. and Lundborg, C.S., 2016. Antibiotics in wastewater of a rural and an urban hospital before and after wastewater treatment, and the relationship with antibiotic use—a one year study from Vietnam. *International Journal of Environmental Research and Public Health*, 13(6).
- Lim, S.Y., Shen, W. and Gao, Z., 2015. Carbon quantum dots and their applications. *Chemical Society Reviews*, 44(1), pp. 362–381.
- Lin, C.C., Wu, D.S. and Huang, J.J., 2018. Antireflection and passivation property of aluminium oxide thin film on silicon nanowire by liquid phase deposition. *Surface and Coatings Technology*.

Liu, C., Zhang, L., Liu, R., Gao, Z., Yang, X., Tu, Z., Yang, F., Ye, Z., Cui, L., Xu, C. and Li, Y., 2016. Hydrothermal synthesis of N-doped TiO<sub>2</sub> nanowires and N-doped graphene heterostructures with enhanced photocatalytic properties. *Journal of Alloys and Compounds*, 656, pp. 24–32.

Liu, L., Qi, Y., Hu, J., Liang, Y. and Cui, W., 2015. Efficient visible-light photocatalytic hydrogen evolution and enhanced photostability of core shell, Cu<sub>2</sub>O / g-C<sub>3</sub>N<sub>4</sub> octahedra. *Applied Surface Science*, 351, pp. 1146–1154.

Liu, X., Zhou, Y., Zhang, J., Luo, L., Yang, Y., Huang, H., Peng, H., Tang, L. and Mu, Y., 2018. Insight into electro-fenton and photo-fenton for the degradation of antibiotics: Mechanism study and research gaps. *Chemical Engineering Journal*, 347, pp. 379–397.

Liu, Y., Wang, R., Yang, Z., Du, H., Jiang, Y., Shen, C., Liang, K. and Xu, A., 2015. Enhanced visible-light photocatalytic activity of Z-scheme graphitic carbon nitride/oxygen vacancy-rich zinc oxide hybrid photocatalysts. *Chinese Journal of Catalysis*, 36(12), pp. 2135–2144.

Lonappan, L., Brar, S.K., Das, R.K., Verma, M. and Surampalli, R.Y., 2016. Diclofenac and its transformation products: Environmental occurrence and toxicity: A review. *Environment International*, 96, pp.127–138.

Lv, J., Zhang, G., Zhang, H., Zhao, C. and Yang, F., 2018. Improvement of antifouling performances for modified PVDF ultrafiltration membrane with hydrophilic cellulose nanocrystal. *Applied Surface Science*, 440, pp. 1091–1100.

Ma, Y., 2012. Enhancement of the biodegradability of ethylenediamine in wastewater by sono-fenton degradation. *International Journal of Chemical, Material and Environmental Research*, 10(2), pp. 117–127.

Malaysia, A.S., 2015. *Water Supply and Wastewater Management Services in Malaysia*.

Martins, N.C.T., Ângelo, J., Violeta, A., Trindade, T., Andrade, L. and Mendes, A., 2016. Applied Catalysis B: Environmental N-doped carbon quantum dots / TiO<sub>2</sub> composite with improved photocatalytic activity. *Applied Catalysis B, Environmental*, 193, pp.67–74.

Matamoros, V., García, J. and Bayona, J.M., 2008. Organic micropollutant removal in a full-scale surface flow constructed wetland fed with secondary effluent. *Water Research*, 42(3), pp. 653–660.

Mathias, F.T., Fockink, D.H., Disner, G.R., Prodocimo, V., Ribas, J.L.C., Ramos, L.P., Cestari, M.M. and Silva de Assis, H.C., 2018. Effects of low concentrations of ibuprofen on freshwater fish *Rhamdia quelen*. *Environmental Toxicology and Pharmacology*, 59, pp. 105–113.

Melvin Ng, H.K., Leo, C.P. and Abdullah, A.Z., 2017. Selective removal of dyes by molecular imprinted TiO<sub>2</sub> nanoparticles in polysulfone ultrafiltration membrane. *Journal of Environmental Chemical Engineering*, 5(4), pp. 3991–3998.

Meng, L.Y., Wang, B., Ma, M.G. and Lin, K.L., 2016. The progress of microwave-assisted hydrothermal method in the synthesis of functional nanomaterials. *Materials Today Chemistry*, 1–2, pp. 63–83.

Ministry of Health Malaysia, 2014. *Malaysian Statistics on Medicines 2009 and 2010. Pharmaceutical Services Division and Clinical Research Centre Ministry of Health.*

Molinari, R., Lavorato, C. and Argurio, P., 2017. Recent progress of photocatalytic membrane reactors in water treatment and in synthesis of organic compounds. A review. *Catalysis Today*, 281, pp. 144–164.

Molinari, R., Palmisano, L., Drioli, E. and Schiavello, M., 2002. Studies on various reactor configurations for coupling photocatalysis and membrane processes in water purification. *Journal of Membrane Science*, 206(1–2), pp. 399–415.

Moza, S., Darowna, D., Wróbel, R. and Morawski, A.W., 2015. A study on the stability of polyethersulfone ultrafiltration membranes in a photocatalytic membrane reactor. *Journal of Membrane Science*, 495, pp. 176–186.

Namdari, P., Negahdari, B. and Eatemadi, A., 2017. Synthesis, properties and biomedical applications of carbon-based quantum dots: An updated review. *Biomedicine and Pharmacotherapy*.

Nasirian, M. and Mehrvar, M., 2018. Photocatalytic degradation of aqueous methyl orange using nitrogen-doped TiO<sub>2</sub> photocatalyst prepared by novel method of ultraviolet-assisted thermal synthesis. *Journal of Environmental Sciences*, 66, pp. 81–93.

Nazarkovsky, M.A., Bogatyrov, V.M., Czech, B., Galaburda, M.V, Wójcik, G., Kolomys, O.F., Strelchuk, V.V, Malysheva, M.L., Oranska, O.I. and Gun'ko, V.M., 2017. Synthesis and properties of zinc oxide photocatalyst by high-temperature processing of resorcinol-formaldehyde/zinc acetate mixture. *Journal of Photochemistry and Photobiology A: Chemistry*, 334, pp. 36–46.

Nemati, F., Hosseini, M., Zare-Dorabei, R., Salehnia, F. and Ganjali, M.R., 2018. Fluorescent turn on sensing of Caffeine in food sample based on sulfur-doped carbon quantum dots and optimization of process parameters through response surface methodology. *Sensors and Actuators B: Chemical*, 273, pp. 25–34.

Nikolaou, A., Meric, S. and Fatta, D., 2007. Occurrence patterns of pharmaceuticals in water and wastewater environments. In: *Analytical and Bioanalytical Chemistry*. pp. 1225–1234.

Oh, W.C., Ullah, K., Zhu, L., Meng, Z.Da, Ye, S. and Sarkar, S., 2014. Photocatalytic properties under visible light with graphene based platinum selenide nanocomposites synthesized by microwave assisted method. *Materials Science in Semiconductor Processing*, 25, pp. 34–42.

Okon, K.O., Balogun, S.T., Askira, U.M., Jibrin, Y.B., Aguru, C.U., Isyaka, T.M. and Ghamba, P.E., 2014. Retrospective analysis of gram-negative bacteria isolated at a tertiary hospital in Maiduguri, Nigeria. *British Microbiology Research Journal*, 4, pp. 1235–1247.

Onsekizoglu, P., Ng, L.Y., Mohammad, a. W.A.W., Ng, C.Y., Li, F., Meng, J., Ye, J., Yang, B., Tian, Q., Deng, C., Bass, M., Freger, V., Hegab, H.M., Zou, L., Xi, Z.Y., Xu, Y.Y., Zhu, L.P., Wang, Y., Zhu, B.K., Mohammad, a. W.A.W., Teow, Y.H., Ang, W.L., Chung, Y.T., Oatley-Radcliffe, D.L., Hilal, N., Song, J., Li, X., Li, Z., Zhang, M., Yin, Y., Zhao, B., Kong, D., Akbari, A., Homayoonfal, M., Miller, D.J., Paul, D.R., Freeman, B.D., Khulbe, K.C., Feng, C., Matsuura, T., Li, F., Ye, J., Yang, L., Deng, C., Tian, Q. and Gryta, M., 2015. Membrane Distillation: Principle, advances, limitations and future prospects in food industry. *Journal of Membrane Science*, 344(1–2), pp. 226–254.

Ouyang, S. and Ye, J., 2011.  $\beta$ -AgAl<sub>1-x</sub>Ga<sub>x</sub>O<sub>2</sub> solid solution photocatalysts: Continuous modulation of electronic structure toward high performance visible light photoactivity. *Journal of the American Chemical Society*, 133(20), pp. 7757–7763.

Owens, G.J., Singh, R.K., Foroutan, F., Alqaysi, M., Han, C.M., Mahapatra, C., Kim, H.W. and Knowles, J.C., 2016. Sol-gel based materials for biomedical applications. *Progress in Materials Science*, 77, pp. 1–79.

Ozawa, H., Honda, S., Katano, D., Sugiura, T. and Arakawa, H., 2014. Novel ruthenium sensitizers with a dianionic tridentate ligand for dye-sensitized solar cells: the relationship between the solar cell performances and the electron-withdrawing ability of substituents on the ligand. *Dalton Transactions*, 43(21), pp. 8026–8036.

Pahasup-anan, T., Suwannahong, K., Dechapanya, W. and Rangkupan, R., 2017. Fabrication and photocatalytic activity of TiO<sub>2</sub> composite membranes via simultaneous electrospinning and electrospaying process. *Journal of Environmental Sciences*.

Pang, Y.L. and Abdullah, A.Z., 2013. Effect of carbon and nitrogen co-doping on characteristics and sonocatalytic activity of TiO<sub>2</sub> nanotubes catalyst for degradation of Rhodamine B in water. *Chemical Engineering Journal*, 214, pp. 129–138.

Park, S., Park, J., Heo, J., Hong, B.Y. and Hong, J., 2017. Growth behaviors and biocidal properties of titanium dioxide films depending on nucleation duration in liquid phase deposition. *Applied Surface Science*, 425, pp. 547–552.

Patil, J.V, Mali, S.S., Kamble, A.S., Hong, C.K., Kim, J.H. and Patil, P.S., 2017. Electrospinning: A versatile technique for making of 1D growth of nanostructured nanofibers and its applications: An experimental approach. *Applied Surface Science*, 423, pp. 641–674.

Pérez del Pino, A., González-Campo, A., Giraldo, S., Peral, J., György, E., Logofatu, C., deMello, A.J. and Puigmartí-Luis, J., 2018. Synthesis of graphene-based photocatalysts for water splitting by laser-induced doping with ionic liquids. *Carbon*, 130, pp. 48–58.

Periyat, P., McCormack, D.E., Hinder, S.J. and Pillai, S.C., 2009. One pot synthesis of anionic (nitrogen) and cationic (sulfur) codoped high temperature stable, visible light active, anatase photocatalysts. *The Journal of Physical Chemistry C*, 113(8), pp. 3246–3253.

Phan, D.D., Babick, F., Nguyen, M.T., Wessely, B. and Stintz, M., 2017. Modelling the influence of mass transfer on fixed-bed photocatalytic membrane reactors. *Chemical Engineering Science*, 173, pp. 242–252.

Pirhashemi, M., Habibi-Yangjeh, A. and Rahim Pouran, S., 2018. Review on the criteria anticipated for the fabrication of highly efficient ZnO-based visible-light-driven photocatalysts. *Journal of Industrial and Engineering Chemistry*.

Praveena, S.M., Shaifuddin, S.N.M., Sukiman, S., Nasir, F.A.M., Hanafi, Z., Kamarudin, N., Ismail, T.H.T. and Aris, A.Z., 2018. Pharmaceuticals residues in selected tropical surface water bodies from Selangor (Malaysia): Occurrence and potential risk assessments. *Science of The Total Environment*, 642, pp. 230–240.

Puga, A.V., 2016. Photocatalytic production of hydrogen from biomass-derived feedstocks. *Coordination Chemistry Reviews*.

Putri, L.K., Ong, W.J., Chang, W.S. and Chai, S.-P., 2015. Heteroatom doped graphene in photocatalysis: A review. *Applied Surface Science*, 358, pp. 2–14.

Rajamanickam, D. and Shanthi, M., 2016. Photocatalytic degradation of an organic pollutant by zinc oxide – solar process. *Arabian Journal of Chemistry*, 9, pp. S1858–S1868.

Rajendran, K. and Sen, S., 2018. Adsorptive removal of carbamazepine using biosynthesized hematite nanoparticles. *Environmental Nanotechnology, Monitoring & Management*, 9, pp. 122–127.

Rani, P. and Jindal, V.K., 2013. Designing band gap of graphene by B and N dopant atoms. *RSC Advances*, 3(3), pp. 802–812.

Ravishankar, H., Roddick, F., Navaratna, D. and Jegatheesan, V., 2018. Preparation, characterisation and critical flux determination of graphene oxide blended polysulfone (PSf) membranes in an MBR system. *Journal of Environmental Management*, 213, pp. 168–179.

Rawindran, H., Lim, J.-W., Goh, P.-S., Subramaniam, M.N., Ismail, A.F., Radi bin Nik M Daud, N.M. and Rezaei-Dasht Arzhandi, M., 2019. Simultaneous separation and degradation of surfactants laden in produced water using PVDF/TiO<sub>2</sub> photocatalytic membrane. *Journal of Cleaner Production*, 221, pp. 490–501.

Reddy, K.R., Karthik, K.V, Prasad, S.B.B., Soni, S.K., Jeong, H.M. and Raghu, A.V, 2016. Enhanced photocatalytic activity of nanostructured titanium dioxide/polyaniline hybrid photocatalysts. *Polyhedron*, 120, pp. 169–174.

Rehman, M.S.U., Rashid, N., Ashfaq, M., Saif, A., Ahmad, N. and Han, J.I., 2015. Global risk of pharmaceutical contamination from highly populated developing countries. *Chemosphere*, 138, pp. 1045–1055.

Riad, S., Mania, J., Bouchaou, L. and Najjar, Y., 2004. Rainfall-runoff model using an artificial neural network approach. *Mathematical and Computer Modelling*, 40(7–8), pp. 839–846.

Rizzo, L., Maniaia, C., Merlin, C., Schwartz, T., Dagot, C., Ploy, M.C., Michael, I. and Fatta-Kassinos, D., 2013. Urban wastewater treatment plants as hotspots for antibiotic resistant bacteria and genes spread into the environment: A review. *Science of The Total Environment*, 447, pp. 345–360.

Rosman, N., Salleh, W.N.W., Mohamed, M.A., Jaafar, J., Ismail, A.F. and Harun, Z., 2018. Hybrid membrane filtration-advanced oxidation processes for removal of pharmaceutical residue. *Journal of Colloid and Interface Science*, 532, pp. 236–260.

Saeki, D., Minami, R. and Matsuyama, H., 2017. Effects of operating conditions on biofouling in crossflow ultrafiltration membrane processes. *Separation and Purification Technology*, 189, pp. 138–144.

Salavati-Niasari, M., Soofivand, F., Sobhani-Nasab, A., Shakouri-Arani, M., Yeganeh Faal, A. and Bagheri, S., 2016. Synthesis, characterization, and morphological control of ZnTiO<sub>3</sub> nanoparticles through sol-gel processes and its photocatalyst application. *Advanced Powder Technology*, 27(5), pp. 2066–2075.

Salim, N.E., Jaafar, J., Ismail, A.F., Othman, M.H.D., Rahman, M.A., Yusof, N., Qtaishat, M., Matsuura, T., Aziz, F. and Salleh, W.N.W., 2018. Preparation and characterization of hydrophilic surface modifier macromolecule modified poly (ether sulfone) photocatalytic membrane for phenol removal. *Chemical Engineering Journal*, 335, pp. 236–247.

Saranya, K., Rameez, M. and Subramania, A., 2015. Developments in conducting polymer based counter electrodes for dye-sensitized solar cells: An overview. *European Polymer Journal*, 66, pp. 207–227.

Saraswat, S.K., Rodene, D.D. and Gupta, R.B., 2018. Recent advancements in semiconductor materials for photoelectrochemical water splitting for hydrogen production using visible light. *Renewable and Sustainable Energy Reviews*.

Shabat-Hadas, E., Mamane, H. and Gitis, V., 2017. Rhodamine B in dissolved and nano-bound forms: Indicators for light-based advanced oxidation processes. *Chemosphere*, 184, pp. 1020–1027.

- Shahbazi, R., Payan, A. and Fattahi, M., 2018. Preparation, evaluations and operating conditions optimization of nano TiO<sub>2</sub> over graphene based materials as the photocatalyst for degradation of phenol. *Journal of Photochemistry and Photobiology A: Chemistry*.
- Shamsuddin, N., Das, D.B. and Starov, V.M., 2015. Filtration of natural organic matter using ultrafiltration membranes for drinking water purposes: Circular cross-flow compared with stirred dead end flow. *Chemical Engineering Journal*, 276, pp. 331–339.
- Shen, T., Wang, Q., Guo, Z., Kuang, J. and Cao, W., 2018. Hydrothermal synthesis of carbon quantum dots using different precursors and their combination with TiO<sub>2</sub> for enhanced photocatalytic activity. *Ceramics International*, 44(10), pp. 11828–11834.
- Shi, R., Li, Z., Yu, H., Shang, L., Zhou, C., Waterhouse, G.I.N., Wu, L.-Z. and Zhang, T., 2017. Effect of nitrogen doping level on the performance of N-doped carbon quantum dot/TiO<sub>2</sub> composites for photocatalytic hydrogen evolution. *ChemSusChem*.
- Shi Ying Lim, W.S., Z.G., Lim, S.Y., Shen, W. and Gao, Z., 2014. Carbon quantum dots and their applications. *Chemical Society reviews*, 44(1), pp. 362–381.
- DaSilva Souza, D.R., Caminhas, L.D., deMesquita, J.P. and Pereira, F.V., 2018. Luminescent carbon dots obtained from cellulose. *Materials Chemistry and Physics*, 203, pp. 148–155.
- Singh, S., Mahalingam, H. and Singh, P.K., 2013. Polymer-supported titanium dioxide photocatalysts for environmental remediation: A review. *Applied Catalysis A: General*.
- Starr, B.J., Tarabara, V.V, Herrera-Robledo, M., Zhou, M., Roualdès, S. and Ayrál, A., 2016. Coating porous membranes with a photocatalyst: Comparison of LbL self-assembly and plasma-enhanced CVD techniques. *Journal of Membrane Science*, 514, pp. 340–349.
- Szabó, R.K., Megyeri, C., Illés, E., Gajda-Schranz, K., Mazellier, P. and Dombi, A., 2011. Phototransformation of ibuprofen and ketoprofen in aqueous solutions. *Chemosphere*, 84(11), pp. 1658–1663.
- Szymański, K., Morawski, A.W. and Mozia, S., 2018. Effectiveness of treatment of secondary effluent from a municipal wastewater treatment plant in a photocatalytic membrane reactor and hybrid UV/H<sub>2</sub>O<sub>2</sub>: Ultrafiltration system. *Chemical Engineering and Processing: Process Intensification*, 125, pp. 318–324.
- Tahir, M., Tahir, B., Saidina Amin, N.A. and Alias, H., 2016. Selective photocatalytic reduction of CO<sub>2</sub> by H<sub>2</sub>O/H<sub>2</sub> to CH<sub>4</sub> and CH<sub>3</sub>OH over Cu-promoted In<sub>2</sub>O<sub>3</sub>/TiO<sub>2</sub> nanocatalyst. *Applied Surface Science*, 389, pp. 46–55.
- Trapido, M., Kulik, N., Goi, A., Veressinina, Y. and Munter, R., 2009. Fenton treatment efficacy for the purification of different kinds of wastewater. *Water Science and Technology*, 60(7), pp. 1795–1801.

Tsehay, M.T., Wang, J., Zhu, J., Velizarov, S. and Van derBruggen, B., 2018. Development and characterization of polyethersulfone-based nanofiltration membrane with stability to hydrogen peroxide. *Journal of Membrane Science*, 550, pp.462–469.

United Nations, 2018. Executive Summary Sustainable Development Goal 6 Synthesis Report 2018 on Water and Sanitation 2 Sustainable Development Goal 6 Synthesis Report 2018 on Water and Sanitation. Sustainable Development Goal 6. p. 16.

Ünlü, B., Çakar, S. and Özacar, M., 2018. The effects of metal doped TiO<sub>2</sub> and dithizone-metal complexes on DSSCs performance. *Solar Energy*, 166, pp. 441–449.

Unser, S., Bruzas, I., He, J. and Sagle, L., 2015. Localized surface plasmon resonance biosensing: Current challenges and approaches. *Sensors*, 15(7), pp. 15684–15716.

Usachov, D., Vilkov, O., Grüneis, A., Haberer, D., Fedorov, A., Adamchuk, V.K., Preobrajenski, A.B., Dudin, P., Barinov, A., Oehzelt, M., Laubschat, C. and Vyalikh, D.V., 2011. Nitrogen-doped graphene: Efficient growth, structure and electronic properties. *Nano Letters*, 11(12), pp. 5401–5407.

Vahidzadeh, E., Fatemi, S. and Nouralishahi, A., 2018. Synthesis of a nitrogen-doped titanium dioxide–reduced graphene oxide nanocomposite for photocatalysis under visible light irradiation. *Particuology*.

Vatanpour, V., Madaeni, S.S., Moradian, R., Zinadini, S. and Astinchap, B., 2011. Fabrication and characterization of novel antifouling nanofiltration membrane prepared from oxidized multiwalled carbon nanotube/polyethersulfone nanocomposite. *Journal of Membrane Science*, 375(1), pp. 284–294.

Vulava, V.M., Cory, W.C., Murphey, V.L. and Ulmer, C.Z., 2016. Sorption, photodegradation, and chemical transformation of naproxen and ibuprofen in soils and water. *Science of The Total Environment*, 565, pp. 1063–1070.

Wadekar, S.S. and Vidic, R.D., 2018. Comparison of ceramic and polymeric nanofiltration membranes for treatment of abandoned coal mine drainage. *Desalination*.

Wang, C.L. and Chen, C.Y., 2018. Fast and controllable sensitization of dye-sensitized solar cells by microwave irradiation. *Solar Energy*, 169, pp. 249–254.

Wang, J., Wang, Z., Huang, B., Ma, Y., Liu, Y., Qin, X., Zhang, X. and Dai, Y., 2012. Oxygen vacancy induced band gap narrowing and enhanced visible light photocatalytic activity of ZnO. *ACS Applied Materials and Interfaces*, 4(8), pp. 4024–4030.

Wang, M., Li, Z., Wu, Y., Ma, J. and Lu, G., 2017. Inhibition of hydrogen and oxygen reverse recombination reaction over Pt/TiO<sub>2</sub> by F ions and its impact on the photocatalytic hydrogen formation. *Journal of Catalysis*, 353, pp. 162–170.

Wang, M., Zhen, W., Tian, B., Ma, J. and Lu, G., 2018. The inhibition of hydrogen and oxygen recombination reaction by halogen atoms on over-all water splitting over Pt-TiO<sub>2</sub> photocatalyst. *Applied Catalysis B: Environmental*, 236, pp. 240–252.

Wang, Q., Yang, C., Zhang, G., Hu, L. and Wang, P., 2017. Photocatalytic Fe-doped TiO<sub>2</sub>/PSF composite UF membranes: Characterization and performance on BPA removal under visible-light irradiation. *Chemical Engineering Journal*, 319, pp. 39–47.

Wang, Q., Yang, C., Zhang, G., Hu, L. and Wang, P., 2017. Photocatalytic Fe-doped TiO<sub>2</sub>/PSF composite UF membranes: Characterization and performance on BPA removal under visible-light irradiation. *Chemical Engineering Journal*, 319, pp. 39–47.

Wang, S. and Wang, J., 2017. Carbamazepine degradation by gamma irradiation coupled to biological treatment. *Journal of Hazardous Materials*, 321, pp. 639–646.

Wang, T., Zhai, Y., Zhu, Y., Li, C. and Zeng, G., 2018. A review of the hydrothermal carbonization of biomass waste for hydrochar formation: Process conditions, fundamentals, and physicochemical properties. *Renewable and Sustainable Energy Reviews*, 90, pp. 223–247.

Wang, Q., Yang, C., Zhang, G., Hu, L. and Wang, P., 2017. Photocatalytic Fe-doped TiO<sub>2</sub>/PSF composite UF membranes: Characterization and performance on BPA removal under visible-light irradiation. *Chemical Engineering Journal*, 319, pp. 39–47.

Wang, W., Tadé, M.O. and Shao, Z., 2018. Nitrogen-doped simple and complex oxides for photocatalysis: A review. *Progress in Materials Science*.

Warsinger, D.M., Chakraborty, S., Tow, E.W., Plumlee, M.H., Bellona, C., Loutatidou, S., Karimi, L., Mikelonis, A.M., Achilli, A., Ghassemi, A., Padhye, L.P., Snyder, S.A., Curcio, S., Vecitis, C.D., Arfat, H.A. and Lienhard, J.H., 2018. A review of polymeric membranes and processes for potable water reuse. *Progress in Polymer Science*.

Witte, W., 1998. Medical consequences of antibiotics use in agriculture. *Science*.

Wolpher, H., Johansson, O., Abrahamsson, M., Kritikos, M., Sun, L. and Åkermark, B., 2004. A tridentate ligand for preparation of bisterpyridine-like ruthenium(II) complexes with an increased excited state lifetime. *Inorganic Chemistry Communications*, 7(3), pp. 337–340.

Wu, B., Wang, Y., Lim, W., Chew, J.W., Fane, A.G. and Liu, Y., 2016. Enhanced performance of submerged hollow fibre microfiltration by fluidized granular activated carbon. *Journal of Membrane Science*, 499, pp. 47–55.

Xie, S., Wang, Y., Zhang, Q., Deng, W. and Wang, Y., 2014. MgO and Pt promoted TiO<sub>2</sub> as an efficient photocatalyst for the preferential reduction of carbon dioxide in the presence of water. *ACS Catalysis*, 4(10), pp. 3644–3653.

- Xu, H., Ding, M., Chen, W., Li, Y. and Wang, K., 2018. Nitrogen-doped GO/TiO<sub>2</sub> nanocomposite ultrafiltration membranes for improved photocatalytic performance. *Separation and Purification Technology*, 195, pp. 70–82.
- Xu, Q., Zhang, L., Yu, J., Wageh, S., Al-Ghamdi, A.A. and Jaroniec, M., 2018. Direct Z-scheme photocatalysts: Principles, synthesis, and applications. *Materials Today*.
- Yan, X., Yuan, K., Lu, N., Xu, H., Zhang, S., Takeuchi, N., Kobayashi, H. and Li, R., 2017. The interplay of sulfur doping and surface hydroxyl in band gap engineering: Mesoporous sulfur-doped TiO<sub>2</sub> coupled with magnetite as a recyclable, efficient, visible light active photocatalyst for water purification. *Applied Catalysis B: Environmental*, 218, pp. 20–31.
- Yang, Y., Zhang, H., Wang, P., Zheng, Q. and Li, J., 2007. The influence of nano-sized TiO<sub>2</sub> fillers on the morphologies and properties of PSF UF membrane. *Journal of Membrane Science*, 288(1), pp. 231–238.
- Yeh, T.F., Chen, S.J., Yeh, C.S. and Teng, H., 2013. Tuning the electronic structure of graphite oxide through ammonia treatment for photocatalytic generation of H<sub>2</sub> and O<sub>2</sub> from water splitting. *The Journal of Physical Chemistry C*, 117(13), pp. 6516–6524.
- Yeh, T.F., Cihlář, J., Chang, C.Y., Cheng, C. and Teng, H., 2013. Roles of graphene oxide in photocatalytic water splitting. *Materials Today*, 16(3), pp. 78–84.
- Yong, M., Zhang, Y., Sun, S. and Liu, W., 2019. Properties of polyvinyl chloride (PVC) ultrafiltration membrane improved by lignin: Hydrophilicity and antifouling. *Journal of Membrane Science*, 575, pp. 50–59.
- Yu, S., Wang, Y., Sun, F., Wang, R. and Zhou, Y., 2018. Novel mpg-C<sub>3</sub>N<sub>4</sub>/TiO<sub>2</sub> nanocomposite photocatalytic membrane reactor for sulfamethoxazole photodegradation. *Chemical Engineering Journal*, 337, pp. 183–192.
- Zangeneh, H., Zinatizadeh, A.A., Zinadini, S., Feyzi, M. and Bahnemann, D.W., 2018. A novel photocatalytic self-cleaning PES nanofiltration membrane incorporating triple metal-nonmetal doped TiO<sub>2</sub> (K-B-N-TiO<sub>2</sub>) for post treatment of biologically treated palm oil mill effluent. *Reactive and Functional Polymers*, 127, pp. 139–152.
- Zhang, D., Karkooti, A., Liu, L., Sadrzadeh, M., Thundat, T., Liu, Y. and Narain, R., 2018. Fabrication of antifouling and antibacterial polyethersulfone (PES)/cellulose nanocrystals (CNC) nanocomposite membranes. *Journal of Membrane Science*, 549, pp. 350–356.
- Zhang, H., Cao, J., Kang, P., Tang, Q., Sun, Q. and Ma, M., 2018. Ag nanocrystals decorated g-C<sub>3</sub>N<sub>4</sub>/Nafion hybrid membranes: One-step synthesis and photocatalytic performance. *Materials Letters*, 213, pp. 218–221.
- Zhang, J., Wang, Z., Liu, M., Zhao, F. and Wu, Z., 2017. In-situ modification of PVDF membrane during phase-inversion process using carbon nanosphere sol as coagulation bath for enhancing anti-fouling ability. *Journal of Membrane Science*, 526, pp. 272–280.

Zhang, J., Zhang, X., Dong, S., Zhou, X. and Dong, S., 2016. N-doped carbon quantum dots/TiO<sub>2</sub> hybrid composites with enhanced visible light driven photocatalytic activity toward dye wastewater degradation and mechanism insight. *Journal of Photochemistry and Photobiology A: Chemistry*, 325, pp. 104–110.

Zhang, L. and Jaroniec, M., 2018. Toward designing semiconductor-semiconductor heterojunctions for photocatalytic applications. *Applied Surface Science*, 430, pp. 2–17.

Zhang, Q.Q., Ying, G.G., Pan, C.G., Liu, Y.S. and Zhao, J.L., 2015. Comprehensive evaluation of antibiotics emission and fate in the river basins of China: Source analysis, multimedia modeling, and linkage to bacterial resistance. *Environmental Science and Technology*, 49(11), pp. 6772–6782.

Zhang, W., Ding, L., Luo, J., Jaffrin, M.Y. and Tang, B., 2016. Membrane fouling in photocatalytic membrane reactors (PMRs) for water and wastewater treatment: A critical review. *Chemical Engineering Journal*.

Zhang, X., Wang, D.K. and Diniz Da Costa, J.C., 2014. Recent progresses on fabrication of photocatalytic membranes for water treatment. *Catalysis Today*, 230, pp. 47–54.

Zhang, Y.Q., Ma, D.K., Zhang, Y.G., Chen, W. and Huang, S.M., 2013. N-doped carbon quantum dots for TiO<sub>2</sub> based photocatalysts and dye-sensitized solar cells. *Nano Energy*, 2(5), pp. 545–552.

Zhang, Y., Yang, H.M. and Park, S.J., 2018. Synthesis and characterization of nitrogen-doped TiO<sub>2</sub> coatings on reduced graphene oxide for enhancing the visible light photocatalytic activity. *Current Applied Physics*, 18(2), pp. 163–169.

Zhang, Y., Zhao, Y., Duan, J. and Tang, Q., 2018. S-doped CQDs tailored transparent counter electrodes for high-efficiency bifacial dye-sensitized solar cells. *Electrochimica Acta*, 261, pp. 588–595.

Zhao, J., Li, Y., Zhu, Y., Wang, Y. and Wang, C., 2016. Enhanced CO<sub>2</sub> photoreduction activity of black TiO<sub>2</sub> coated Cu nanoparticles under visible light irradiation: Role of metallic Cu. *Applied Catalysis A: General*, 510, pp. 34–41.

Zhong, Y., Shao, Y., Ma, F., Wu, Y., Huang, B. and Hao, X., 2017. Band gap-matched CdSe QD/WS<sub>2</sub> nanosheet composite: Size-controlled photocatalyst for high-efficiency water splitting. *Nano Energy*, 31, pp. 84–89.

Zhou, F., Yan, C., Liang, T., Sun, Q. and Wang, H., 2018. Photocatalytic degradation of orange G using sepiolite TiO<sub>2</sub> nanocomposites: Optimization of physicochemical parameters and kinetics studies. *Chemical Engineering Science*, 183, pp. 231–239.

Zhou, Y., Engler, N. and Nelles, M., 2018. Symbiotic relationship between hydrothermal carbonization technology and anaerobic digestion for food waste in China. *Bioresource Technology*.

Zong, H., Xia, X., Liang, Y., Dai, S., Alsaedi, A., Hayat, T., Kong, F. and Pan, J.H., 2018. Designing function-oriented artificial nanomaterials and membranes via electrospinning and electrospraying techniques. *Materials Science and Engineering C*.